Spherical and Non-spherical Bubble Dynamics in Soft Matter

by

Kazuya Murakami

A dissertation submitted in partial fulfillment
of the requirements for the degree of
Doctor of Philosophy
(Mechanical Engineering and Scientific Computing)
in The University of Michigan
2020

Doctoral Committee:

Associate Professor Eric Johnsen, Chair
Assistant Professor Jesse Samuel Capecelatro
Associate Professor Karthik Duraisamy
Assistant Professor Jon Estrada

Kazuya Murakami
mkazuya@umich.edu
ORCID iD: 0000-0002-2010-0477

To my parents and brother.

ACKNOWLEDGMENTS

I would like to express my deepest gratitude to my advisor, Prof. Eric Johnsen, for his mentorship and support during my Ph.D. studies. His kindness and incisive advice on my research have been of paramount importance for my success. I extend my gratitude to the committee members, first to Prof. Jesse Capecelatro and Prof. Karthik Duraisamy not only for their time and guidance but also for instructing me in CFD and data-driven analysis. Their classes are definitely one of my best experiences at Michigan. Michigan is really an ideal place to study CFD, an exciting topic in science and engineering. I am also very grateful to Prof. Jon Estrada for leading our cavitation project as well as for his comments on my dissertation.

There are many people whose collaborations are indispensable to my achievements. First of all, I sincerely thank Prof. Christian Franck for letting me participate in the BRC project. This project is really an interesting interdisciplinary research with clear vision and objectives. I am grateful to many colleagues in the BRC project: Prof. Tim Colonius, Prof. David Hennan, Prof. Zhen Xu, Alice Fawzi, Jonathan Sukovich, Selda Buyukozturk, Harry Cramer, Kevin Schmidmayer, Jean-Sebastien Spratt, Anastasia Tzoumaka, and Jin Yang. In particular, I thank Prof. Hennan, Selda, Anastasia, and Jin for closely working together on cavitation modeling. I was so fortunate to be a member of this BRC group. I am also grateful to Prof. Keita Ando and Yushi Yamakawa for their experimental studies. Prof. Ando is actually my previous advisor when I was an undergraduate student and is the person who recommended me to study abroad. I greatly appreciate his kind support and suggestion. I also thank Renaud Gaudron for working hard together on a complicated

mathematical problem.

I would like to express my gratitude to the members of Scientific Computing and Flow Physics Laboratory: Minki Kim, Griffin Cearley, Mauro Rodriguez, Lauren Mancia, Shahaboddin Beig, Eunhye An, Samuel Pellone, Michael Wadas, Suyash Tandon, Philip Johnson, Kevin Ma, and William White. My special thanks go to Minki for fruitful discussions and a friendship. I also thank my classmates: Gregory Shallcross, Yuan Yao, Sarah Beetham, Ali Kord, Weitao Sun, Miao Zi Wee, and a visiting student, Tomoki Kondo. I am also very grateful to Prof. Katsuo Kurabayashi for his personal mentorship and advice on my career. Finally, I would like to thank my parents and brother for their continuous support, encouragement and understanding.

This work was supported by ONR grant N00014-17-1-2058 (under Dr. T. Bentley) and Overseas Scholarship from the Funai Foundation for Information Technology.

TABLE OF CONTENTS

LIST OF FIGURES

Figure

LIST OF TABLES

Table

LIST OF APPENDICES

Appendix

LIST OF ABBREVIATIONS

IMR Inertial Microcavitation high strain-rate Rheometry

TBI Traumatic Brain Injury

ODE Ordinary Differential Equation

PDE Partial Differential Equation

STP Standard Temperature and Pressure

CFL Courant-Friedrichs-Lewy

ABSTRACT

Cavitation and bubble dynamics play an important role in a wide range of applications including material characterization and therapeutic ultrasound. A specific problem in bubble dynamics is inertially dominated collapse, which occurs when a bubble reaches a critical size compared to its equilibrium size. This inertial collapse of cavitation bubbles enables us to characterize soft materials at high strain-rates or to ablate malignant tissue in therapeutic ultrasound. This thesis contributes to the understanding of spherical and non-spherical bubble dynamics in soft matter relevant to these applications.

We first study ultrasound-induced oscillations of a gas bubble in soft matter. Oscillations of a spherical bubble in water are described by a classical Rayleigh–Plesset-type model. Although this model has been extended to include viscoelasticity necessary to represent soft matter, experiments of nonlinear bubble oscillations in soft matter are scarce, thus limiting opportunities for validating the models and understanding the role of viscoelasticity on bubble oscillations. We experimentally and numerically study ultrasound-induced bubble oscillations in a gelatin gel. Comparison of finite-amplitude oscillations between experiments and numerical solutions show good agreement, implying the validity of the viscoelastic modeling. A resonance curve of the ultrasound-induced bubble oscillations is obtained and shows the nonlinear feature of spring softening, where viscoelasticity has an impact on the resonant radius and peak amplitude.

Since cavitation bubbles in soft materials consist of a finite amount of non-condensible gas as well as vapor, we investigate the role of gas-vapor mixture transport on the bubble dynamics. From a modeling standpoint, past studies relied on the assumption that the ratios of specific heats are the same for the gas and vapor. We develop a new model that accounts for the mixture with

different ratios of specific heats. Numerical solutions show that vapor is trapped by an air shell during inertial collapse. This trapped vapor reduces the bubble collapse velocity and thus energy losses via acoustic radiation, leading to a larger bubble rebound. This analysis is further validated against experiments of laser-induced bubble collapse in glycerol. Comparison between the new and conventional models shows experimentally measurable discrepancies of several percent.

Finally, we study the shape stability of a bubble in soft matter. Bubbles deviate from a spherical shape in practice, typically due to one of two mechanisms: parametric instability or Rayleigh-Taylor-type instability. We develop a model for non-spherical bubble dynamics in soft matter by extending classical perturbation analysis on a plane interface to a spherical interface between a gas and a soft solid. Parametric instability occurs during ultrasound-induced oscillations. The natural frequency and a Mathieu equation obtained from the non-spherical model predict unstable modes in parametric instability, which agrees with experimental observations in gelatin gels. Rayleigh–Taylor-type instability is induced by the large acceleration during inertial collapse. Numerical solutions of the non-spherical model show that viscoelasticity influences the bubble wall acceleration and thus is a key factor to determine this instability.

CHAPTER 1

Introduction

1.1 The role of cavitation and bubble dynamics

1.1.1 Inertial microcavitation high strain-rate rheometry

Cavitation and bubble dynamics form the foundation of a new technique for material characterization called Inertial Microcavitation high strain-rate Rheometry (IMR) (Estrada *et al.*, 2018). In general, cavitation is known as vaporization due to pressure drop below the saturated vapor pressure[1] (Brennen, 1995). On the other hand, we often use a focused laser pulse to control a nucleation site of a cavitation bubble (e.g., Brujan & Vogel, 2002). The process of laser-induced cavitation is illustrated in figure 1.1: a laser pulse is focused into a soft material (a), which induces complex growth of a cavitation bubble to the maximum size (b), and the bubble collapses subsequently and oscillates toward the equilibrium state (c). An important feature of the bubble dynamics is that the soft material surrounding the bubble has a much larger density than that of the gas inside the bubble. When the bubble grows to sufficiently large size, the huge density difference results in the nonlinear behavior of the subsequent bubble oscillations as depicted in the time history of bubble radius in figure 1.1. This is so-called inertial cavitation or inertial collapse (Flynn, 1975a,b; Leighton, 1994). IMR is a technique to characterize soft materials using this laser-induced inertial cavitation of a micron-sized bubble.

[1] For water, 3.1 kPa at 25 °C and 101.3 kPa (1 atm) at 100 °C. An interesting example of cavitation is a cracking glass bottle as a popular party trick (Daily *et al.*, 2014).

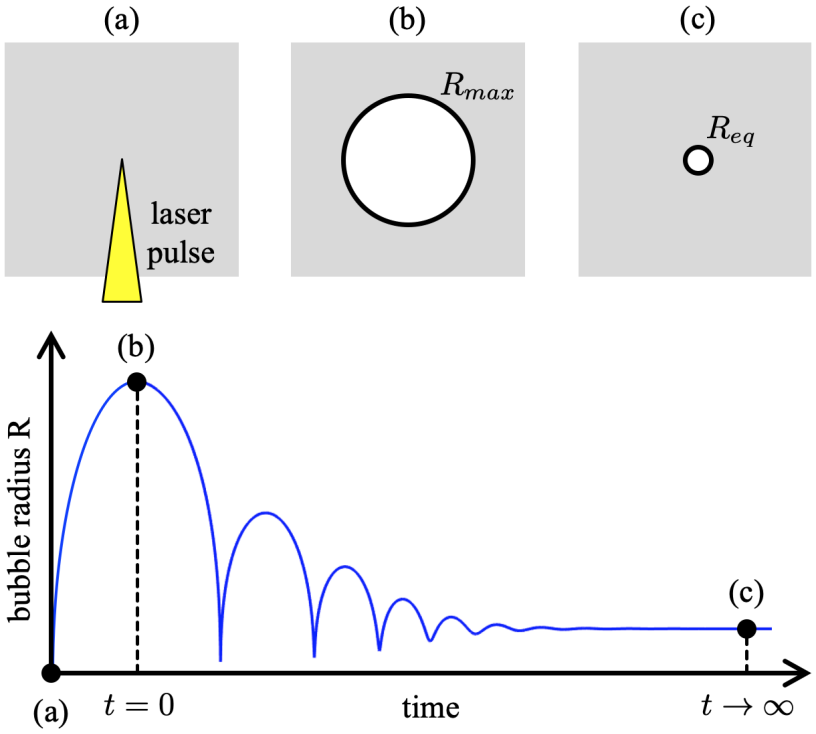

Figure 1.1: The process of spherically symmetric laser-induced inertial cavitation in a soft material. A laser pulse is focused into a soft material (a), which induces complex growth of the bubble to the maximum radius R_{max} (b). Subsequently, the bubble collapses inertially and oscillates toward the equilibrium state with the radius R_{eq} (c).

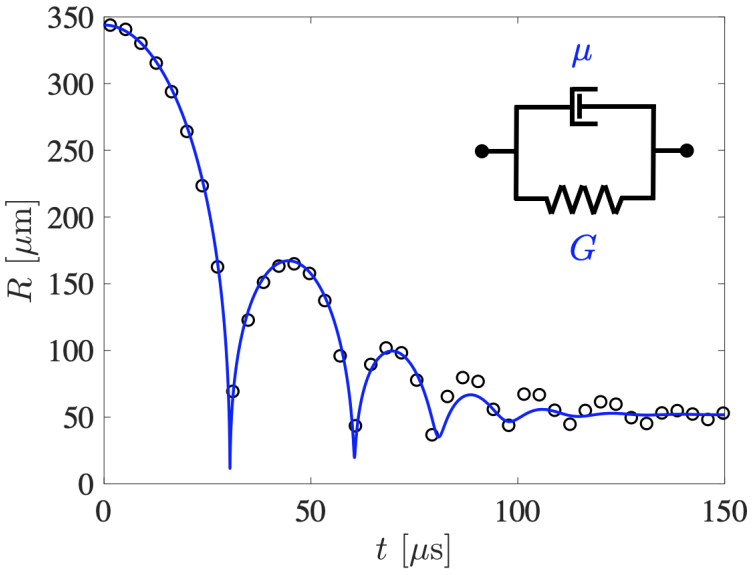

Figure 1.2: An example of material characterization through IMR. A theoretical-numerical cavitation model (blue line) reproduces experiments of the laser-induced inertial collapse of a bubble in a soft material (black circles) with fitted viscosity μ and shear modulus G.

The idea behind IMR is to compare the experiments of laser-induced inertial cavitation in a soft material recorded by a high-speed camera with a theoretical-numerical cavitation model (Estrada *et al.*, 2018). Figure 1.2 shows an example of material characterization through IMR. We first choose a constitutive equation, which is a Kelvin–Voigt viscoelastic model consisting of a damper and a spring in parallel in this example. Then, solutions of the cavitation model (blue line) are fitted to the experiments (black circles) with appropriate viscosity μ and shear modulus G. The cavitation model reproduces the experiments well in this example. If the fit is not adequate, we repeat the same process with a different constitutive equation. This process yields the constitutive model and corresponding viscoelastic properties for the soft material used in experiments.

The target of IMR is to characterize soft materials at high strain-rates, which conventional techniques cannot readily achieve. Figure 1.3 summarizes current material testing techniques with regard to the corresponding regimes of strain rates (x-axis) and stresses (y-axis). Tension-compression testing characterizes materials only at quasi-static scheme. The Kolsky bar or Taylor impact are applied in the high-strain rates regime, but these techniques are for stiff materials in which high stresses are induced. IMR is an approach that can be applied to soft materials at high

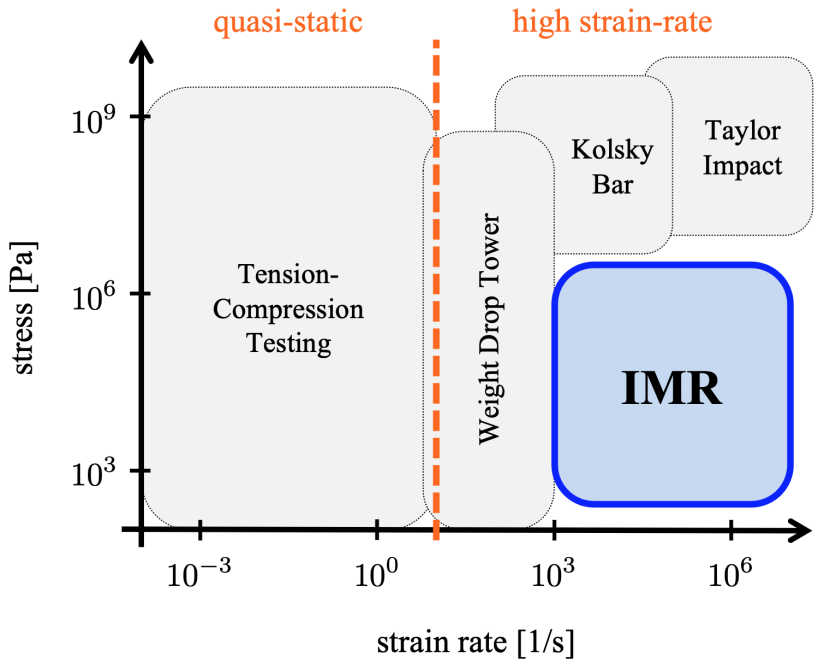

Figure 1.3: Lack of current material testing techniques to characterize soft materials at high strain rates (blue box).

strain-rates (blue box). The inertial bubble collapse rapidly causes large deformation in the soft materials, which enables us to characterize them at high strain-rates.

An example of applications that benefit from IMR is blast Traumatic Brain Injury (TBI) (Baughman Shively *et al.*, 2016; Franck, 2017). Military personnel and civilians in Iraq and Afghanistan have had a TBI as a result of blast exposure in war, and have reported symptoms such as headache, memory problems, depression and anxiety, though the damage mechanism and pathology still remain elusive. Brain cells are sensitive to local tissue strains and strain-rates (Bar-Kochba *et al.*, 2016) so that the mechanical response of brain tissue at high strain-rates needs to be quantitatively evaluated, which is possibly connected to injury criteria. Furthermore, microcavitation is hypothetically considered to be the damage mechanism in blast TBI (Goeller *et al.*, 2012; Franck, 2017). Baughman Shively *et al.* (2016) analyzed brain autopsy specimens and showed that the tissue damage was localized to internal brain interfaces which are capable of inducing tension and thus cavitation. The length scale of the tissue damage was also comparable with microcavitation bubbles. Therefore, IMR is an appropriate technique to characterize the brain tissue, and the study

of cavitation and bubble dynamics in soft matter is required not only to improve IMR but also to elucidate the origin of blast TBI.

1.1.2 Therapeutic ultrasound

Cavitation and bubble dynamics play an important role in a wide range of biomedical applications including therapeutic ultrasound (Bailey *et al.*, 2003; Mitragotri, 2005; Coussios & Roy, 2008; Brennen, 2015). In ultrasound drug delivery (Ibsen *et al.*, 2013), microbubbles are injected into the vasculature[2] and flow to pre-identified regions where focused ultrasound induces bubble break up and enables drug release. In histotripsy (Xu *et al.*, 2004; Bader *et al.*, 2019), ultrasound is focused into the body to induce inertial cavitation. The inertial collapse of bubbles results in rapid compression of the gas inside the bubbles to high pressures and temperatures, which can ablate a malignant tissue without using a surgical knife. These therapeutic ultrasound applications require a fundamental understanding of cavitation and bubble dynamics, specifically the interaction between ultrasound and bubbles in soft tissue.

1.2 Single bubble dynamics in soft matter

1.2.1 Spherical bubble dynamics

Motivated by IMR, blast TBI and therapeutic ultrasound, we analytically and experimentally study single bubble dynamics in soft matter. Cavitation and bubble dynamics have been studied for a long time, historically in water for naval applications (Plesset & Prosperetti, 1977; Brennen, 1995), and recently in soft matter for biomedical applications (Brujan, 2011; Dollet *et al.*, 2019), mostly based on continuum mechanics. Bubble dynamics are often studied analytically and experimentally, while some studies conduct direct simulations (e.g., Johnsen & Colonius, 2009; Beig & Johnsen, 2015), in which the full equations of motion are solved. However, direct simulations of bubble

[2]Bubble dynamics in blood (a non-Newtonian fluid) (Fung, 1993) could be studied in a fashion similar to those in soft matter presented in this thesis.

dynamics still has numerical challenges such as incorporating phase changes, surface tension and nonlinear elasticity of soft matter. In particular, conducting such a compressible simulation for a sufficiently long time (e.g., many cycles of ultrasound-induced bubble oscillations) is challenging because of the high computational cost. For these reasons, this study combines analytical and experimental approaches to study the single bubble dynamics in soft matter.

There have been many contributions to modeling single bubble dynamics under the assumption that the bubble retains its spherical shape. Oscillations of a spherical bubble in water were first described by the classical Rayleigh–Plesset equation (Rayleigh, 1917; Plesset, 1949). Compressible effects (Herring, 1941; Tomita & Shima, 1977; Keller & Miksis, 1980; Prosperetti & Lezzi, 1986; Lezzi & Prosperetti, 1987), heat diffusion effects (Prosperetti *et al.*, 1988; Kamath *et al.*, 1993; Preston, 2004; Stricker *et al.*, 2011), mass diffusion effects (Nigmatulin *et al.*, 1981; Akhatov *et al.*, 2001; Preston, 2004) and viscoelastic effects of soft matter (Allen & Roy, 2000a,b; Yang & Church, 2005; Hua & Johnsen, 2013; Gaudron *et al.*, 2015) were subsequently incorporated into the model. As a result, the description of spherical bubble dynamics in soft matter consists of several Ordinary Differential Equations (ODEs) and Partial Differential Equations (PDEs), which are solved numerically. This approach lays at the foundation of IMR (Estrada *et al.*, 2018) and is also used in the study of therapeutic ultrasound (Bader *et al.*, 2019). However, some limitations still remain in this model: the model has not been validated against experiments of nonlinear bubble oscillations in soft matter driven by ultrasound, and gas-vapor mixture transport inside the bubble is not fully understood.

Experiments of ultrasound-induced finite-amplitude oscillations have been challenging because bubbles oscillating in water have a tendency to break up (Brennen, 2002; Versluis *et al.*, 2010). Kameda & Matsumoto (1999) experimentally observed ultrasound-induced finite-amplitude oscillations of an air bubble in highly viscous silicone oil, which agreed with the model for spherical bubble dynamics. In contrast with experiments in Newtonian fluids, Hamaguchi & Ando (2015) experimentally observed ultrasound-induced small-amplitude oscillations of an air bubble in a gelatin gel and showed agreement with solutions to the linearized model. On the other hand,

experiments of finite-amplitude oscillations in soft matter are lacking, and thus limit validation of models including viscoelastic effects (Gaudron *et al.*, 2015) as well as understanding the role of viscoelasticity on ultrasound-induced bubble dynamics.

Contents of cavitation bubbles in water are usually vapor with a small amount of air, while a finite amount of non-condensible gas as well as vapor are expected to exist inside the laser-induced cavitation bubbles in soft materials, thus requiring an understanding of gas-vapor mixture transport in the bubble dynamics. Akhatov *et al.* (2001) studied the laser-induced collapse of a bubble in water, which contains vapor and a small amount of air, and showed that an air shell formed at the bubble wall traps the vapor inside the bubble, leading to milder bubble collapse. However, the role of gas-vapor mixture transport on the time evolution of bubble radius is not fully understood, which is of our interest for IMR. From a modeling standpoint, past studies (Hao *et al.*, 2017; Estrada *et al.*, 2018) relied on the assumption that the ratios of specific heats are the same for the non-condensible gas and vapor, which is a limitation and may not be valid for a bubble containing a finite amount of non-condensible gas.

1.2.2 Shape stability of a bubble

Another limitation of the theoretical-numerical cavitation model is the spherical assumption; bubbles often deviate from a spherical shape in practice. Predicting the onset of shape instabilities of a bubble is important to properly use IMR, which relies on calculating the spherical bubble radius (Estrada *et al.*, 2018). Shape stability is also important to predict the bubble break up in ultrasound drug delivery (Ibsen *et al.*, 2013) or to estimate the bubble collapse pressure in tissue ablation (Brennen, 2015). Shape stability analysis of a bubble was pioneered by Plesset (1954) and Prosperetti (1977b). The idea is to extend classical perturbation analysis on a plane interface such as Rayleigh–Taylor instability (Taylor, 1950) or Kelvin–Helmholtz instability (e.g., Kundu *et al.*, 2016, pp. 537-544)) to a spherical interface between a gas and water, where non-spherical perturbations are described by spherical harmonics. The analysis results in two ODEs: one for the base state (mean bubble radius), and the other for the perturbation amplitude. Prosperetti (1977b)

extended this non-spherical model by adding viscous rotational corrections. This non-spherical model has been used to investigate the shape stability of a bubble in water, primarily motivated by sonoluminescence (Brenner *et al.*, 1995; Hilgenfeldt *et al.*, 1996; Hao & Prosperetti, 1999; Brenner *et al.*, 2002), ultrasound drug delivery (Liu *et al.*, 2012, 2016) and sonochemistry (Zhang *et al.*, 2015, 2018; Klapcsik & Hegedüs, 2019). However, shape stability analysis has yet to be extended to a bubble in soft matter.

Two types of instability cause departures from a spherical bubble shape: parametric instability and Rayleigh–Taylor-type instability (Brenner *et al.*, 1995). Parametric instability usually occurs during ultrasound-induced oscillations. This instability is caused by parametric resonance between the mean bubble radius and the non-spherical perturbation, which is mathematically described by a Mathieu equation (Francescutto & Nabergoj, 1978). Parametric instability in water has been experimentally observed, which validated the shape stability analysis (Dollet *et al.*, 2008; Versluis *et al.*, 2010). Hamaguchi & Ando (2015) observed parametric instability in a gelatin gel, though shape stability analysis in soft matter was not available at that point. Rayleigh–Taylor-type instability is often induced during inertial collapse when the surrounding water is strongly accelerated into the gas inside the bubble and vice versa (Hilgenfeldt *et al.*, 1996; Brennen, 2002). However, experimental observation is challenging because the time scale of this instability is too small. In fact, as shown in the example of IMR in figure 1.2, experiments usually cannot capture the bubble at its minimum size during inertial collapse because of the limited resolutions of high-speed cameras, where the Rayleigh–Taylor-type instability is likely to occur. Therefore, we need to rely on an analytical approach to investigate the bubble behavior between the two snapshots in experiments, though this instability in soft matter has not been studied due to the lack of the non-spherical model.

1.3 Thesis overview

This thesis contributes to the understanding of spherical and non-spherical bubble dynamics in soft matter. The overall goal is to understand and improve a theoretical-numerical cavitation model used in IMR to appropriately predict the inertial bubble collapse in soft materials. The fundamental studies in this thesis would also be important ingredients for the blast TBI and therapeutic ultrasound. The analysis is based on continuum mechanics, and models for spherical and non-spherical bubble dynamics are derived from conservation laws. These mathematical models are numerically solved to investigate the bubble dynamics and compared with experiments to discuss the validity. The specific objectives of this thesis are:

- Validate a model for spherical bubble dynamics including viscoelastic effects against experiments of ultrasound-induced finite-amplitude oscillations in a hydrogel, and investigate the role of viscoelasticity on ultrasound-induced bubble dynamics.

- Develop a model for spherical gas-vapor bubble dynamics that accounts for variations in the ratio of specific heats of the mixture, and investigate the role of gas-vapor mixture transport on the inertial bubble collapse.

- Develop a model for non-spherical bubble dynamics in soft matter by extending classical perturbation analysis to a spherical interface between a gas and a soft solid.

- Investigate two types of shape instability of a bubble in soft matter: parametric instability during ultrasound-induced oscillations, and Rayleigh–Taylor-type instability during inertial collapse.

CHAPTER 2

Ultrasound-induced Oscillations of a Gas Bubble in Soft Matter

This chapter is adapted from Murakami *et al.* (2020b).

2.1 Introduction

We experimentally and numerically study ultrasound-induced nonlinear oscillations of a gas bubble in soft matter to investigate the role of viscoelasticity on the bubble dynamics. A fundamental understanding of the interaction between ultrasound and bubbles in soft tissue is required for therapeutic ultrasound applications (Bailey *et al.*, 2003; Mitragotri, 2005; Coussios & Roy, 2008; Brennen, 2015). A model for spherical bubble dynamics was proposed in past studies (Rayleigh, 1917; Plesset, 1949; Keller & Miksis, 1980; Prosperetti *et al.*, 1988; Gaudron *et al.*, 2015; Estrada *et al.*, 2018), which includes viscoelastic effects of soft matter, while validation studies for ultrasound-induced finite-amplitude oscillations in soft matter are still lacking. This mathematical model is also used in Inertial Microcavitation high strain-rate Rheometry (IMR) (Estrada *et al.*, 2018). In this chapter, we validate the model against experiments of ultrasound-induced bubble oscillations in a hydrogel, and then investigate the role of viscoelasticity of the gel on the bubble dynamics. The experimental data in this chapter were provided by Mr. Yushi Yamakawa and Prof. Keita Ando from Keio University.

Starting from the conservation laws of continuum mechanics, we review Rayleigh–Plesset-type models for spherical bubble dynamics in soft matter. Note that some assumptions (e.g., homobaric, cold liquid) introduced in this chapter continue to be used throughout this thesis. In the experi-

ments, the lower ultrasound frequency of 28 kHz is used to obtain sufficient temporal and spatial resolutions of the bubble dynamics, though a megasonic wave is often used in the therapeutic ultrasound. Transparent hydrogels are convenient to visualize the bubble dynamics in soft matter (Barney *et al.*, 2020) so that a 6 wt% gelatin gel is used as a tissue-mimicking medium. Viscoelastic properties of gels driven by ultrasound at the frequency of 10-50 kHz substantially differ from those measured by commercial rheometers under quasi-static conditions (Jamburidze *et al.*, 2017; Saint-Michel & Garbin, 2020) and thus need to be treated as unknown parameters. We first experimentally observe small-amplitude bubble oscillations to obtain the viscosity and shear modulus of the gelatin gel by comparing with a linear solution of the model (Hamaguchi & Ando, 2015). Thereafter, the model is validated against experiments of finite-amplitude bubble oscillations. Furthermore, a resonance curve of the bubble oscillations is constructed to elucidate the features of ultrasound-induced bubble dynamics. Lastly, the dependence of the bubble dynamics on the viscoelasticity is numerically examined.

2.2 Modeling of spherical bubble dynamics in soft matter

2.2.1 Principles and assumptions

The analysis of single bubble dynamics in this study is based on continuum mechanics. Given the bubble size of interest $R \approx 100\,\mu$m and the mean free path of air molecules at room temperature and atmospheric pressure $l \approx 56$ nm, the Knudsen number is much less than unity (Kn $= l/R \ll 1$), thus the continuum assumption is acceptable. During the bubble collapse ($R \approx 1\ \mu$m), the air inside the bubble is compressed ($l \ll 56$ nm) so that the continuum assumption is expected to be maintained. The soft matter surrounding the bubble is considered to be homogeneous; if the soft biological tissue is heterogeneous, its length scale must be much smaller than the bubble size as well. The gas inside the bubble and the soft solid surrounding the bubble follow conservation laws:

conservation of mass, momentum and energy,

$$\frac{\partial \rho}{\partial t} + \frac{\partial}{\partial x_i}(\rho u_i) = 0, \tag{2.1}$$

$$\frac{\partial}{\partial t}(\rho u_j) + \frac{\partial}{\partial x_i}(\rho u_i u_j) = \frac{\partial}{\partial x_i}(\mathsf{T}_{ij}), \tag{2.2}$$

$$\frac{\partial}{\partial t}\left[\rho\left(e + \frac{1}{2}u_j^2\right)\right] + \frac{\partial}{\partial x_i}\left[\rho\left(e + \frac{1}{2}u_j^2\right)u_i\right] = \frac{\partial}{\partial x_i}(\mathsf{T}_{ij}u_j) - \frac{\partial q_i}{\partial x_i}, \tag{2.3}$$

where t is time, x_i is the spatial coordinate, ρ is the density, u_i is the velocity field, T_{ij} is the stress tensor, e is the internal energy and q_i is the heat flux vector. Gravity is neglected in the analysis.

We study spherical bubble dynamics, which are applicable in the situations where no mechanism break the problem symmetry (e.g., the presence of a neighboring object). The analysis relies on two significant assumptions:

- Physical phenomena are spherically symmetric
- Pressure inside a bubble is homobaric

Given the spherically symmetric assumption, the analysis starts from the one-dimensional radial component of conservation laws in spherical coordinates, where the origin is located at the bubble center (see figure 2.1). The homobaric assumption means that the pressure field inside the bubble is uniform $p_b = p_b(t)$, although the temperature field is not uniform $T = T(r, t)$ where r is the radial distance (Prosperetti *et al.*, 1988; Lin *et al.*, 2002; Zhou & Prosperetti, 2020). An important feature of the bubble dynamics is that the surrounding soft solid (or liquid) has a much larger density than that of the inside gas so that gas inertia is negligible. Prosperetti *et al.* (1988) showed that gas pressure gradient is balanced with gas inertia and is written by the bubble wall Mach number and the ratio between the bubble size and a wavelength of pressure perturbations, which are sufficiently small because of the huge density difference between the gas and surroundings. This scaling analysis allows us to use the homobaric assumption. These two assumptions make a number of analysis feasible in the bubble dynamics. In this study, we have an additional assumption:

- Temperature of soft solid is constant at room temperature T_∞

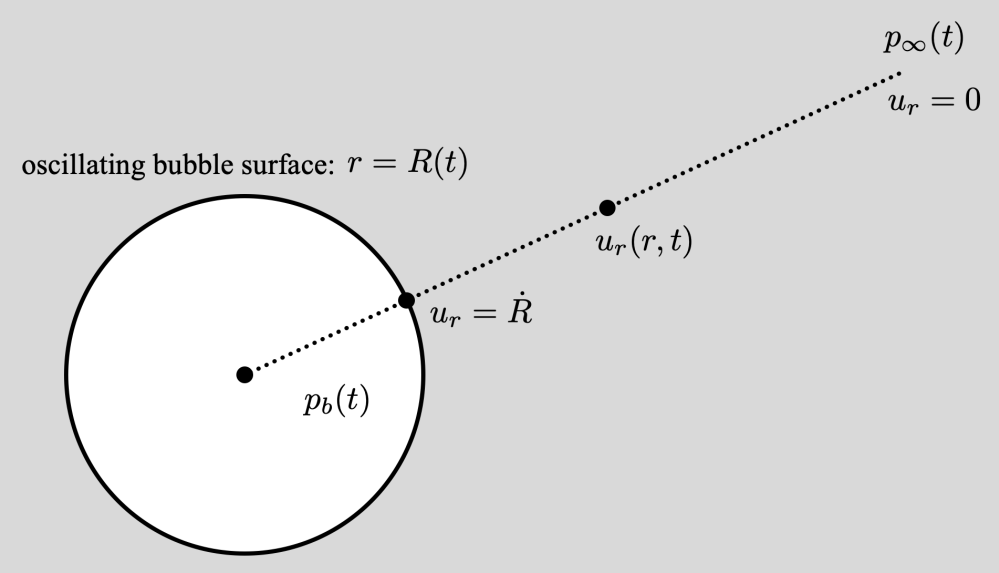

Figure 2.1: Coordinates for a spherical bubble in a soft solid.

This is "cold liquid" assumption, which is reasonable because the volumetric heat capacity of soft solid is much larger than that of gas (Prosperetti *et al.*, 1988; Preston *et al.*, 2007; Barajas & Johnsen, 2017). Note that reducing the spherically symmetric and homobaric assumptions is challenging, while the cold liquid assumption can be reduced by solving the energy equation for the surrounding soft solid[1] (Kamath *et al.*, 1993; Preston, 2004; Stricker *et al.*, 2011).

2.2.2 Mathematical model

We consider an oscillating spherical bubble of radius $R(t)$ in an infinite soft solid of constant density ρ_∞ and temperature T_∞, as shown in figure 2.1. Assuming incompressible and irrotational motion of the soft solid, the radial velocity field $u_r(r,t)$ ($r \geq R$) is determined by the potential flow theory. The classical Rayleigh–Plesset equation is derived by integrating the conservation of momentum (2.2) from the oscillating bubble surface to infinity (Rayleigh, 1917; Plesset, 1949; Brennen, 1995),

$$R\ddot{R} + \frac{3}{2}\dot{R}^2 = \frac{1}{\rho_\infty}\left(p_b - p_\infty - \frac{2\sigma}{R} + S\right), \tag{2.4}$$

[1] It is important to keep in mind that the Keller–Miksis equation (2.5) is also derived under the cold liquid assumption. The thermodynamic state of the soft solid is determined by two variables: one is the cold liquid temperature T_∞ and the other is the pressure or the enthalpy (Keller & Miksis, 1980; Prosperetti & Lezzi, 1986).

where the dot represents the temporal derivative, σ is the surface tension and S is the stress integral. The homobaric bubble pressure $p_b(t)$ and far-field pressure $p_\infty(t)$ are incorporated through the boundary conditions at the bubble surface and infinity. In short, the Rayleigh–Plesset equation (2.4) is a semi-analytical solution of the conservation laws (2.1) to (2.3) for the soft solid surrounding the bubble, which is written with respect to the bubble radius $R(t)$ rather than the radial velocity field $u_r(r,t)$. Note that conservation of energy (2.3) is not solved because we have the cold liquid assumption $T(r,t) = T_\infty$ $(r \geq R)$.

Compressible effects in the soft solid are important for large-amplitude bubble oscillations, which are incorporated as follows. The Mach number is defined as $\mathrm{Ma} = \dot{R}/c_\infty$ where $\dot{R}$ is the bubble wall velocity and c_∞ is the sound speed of the soft solid. Simplified singular-perturbation analysis of the Rayleigh–Plesset equation (2.4) to the first-order in the Mach number results in the Keller–Miksis equation (Keller & Miksis, 1980; Prosperetti & Lezzi, 1986), which is also reviewed by Estrada *et al.* (2018),

$$R\ddot{R}\left(1-\frac{\dot{R}}{c_\infty}\right)+\frac{3}{2}\dot{R}^2\left(1-\frac{\dot{R}}{3c_\infty}\right)=\frac{1}{\rho_\infty}\left(1+\frac{\dot{R}}{c_\infty}+\frac{R}{c_\infty}\frac{d}{dt}\right)\left(p_b-p_\infty-\frac{2\sigma}{R}+S\right). \tag{2.5}$$

Note that this weakly compressible Keller–Miksis equation (2.5) reduces to the incompressible Rayleigh–Plesset equation (2.4) as $c_\infty \to \infty$.

The viscoelastic nature of the soft solid is modeled by a Kelvin–Voigt constitutive equation consisting of a damper and a spring in parallel as shown in figure 2.2, with Newtonian viscosity and (nonlinear) neo-Hookean elasticity. The stress integral S can be evaluated to yield (Gaudron *et al.*, 2015)

$$S=-\frac{4\mu\dot{R}}{R}-\frac{G}{2}\left[5-4\frac{R_{eq}}{R}-\left(\frac{R_{eq}}{R}\right)^4\right], \tag{2.6}$$

where μ and G are the constant viscosity and shear modulus, and R_{eq} is the equilibrium bubble radius. This viscoelastic model has been validated by experiments of bubble dynamics in hydrogels, including ultrasound-induced linear oscillations in a gelatin gel (Hamaguchi & Ando, 2015) and

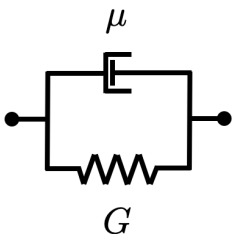

Figure 2.2: A Kelvin–Voigt viscoelastic model.

laser-induced inertial collapse in a polyacrylamide gel (Estrada *et al.*, 2018), while experiments of ultrasound-induced nonlinear oscillations are still lacking for this validation study.

A model for the homobaric bubble pressure $p_b(t)$ is derived from the conservation laws (2.1) to (2.3) for the gas inside the bubble in conjunction with an equation of state (ideal gas law). In this chapter, we assume that the bubble consists of non-condensible gas (air) only; no vapor is present[2]. This assumption is reasonable because the gelatin gel in our experiments is air-supersaturated (see section 2.3). The homobaric bubble pressure therefore obeys the following Ordinary Differential Equation (ODE) (Prosperetti *et al.*, 1988):

$$\dot{p}_b = \frac{3}{R}\left[-\gamma p_b \dot{R} + (\gamma - 1)K \left.\frac{\partial T}{\partial r}\right|_w\right], \tag{2.7}$$

where γ is the ratio of specific heats, $K(T)$ is the thermal conductivity of the gas, and w denotes the value evaluated at the bubble wall $r = R(t)$. We use the temperature-dependent thermal conductivity (Prosperetti *et al.*, 1988),

$$K(T) = AT + B, \tag{2.8}$$

where A and B are the fitting coefficients. This approximation of thermal conductivity is discussed in greater detail in section 3.2.2 in chapter 3. The temperature field $T(r, t)$ inside the bubble is

[2] A model for gas-vapor mixture is introduced in chapter 3 with full derivation process from the conservation laws (2.1) to (2.3).

determined by the Partial Differential Equation (PDE):

$$\rho C_p \left(\frac{\partial T}{\partial t} + u_r \frac{\partial T}{\partial r} \right) = \dot{p}_b + \frac{1}{r^2} \frac{\partial}{\partial r} \left(r^2 K \frac{\partial T}{\partial r} \right), \tag{2.9}$$

where C_p is the specific heat of the gas at constant pressure. The radial velocity field inside the bubble ($0 \leq r \leq R$) is given by

$$u_r(r,t) = \frac{1}{\gamma p_b} \left[-\frac{1}{3} r \dot{p}_b + (\gamma - 1) K \frac{\partial T}{\partial r} \right]. \tag{2.10}$$

The gas follows the ideal gas law $p_b = \rho \mathcal{R} T$ where $\mathcal{R}$ is the gas constant. The boundary conditions are $\partial T / \partial r|_{r=0} = 0$ at the origin and the cold liquid assumption $T(r = R, t) = T_\infty$ at the bubble wall.

The surrounding soft solid is possibly under pre-strain where the bubble pressure is

$$p_{b,0} = p_{atm} + \frac{2\sigma}{R_0} + \frac{G}{2} \left[5 - 4 \frac{R_{eq}}{R_0} - \left(\frac{R_{eq}}{R_0} \right)^4 \right], \tag{2.11}$$

where p_{atm} is the atmospheric pressure and R_0 is the bubble radius with pre-strain. In this chapter, the ratio of the equilibrium bubble radius to the bubble radius with pre-strain (see figure 2.4) is set to $R_{eq}/R_0 = 0.6$, which is close to the prediction of Ando & Shirota (2019). Note that we found that this ratio has a small impact on the bubble oscillations at least in our problems.

In summary, the dynamics of a spherical gas bubble in soft matter are described by solving the two ODEs and one PDE simultaneously[3]: the Keller–Miksis equation (2.5), the ODE for homobaric bubble pressure (2.7) and the PDE for temperature (2.9), where the radial velocity is given by equation (2.10). The model is solved numerically: we semi-discretize the PDE (2.9) by finite differences, and integrate in time by the Cash–Karp Runge–Kutta method (Press *et al.*, 2007, pp. 910-915). We use the normalized radial coordinate $y = r/R(t)$, and the computational domain ranges $0 \leq y \leq 1$ where the number of uniform spatial mesh is set to $N_y = 200$. The dimensionless form is available in Appendix A.2. We choose the characteristic length and time as $L_c = R_{eq}$ and

[3]We call this "pure gas model" in contrast with the "gas-vapor model" introduced in chapter 3.

Property	Value
γ	1.4
M	28.97 g/mol
C_p	1.00 kJ/(kg · K)
A	5.3×10^{-5} W/m · K^2
B	1.17×10^{-2} W/m · K

Table 2.1: Physical properties of air. The gas constant is $\mathcal{R} = \mathcal{R}_u/M$ where $\mathcal{R}_u = 8.314$ kJ/(kmol · K) is the universal gas constant and M is the molecular weight.

Property	Value
ρ_∞	1020 kg/m^3
c_∞	1567 m/s
σ	0.040 N/m
μ	18.3 mPa · s
G	4.0 kPa

Table 2.2: Physical properties of a 6 wt% gelatin gel. The viscosity μ and shear modulus G are fitted through the linear theory (see section 2.4).

$T_c = 1/f_d$ where f_d is the driving frequency. The initial conditions are set to $R(t = 0) = R_0$, $\dot{R}(t = 0) = 0$, $p_b(t = 0) = p_{b,0}$ and $T(r, t = 0) = T_\infty$. The physical properties of air and the 6 wt% gelatin gel at Standard Temperature and Pressure (STP) ($T_\infty = 298.15$ K and $p_{atm} = 101.3$ kPa) are listed in tables 2.1 and 2.2, respectively.

2.2.3 Linear theory

The Rayleigh–Plesset equation (2.4) is linearized to enable us to obtain the viscosity and shear modulus of the gel from its comparison with small-amplitude bubble oscillations (Hamaguchi & Ando, 2015). The bubble response to the sinusoidal acoustic pressure $p_a(t) = C_d \cos(2\pi f_d t)$ with sufficiently small amplitude C_d and frequency f_d is expected to be linear ($R = R_0(1 + \mathsf{x})$ where $\mathsf{x} \ll 1$) and the bubble contents tend to behave polytropically. In this limit, the Rayleigh–Plesset equation (2.4) reduces to the linear ODE of a mass-damper-spring system:

$$\mathsf{m}\ddot{\mathsf{x}} + \mathsf{c}\dot{\mathsf{x}} + \mathsf{k}\mathsf{x} = C_d \cos(2\pi f_d t), \tag{2.12}$$

where the mass, damping and spring constants are given by

$$\mathsf{m} = \rho_\infty R_0^2, \quad \mathsf{c} = 4\mu_{\text{eff}}, \quad \mathsf{k} = 3\kappa_{\text{eff}} p_{b,0} - \frac{2\sigma}{R_0} + 2G\left[\frac{R_{eq}}{R_0} + \left(\frac{R_{eq}}{R_0}\right)^4\right]. \tag{2.13}$$

The effective polytropic index and viscosity κ_{eff} and μ_{eff} are given by (Chapman & Plesset, 1971; Prosperetti, 1977a; Ando *et al.*, 2009),

$$\kappa_{\text{eff}} = \frac{1}{3}\Re\{\Upsilon\}, \quad \mu_{\text{eff}} = \mu + \frac{p_{b,0}}{8\pi f_d}\Im\{\Upsilon\} + \frac{\rho_\infty (2\pi f_d)^2 R_0^3/(4c_\infty)}{1 + (2\pi f_d R_0/c_\infty)^2}, \tag{2.14}$$

where Υ is the complex transfer function of the Peclet number $\text{Pe} = R_0^2(2\pi f_d)/D_h$ where $D_h = K(T_\infty)/\rho_\infty C_p$ is the thermal diffusivity,

$$\Upsilon = \frac{3\gamma}{1 - 3(\gamma - 1)i\,\text{Pe}^{-1}(\sqrt{i\,\text{Pe}}\coth\sqrt{i\,\text{Pe}} - 1)}. \tag{2.15}$$

Note that the nonlinear elastic term of the pre-strain still remains in equations (2.11) and (2.13), regardless of whether the bubble response is linear or nonlinear. When the pre-strain is assumed to vanish (i.e., $R_0 = R_{eq}$), this elastic model reduces to the linear model of Hamaguchi & Ando (2015).

The steady-state solution of the linearized equation (2.12) is given by

$$\mathsf{x}(t) = X\cos(2\pi f_d t + \delta), \tag{2.16}$$

where X and δ are the oscillation amplitude and phase shift,

$$X = \frac{C_d/\mathsf{k}}{\sqrt{[1 - (f_d/f_N)^2]^2 + 4\zeta^2(f_d/f_N)^2}}, \tag{2.17}$$

$$\delta = \arctan\frac{2\zeta(f_d/f_N)}{1 - (f_d/f_N)^2}, \tag{2.18}$$

where f_N and ζ are the natural frequency and damping ratio, respectively,

$$f_N = \frac{1}{2\pi}\sqrt{\frac{k}{m}}, \quad \zeta = \frac{c}{2\sqrt{mk}}, \tag{2.19}$$

with which the resonant frequency f_R is defined as

$$f_R = \sqrt{1-\zeta^2} f_N. \tag{2.20}$$

2.3 Experiments

The experiments were conducted by Mr. Yushi Yamakawa and Prof. Keita Ando from Keio University. A 6 wt% air-supersaturated gelatin gel is used as the soft matter in the experiments. The gelatin extracted from porcine skin (G 2500, Sigma-Aldrich) and water are mixed and heated, and the solutions are poured into an acrylic case (38 mm × 38 mm × 15 mm) whose bottom is sealed with a thin plastic wrap. The solutions turn to a gel after overnight cooling at 4 °C. The gel returns to room temperature by being soaked in a water tank, and is supersaturated with dissolved air (Hamaguchi & Ando, 2015).

A spherical bubble nucleus is generated in the gelatin gel by focusing a Q-switched Nd:YAG laser pulse (ULTRA 50 GRM, Quantel) through a microscope objective, as illustrated in figure 2.3 (a). Since the surrounding gel is supersaturated, the bubble exhibits gradual growth due to the gas influx in the order of minutes, as shown in figure 2.3 (b) and (c). The bubble radius R_0 can be controlled by utilizing this mass diffusion. Figure 2.4 (a) is the bubble nucleus right after the laser focusing, which eventually finishes to grow within a couple of hours and then starts to shrink due to the gas outflux back into the gel. In the end, the gas inside the bubble completely dissolves into the gel, leaving structural damage as shown in figure 2.4 (b). We interpret the radius of this structural damage as the equilibrium radius R_{eq}. The relation between the equilibrium radius R_{eq} and the bubble radius in the pre-strained gel R_0 is depicted in figure 2.4 (c).

The bubble oscillations driven by the ultrasound emitted from a 28 kHz planner piezoelectric

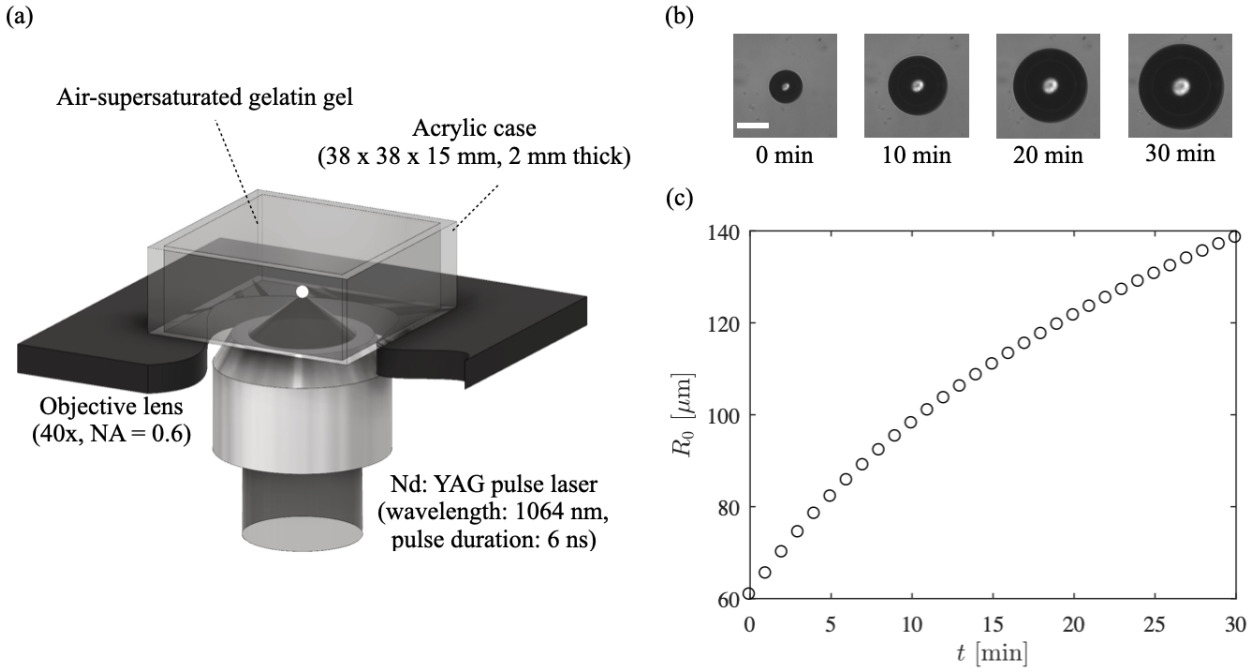

Figure 2.3: The spherical bubble in a gelatin gel generated by focusing a laser pulse and its growth driven by the mass diffusion. (a) The optical system to generate a bubble by focusing a laser pulse. (b) Snapshots of the growing bubble in the 6 wt% air-supersaturated gelatin gel. The scale bar represents 100 μm. (c) The evolution of the area-equivalent bubble radius (obtained from (b)).

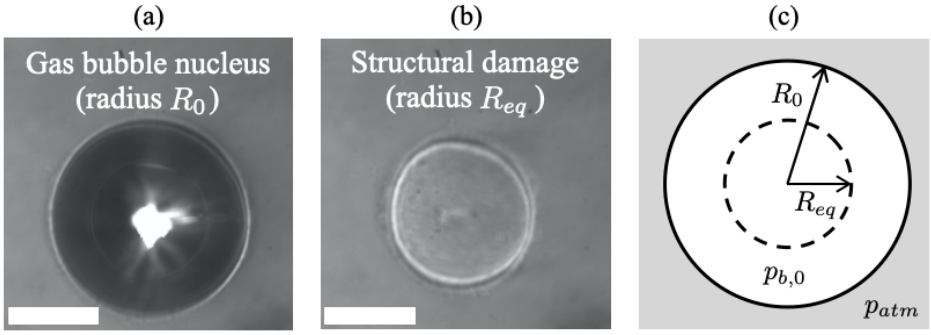

Figure 2.4: A gas bubble nucleus and structural damage in a gelatin gel. (a) A gas bubble nucleus in a gelatin gel right after the laser focusing. (b) Structural damage after the gas bubble completely dissolves into the surrounding gel. (c) Schematic illustration of the bubble radius with pre-strain R_0 and the equilibrium bubble radius R_{eq}. The scale bar represents 50 μm.

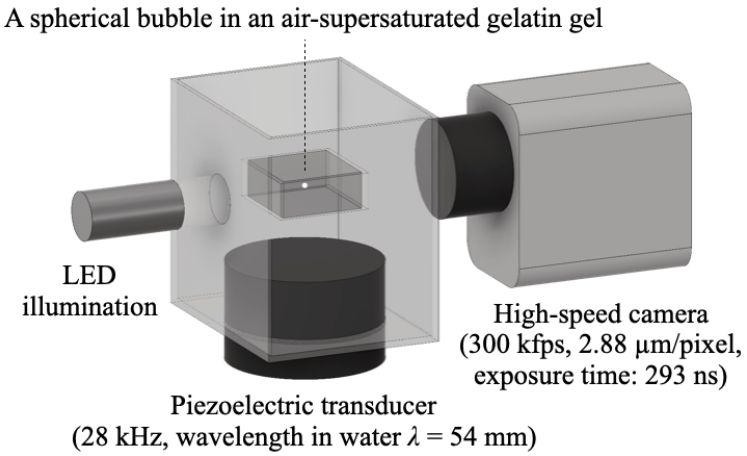

Figure 2.5: Schematic illustration of the experimental setup for recording the bubble oscillations driven by a 28 kHz planar ultrasound. The bubble is placed at one half of the ultrasound wavelength above the piezoelectric transducer.

transducer (0.028Z45I, JAPAN PROBE) are recorded by a high-speed camera (FASTCAM SA-X2, Photron), as illustrated in figure 2.5. The transducer is attached on the bottom of an acrylic container filled with tap water. The distance between the transducer and the free surface of the tap water is set to $5\lambda/4$ where λ is the ultrasound wavelength, in order to form a standing-wave-like pressure field (Yamashita & Ando, 2020). The bubble generated in the gel is placed at the antinode of the standing wave (i.e., $\lambda/2$ above the transducer). The acoustic pressure $p_a(t)$ in the water (without the gel sample) is measured by a hydrophone (HCT0310, Onda). The acoustic pressure in the gel is expected to be similar to the underwater pressure because their acoustic impedances are similar.

In short, there are two parameters to be controlled in the experiments:

- Bubble radius with pre-strain R_0
- Ultrasound pressure amplitude $p_A = \max(p_a)$

The first is controlled through the gradual bubble growth driven by mass diffusion, and the second is set from 0.03 atm to 0.24 atm. On the other hand, the gelatin concentration and ultrasound frequency are fixed at 6 wt% and $f_d = 28$ kHz, respectively.

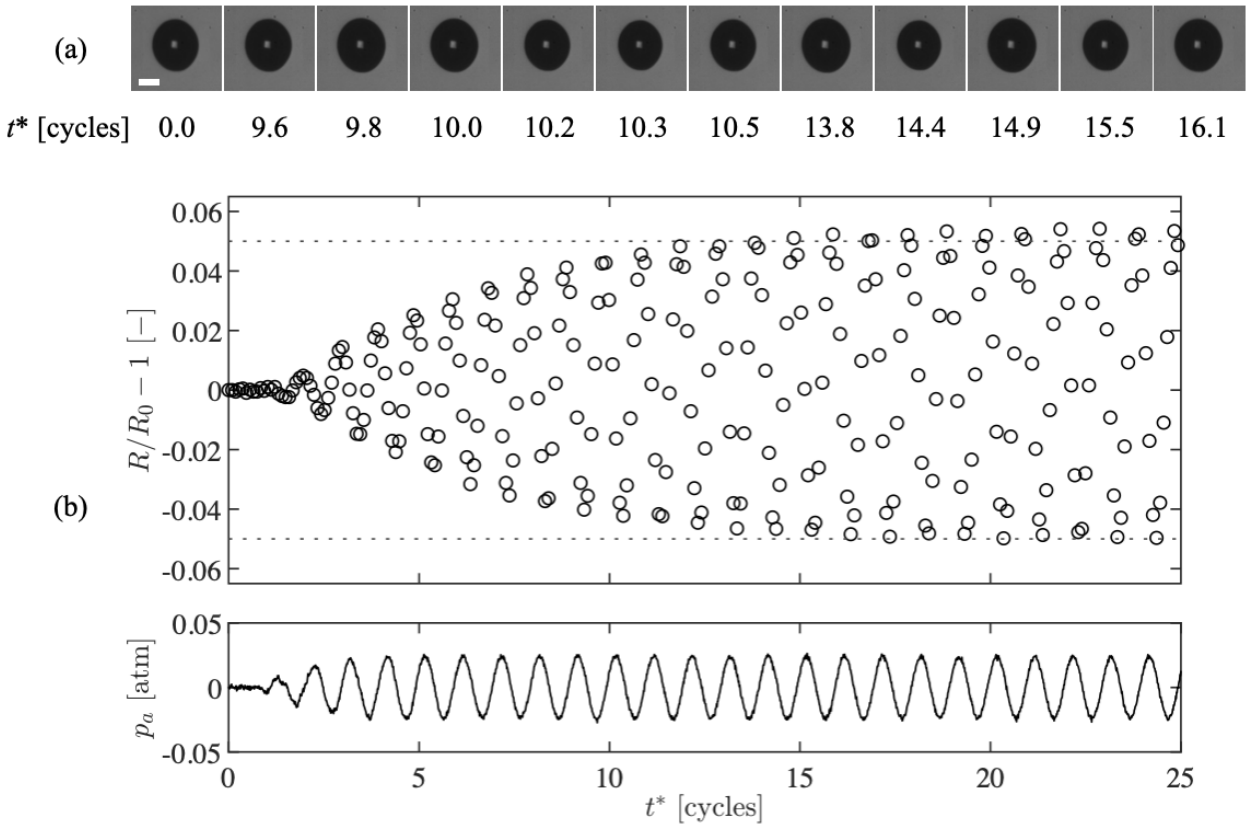

Figure 2.6: Small-amplitude oscillations of a spherical bubble in the 6 wt% gelatin gel driven by 28 kHz ultrasound ($R_0 = 115.9$ μm, $f_d/f_R = 1.00$). (a) A series of the recorded images. The scale bar represents 100 μm. (b) Evolution of the area-equivalent radius (top) and the ultrasound pressure wave with $p_A \approx 0.03$ atm (bottom).

2.4 Small-amplitude bubble oscillations

We first experimentally observe small-amplitude bubble oscillations and obtain the viscosity and shear modulus of the 6 wt% gelatin gel by comparing with the linear solution introduced in section 2.2.3. As a representative example, figure 2.6 shows the experimental results of the bubble with $R_0 = 115.9$ μm (under resonance $f_d/f_R = 1.00$) driven by low-amplitude ultrasound pressure $p_A = 0.03$ atm. A series of the recorded images in figure 2.6 (a) show that the bubble maintains its spherical shape during the oscillations. The evolution of the area-equivalent radius in figure 2.6 (b) shows that the oscillation amplitude during both growth and shrinking phases is approximately $0.05R_0$, thus the oscillation amplitude is sufficiently small for the dynamics to be linearized.

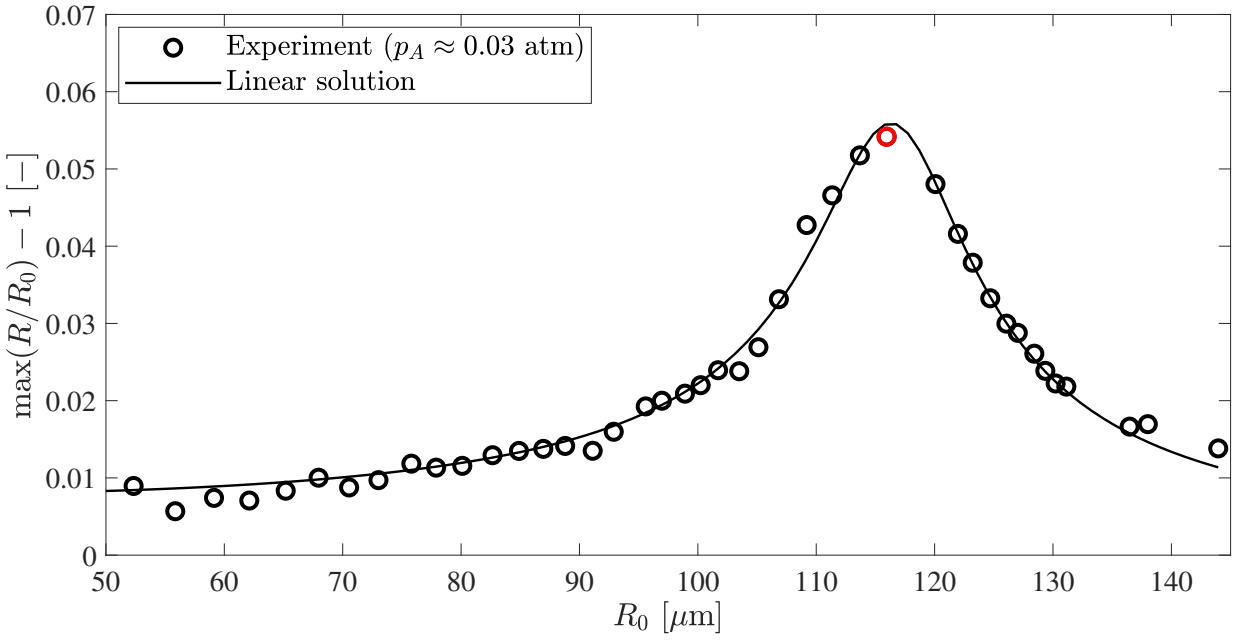

Figure 2.7: Resonance curve of the small-amplitude bubble oscillations driven by 28 kHz ultrasound with $p_A \approx 0.03$ atm as a function of the bubble radius with pre-strain R_0. The circles represent the experimental results, in which the red one corresponds to the case in figure 2.6. The solid line is the linear solution (2.17) with the fitted viscosity $\mu = 18.3$ mPa · s and shear modulus $G = 4.0$ kPa for the 6 wt% gelatin gel.

Starting from the bubble nucleus of $R_0 \approx 50\,\mu$m, the same experiment as in figure 2.6 but with increasing the bubble radius R_0 was repeated to construct the resonance curve as shown in figure 2.7. This resonance curve is the relation between the oscillation amplitude max(R) and the bubble radius with pre-strain R_0. The experimental results with different R_0 are represented by circles, in which the red one corresponds to the resonant case in figure 2.6. Since the oscillation amplitude is sufficiently small, we compare the resonance curve with the linear solution to obtain the viscosity and shear modulus of the gel. The linear solution of the oscillation amplitude (2.17) is fitted to the experimental data through the least squares method. The fitted linear solution agrees well with the experimentally determined resonance curve, where the fitting parameters of the viscosity and shear modulus are $\mu = 18.3$ mPa · s and $G = 4.0$ kPa, respectively.

2.5 Finite-amplitude bubble oscillations

2.5.1 Experimental and numerical results

We experimentally and numerically study ultrasound-induced finite-amplitude oscillations of a gas bubble, and discuss the validity of the mathematical model introduced in section 2.2.2. Figure 2.8 (a) shows the experimental results of the bubble with $R_0 = 124.0\,\mu$m ($f_d/f_R = 1.06$) driven by high-amplitude ultrasound pressure $p_A = 0.24$ atm. The evolution of the corresponding area-equivalent radius is shown in figure 2.8 (b), where the oscillation amplitude during the growth phase is approximately $0.3R_0$ while that during the shrinking phase is smaller, indicating the nonlinearity of the dynamics. Numerical solutions of the model with the viscosity and shear modulus fitted through the linear theory are also shown in figure 2.8 (b). In the numerical simulation, the far-field pressure in the Keller–Miksis equation (2.5) is given by $p_\infty(t) = p_{atm} + p_a(t)$, provided that the wavelength of the ultrasound is sufficiently larger than the bubble size[4]. The comparison between the experiment and simulation shows good agreement, which implies the validity of the Rayleigh–Plesset-type model coupled with the Kelvin-Voigt constitutive equation with neo-Hookean elasticity.

When the oscillation amplitude is even larger, we experimentally observed that the bubble eventually starts non-spherical oscillations. Figure 2.9 (a) shows the experimental results of the bubble with $R_0 = 107.8\,\mu$m ($f/f_R = 0.93$) driven by high-amplitude ultrasound pressure $p_A = 0.24$ atm. The bubble initially oscillates spherically, but non-spherical oscillations of mode 1 (translational motion) appear after $t^* \approx 13.0$. Note that non-spherical oscillations of mode 1 cannot occur in water (Prosperetti, 1977b; Versluis *et al.*, 2010; Liu *et al.*, 2012), but can occur in our case because the gelatin gel possesses the elasticity which works as restoring force in the translational direction, as predicted by the analysis of Murakami *et al.* (2018, 2020a) (see chapter 5). Figure 2.9 (b) shows the evolution of the area-equivalent radius from the experiments compared with the numerical solutions of the model. Although the comparison shows reasonable agreement initially,

[4]The far-field pressure cannot have polar and azimuthal dependence due to the spherically symmetric assumption.

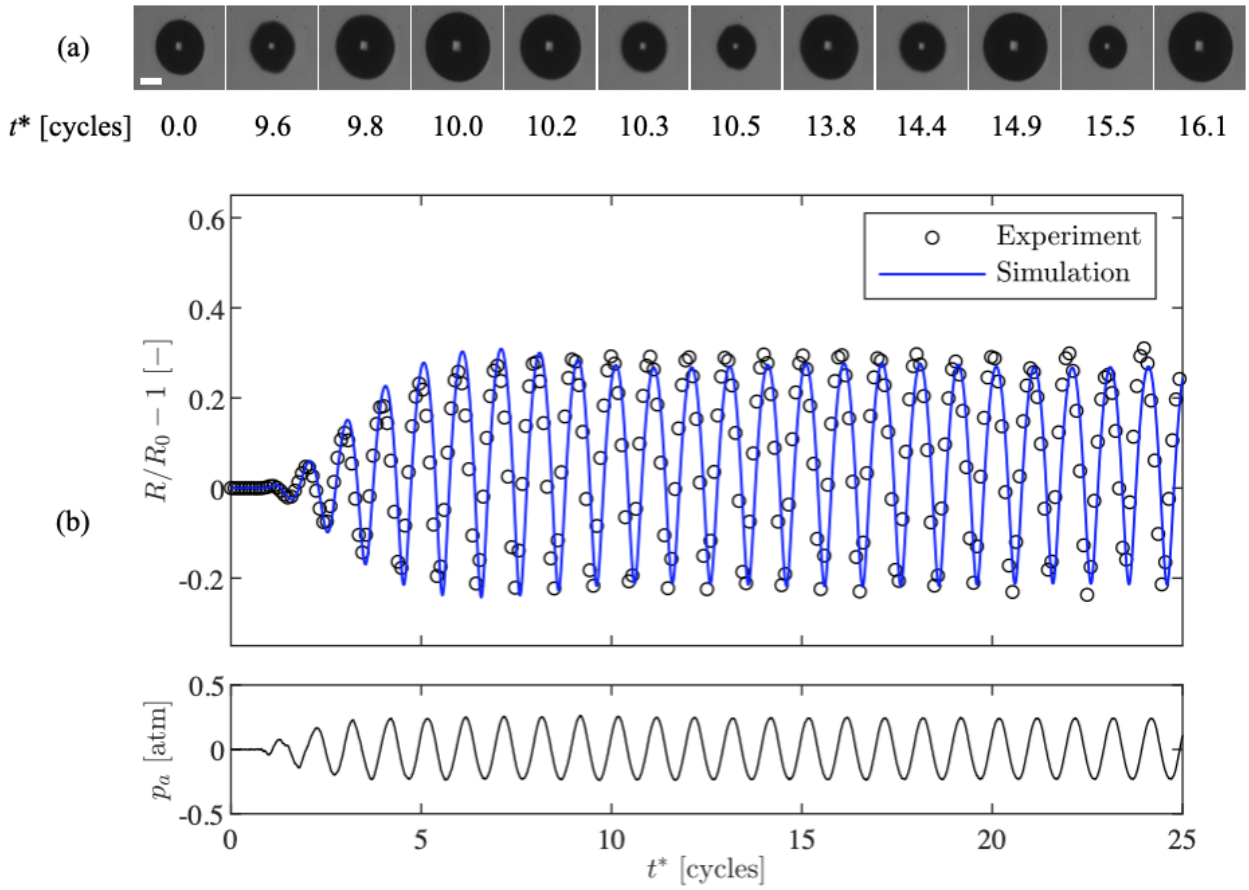

Figure 2.8: Finite-amplitude oscillations of a spherical bubble in the 6 wt% gelatin gel driven by 28 kHz ultrasound ($R_0 = 124.0\ \mu$m, $f/f_R = 1.06$). (a) A series of the recorded images. The scale bar represents 100 μm. (b) Evolution of the area-equivalent radius compared with numerical solutions of the model with the viscosity $\mu = 18.3$ mPa $\cdot$ s and shear modulus $G = 4.0$ kPa fitted through the linear theory (top) and the ultrasound pressure wave with $p_A \approx 0.24$ atm (bottom).

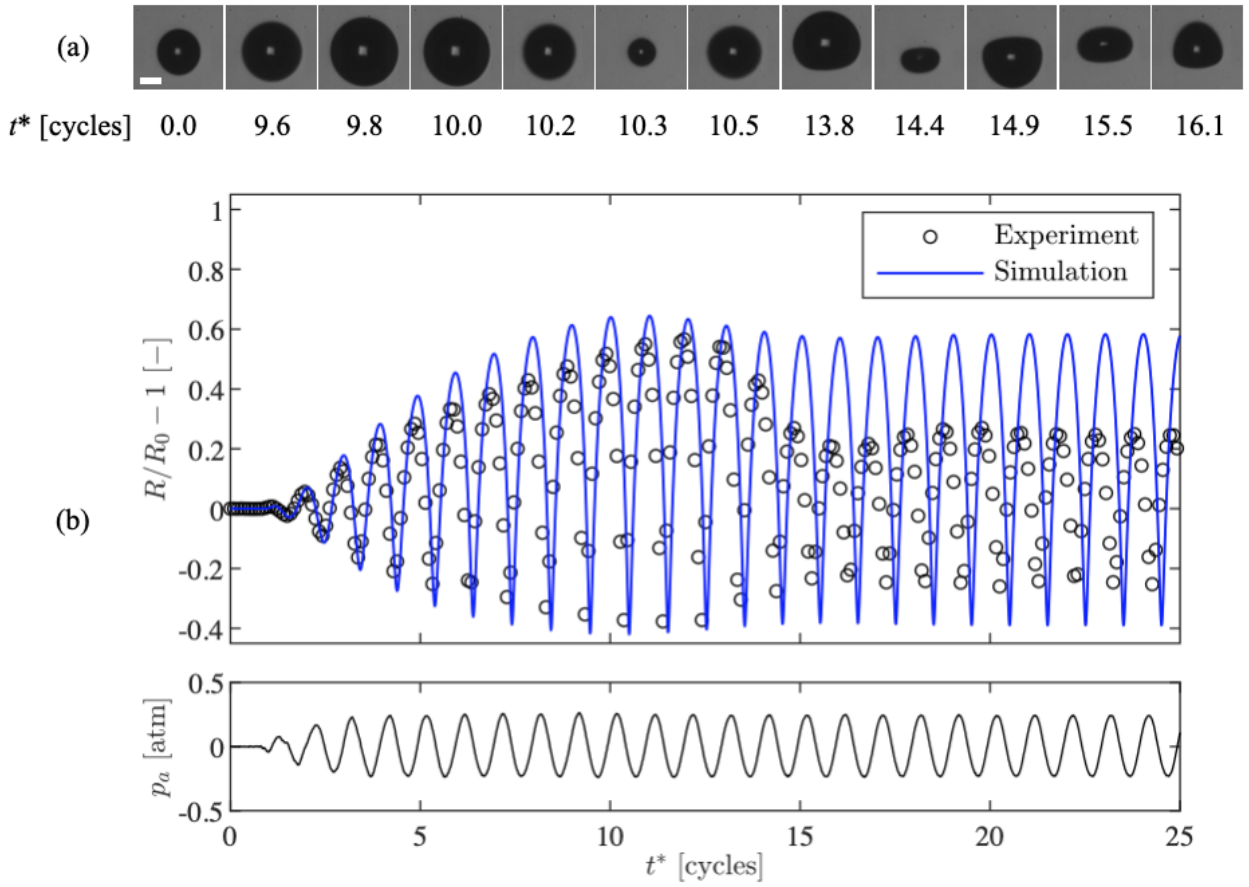

Figure 2.9: Non-spherical bubble oscillations of mode 1 in the 6 wt% gelatin gel driven by 28 kHz ultrasound ($R_0 = 107.8\ \mu$m, $f/f_R = 0.93$). (a) A series of the recorded images. The scale bar represents 100 μm. (b) Evolution of the area-equivalent radius compared with numerical solutions of the model with the viscosity $\mu = 18.3$ mPa $\cdot$ s and shear modulus $G = 4.0$ kPa fitted through the linear theory (top) and the ultrasound pressure wave with $p_A \approx 0.24$ atm (bottom).

the volumetric oscillation amplitude in the experiment[5] is damped after the non-spherical oscillations appear, because some of the energy is consumed by the non-spherical oscillations (Feng & Leal, 1997; Liu *et al.*, 2011). Obviously, the present model for spherical bubble dynamics cannot predict this non-spherical behavior and overestimates the volumetric oscillations. Departures from sphericity are quantified and predicted in chapter 5.

The resonance curve of the finite amplitude oscillations is constructed by repeating the same experiment as figures 2.8 and 2.9 but with increasing the bubble radius starting from $R_0 \approx 50\ \mu$m,

[5] After the non-spherical oscillations appear, the area-equivalent radius is no longer the spherical bubble radius $R(t)$ but still an estimate of oscillation amplitude in volume of the bubble.

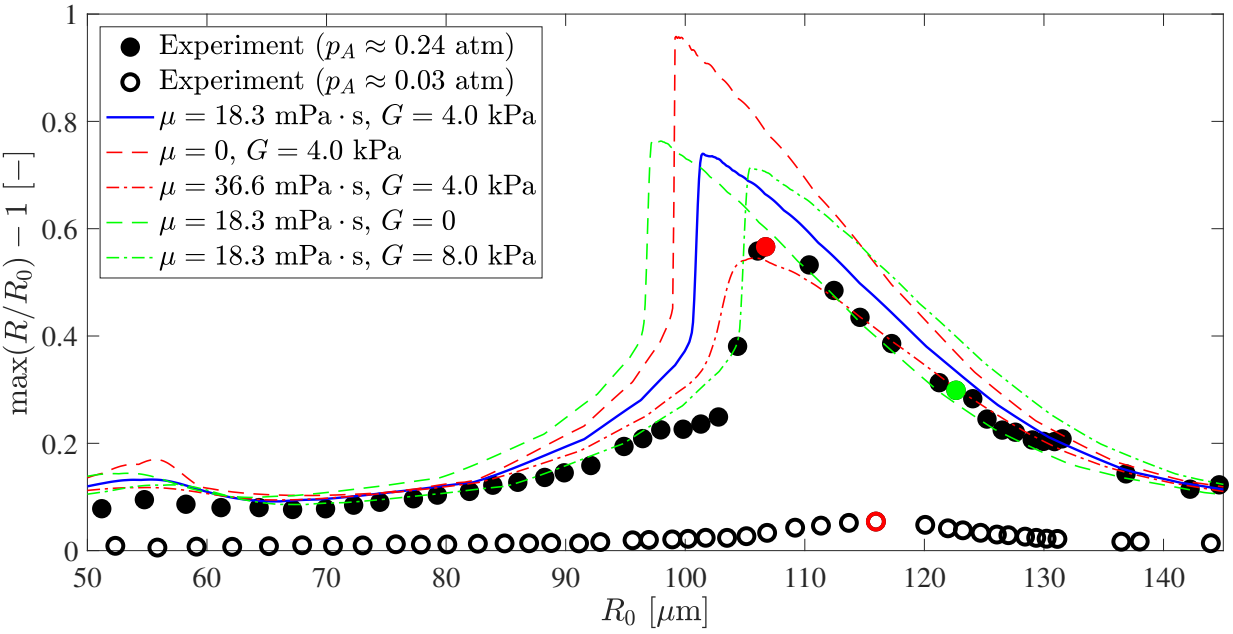

Figure 2.10: Resonance curve of the finite-amplitude bubble oscillations driven by 28 kHz ultrasound with $p_A \approx 0.24$ atm as a function of the bubble radius with pre-strain R_0. The filled circles represent the experimental results, in which the green and red ones correspond to the cases in figures 2.8 and 2.9, respectively. The resonance curve of the small-amplitude oscillations in figure 2.7 is also included. The lines are the resonance curves obtained from numerical solutions of the model with varying viscosity and shear modulus of the gel.

as shown in figure 2.10. The filled circles represent the experimental results including the cases in figures 2.8 and 2.9 as green and red ones, respectively. For comparison purposes, the resonance curve of the small-amplitude oscillations already shown in figure 2.7 is also included in figure 2.10. The resonance curve of the finite-amplitude oscillations shows nonlinear characteristics. Specifically, the resonant bubble radius becomes smaller as the peak (red filled circle) is shifted to the smaller bubble radius R_0 compared to the peak of the small-amplitude oscillations (red circle). The resonance curve also has a jump before the peak. These nonlinear features are known as *spring softening* and reported in the past numerical studies for bubbles in water (Lauterborn, 1976; Fujiwara & Shima, 1980). Bubbles oscillating in water have a tendency to break up (Brennen, 2002), while bubbles in gels are rather stable, thus allowing us to experimentally observe the nonlinear spherical oscillations and confirm the spring softening feature.

2.5.2 The role of viscoelasticity on bubble oscillations

We numerically examine the dependence of the resonance curve on the viscoelastic properties of the gel. Figure 2.10 shows the resonance curve obtained from the simulations with the viscosity $\mu = 18.3$ mPa $\cdot$ s and shear modulus $G = 4.0$ kPa fitted through the linear theory (solid blue line). In addition, the resonance curves obtained from the simulations with no viscosity $\mu = 0$ and double viscosity $\mu = 36.6$ mPa $\cdot$ s (but with the same shear modulus) are shown as red lines, and those with no shear modulus $G = 0$ and double shear modulus $G = 8.0$ kPa (but with the same viscosity) are shown as green lines. Viscosity suppresses the oscillation amplitude, thus reducing the spring softening feature and increasing the resonant bubble radius. Shear modulus increases the resonant bubble radius, while it has a small impact on the oscillation amplitude.

The discrepancy in the resonance curves between the experiments (filled circles) and simulations with the fitting parameters (solid blue line) in figure 2.10 is emphasized especially for the cases that the bubble radius R_0 is smaller than the resonant bubble radius. All the experimental data in figure 2.10 are obtained from the same sample of the bubble in the gelatin gel, and the order of the experimental runs is from the smallest to largest size of the bubble, with alternately using the high- and low-amplitude ultrasound pressure. Therefore, we speculate that the discrepancy is caused by the reduced viscosity and shear modulus of the gel which is damaged by the large-amplitude oscillations around the resonant condition. For example, the gel in figure 2.6 (red circle in figure 2.10) had already been damaged by the larger-amplitude oscillations in figure 2.9 (red filled circle in figure 2.10). This indicates that our fitting parameters determined through the linear theory correspond to the damaged gel. In fact, the simulations with higher viscoelasticity (chain lines in figure 2.10) yield better agreement with the experiments.

2.6 Conclusions

Ultrasound-induced nonlinear oscillations of a gas bubble in a 6 wt% air-supersaturated gelatin gel are experimentally and numerically studied to investigate the role of viscoelasticity on bubble

dynamics. The comparison of finite-amplitude oscillations between experiments and simulations shows good agreement, implying the validity of the Rayleigh–Plesset-type model for spherical bubble dynamics coupled with the Kelvin-Voigt constitutive equation with neo-Hookean elasticity. The resonance curve of the finite-amplitude bubble oscillations is experimentally obtained, which shows the nonlinear feature of spring softening. The appropriate selection of the viscosity and shear modulus of the gel is important to reproduce the experimentally determined resonance curve because the resonant radius and peak amplitude are sensitive to viscoelasticity. The comparison of the resonance curve between experiments and simulations indicates that our fitting parameters obtained through the linear theory correspond to the gel which has been damaged by the repeated large-amplitude oscillations.

These validation studies as well as findings of the role of viscoelasticity contribute to the fundamental understanding of ultrasound-induced bubble dynamics in soft matter. The experiments show that the bubble eventually starts non-spherical oscillations of mode 1, while the model for spherical bubble dynamics cannot predict this non-spherical behavior and overestimates the volumetric oscillations. This is a critical drawback when it comes to predicting the bubble break up or the bubble collapse pressure in the therapeutic ultrasound (Brennen, 2015). The shape instability of a bubble during ultrasound-induced oscillations is known as parametric instability (Versluis *et al.*, 2010), and is investigated in greater detail in chapters 4 and 5 of this thesis. In this chapter, we study the dynamics of an air-dominated bubble, while laser-induced cavitation bubbles in soft materials used in IMR have gas-vapor mixture inside the bubble. Therefore, we extend the model to consider the gas-vapor mixture transport in chapter 3.

CHAPTER 3

Inertial Collapse of a Spherical Gas-vapor Bubble in Soft Matter

3.1 Introduction

We study gas-vapor mixture transport inside a bubble, which plays an important role on inertial bubble collapse in soft matter. One of the goals of this thesis is to improve the model for spherical bubble dynamics used in Inertial Microcavitation high strain-rate Rheometry (IMR) (Estrada *et al.*, 2018). Contents of cavitation bubbles in water are usually vapor with a small amount of air, while a finite amount of non-condensible gas as well as vapor are expected to exist inside laser-induced cavitation bubbles in soft materials. However, studies for gas-vapor bubble dynamics are limited (Akhatov *et al.*, 2001; Hao *et al.*, 2017), and the role of gas-vapor mixture transport on the inertial collapse is not fully understood. From a modeling standpoint, past studies (Hao *et al.*, 2017; Estrada *et al.*, 2018) relied on the assumption that the ratios of specific heats are the same for the non-condensable gas and vapor $\gamma = \gamma_g = \gamma_v$ (we call this *constant-γ assumption*), which is a limitation of the current model. In this chapter, we develop a new model for gas-vapor bubble dynamics that accounts for variations in the ratio of specific heats of the mixture, and then investigate the role of gas-vapor mixture transport on inertial collapse.

Under the spherically symmetric, homobaric, cold liquid and weakly compressible assumptions, a model for homobaric bubble pressure is derived from the conservation laws for the gas-vapor mixture inside the bubble. In contrast with the bubble consisting of non-condensible gas

only in chapter 2, the present model includes gas-vapor mixture transport inside the bubble, as well as vaporization and condensation at the bubble interface. We first develop the new model and present the dimensionless form, numerical method and verification. Then, the role of gas-vapor mixture transport on inertial collapse is investigated by resolving the temperature and mass fraction fields inside the bubble. Furthermore, our analysis on the gas-vapor bubble dynamics is validated against experiments of laser-induced bubble collapse in 50 wt% glycerol. Lastly, we investigate the validity of the constant-γ assumption by comparing solutions between the new and conventional models. The experimental data in this chapter were provided by Ms. Selda Buyukozturk, Mr. Harry Cramer, and Prof. Christian Franck from the University of Wisconsin.

3.2 Modeling of spherical gas-vapor bubble dynamics

3.2.1 Gas-vapor mixture model

The model for homobaric bubble pressure $p_b(t)$ of gas-vapor mixture is derived from the conservation laws (2.1) to (2.3) for the mixture in conjunction with the equation of state (ideal gas law). The thermodynamic system corresponds to the local control volume as illustrated in figure 3.1. The non-condensible gas and vapor share the volume $V = V_g = V_v$, at equilibrium temperature $T = T_g = T_v$, where the subscripts g and v denote non-condensible gas and vapor, respectively. The pressure and density of the gas-vapor mixture follow Dalton's law: $p_m = p_g + p_v$ and $\rho_m = \rho_g + \rho_v$. The mass fraction of vapor is defined as $k = \rho_v/\rho_m$, and the mass fraction of gas is correspondingly $1 - k = \rho_g/\rho_m$. Then, mixture properties are given as follows (e.g., Thompson, 1972, pp. 82-85): mixture enthalpy $h_m = kh_v + (1-k)h_g$, mixture specific heat at constant pressure $C_{p,m} = kC_{p,v} + (1-k)C_{p,g}$ and mixture gas constant $\mathcal{R}_m = k\mathcal{R}_v + (1-k)\mathcal{R}_g$. The velocity field is also given based on the mass fraction $u_{i,m} = ku_{i,v} + (1-k)u_{i,g}$. Note that the total pressure is assumed to be uniform, while partial pressures of gas and vapor are not uniform: $p_m = p_b(t) = p_g(r,t) + p_v(r,t)$. Nevertheless, the mixture is assumed to follow the ideal gas law $p_b = \rho_m \mathcal{R}_m T$.

The conservation of mass (2.1) for a gas-vapor mixture combined with Fick's law for mass

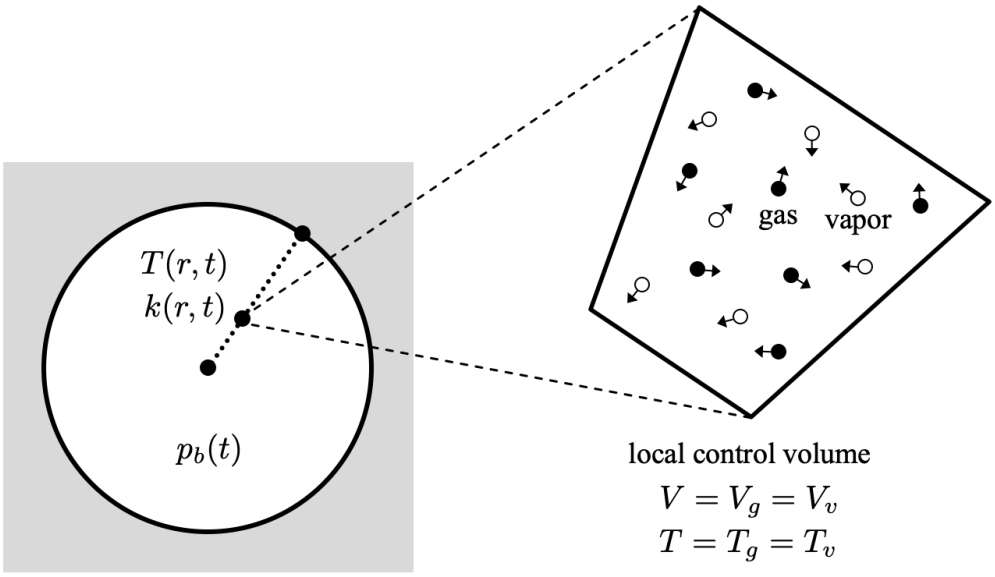

Figure 3.1: Local control volume in the field inside the bubble. Non-condensable gas and vapor share the volume at equilibrium temperature.

diffusion results in the following Partial Differential Equation (PDE) for mass fraction of vapor (Estrada *et al.*, 2018),

$$\frac{\partial k}{\partial t} + u_{r,m}\frac{\partial k}{\partial r} = \frac{1}{\rho_m r^2}\frac{\partial}{\partial r}\left(\rho_m r^2 D_m \frac{\partial k}{\partial r}\right), \tag{3.1}$$

where D_m is the mass diffusivity between the non-condensable gas and vapor.

Subtracting conservation of momentum (2.2) multiplied by $u_{j,m}$ from conservation of energy (2.3) results in

$$\rho_m\left(\frac{\partial h_m}{\partial t} + u_{i,m}\frac{\partial h_m}{\partial x_i}\right) - \dot{p}_b = \frac{\partial}{\partial x_i}\left(K_m \frac{\partial T}{\partial x_i}\right), \tag{3.2}$$

where the internal energy e_m is replaced by the enthalpy $h_m = e_m + p_b/\rho_m$, the heat flux is given by Fourier's law for heat diffusion, and $K_m(T,k)$ is the mixture thermal conductivity which depends on both temperature and mass fraction of vapor (see section 3.2.2). We neglect viscous stresses because their contributions to the bubble dynamics are small even if the temperature dependence of gas viscosity is taken into account (see Appendix B). Using the thermodynamic relation $h_m =$

$C_{p,m}T$, the mixture variables defined above, and the PDE for the mass fraction of vapor (3.1), equation (3.2) becomes

$$\rho_m C_{p,m}\left(\frac{\partial T}{\partial t}+u_{i,m}\frac{\partial T}{\partial x_i}\right)+(C_{p,v}-C_{p,g})T\frac{\partial}{\partial x_i}\left(\rho_m D_m\frac{\partial k}{\partial x_i}\right)-\dot{p}_b=\frac{\partial}{\partial x_i}\left(K_m\frac{\partial T}{\partial x_i}\right). \tag{3.3}$$

Using the ideal gas law, the first term on the left-hand side is rewritten as

$$\rho_m C_{p,m}\left(\frac{\partial T}{\partial t}+u_{i,m}\frac{\partial T}{\partial x_i}\right)=\frac{C_{p,m}}{\mathcal{R}_m}\left[\dot{p}_b-T(\mathcal{R}_v-\mathcal{R}_g)\frac{\partial}{\partial x_i}\left(\rho_m D_m\frac{\partial k}{\partial x_i}\right)+p_b\frac{\partial u_{i,m}}{\partial x_i}\right]. \tag{3.4}$$

Then, equation (3.3) can be organized as below, for the radial component in spherical coordinates,

$$\dot{p}_b-\frac{\mathcal{R}_m}{C_{p,m}}\dot{p}_b+p_b\frac{1}{r^2}\frac{\partial}{\partial r}(r^2u_{r,m})=\mathsf{G}, \tag{3.5}$$

where

$$\mathsf{G}=\left(\frac{\mathcal{R}_v-\mathcal{R}_g}{\mathcal{R}_m}-\frac{C_{p,v}-C_{p,g}}{C_{p,m}}\right)\mathcal{R}_m T\frac{1}{r^2}\frac{\partial}{\partial r}\left(r^2\rho_m D_m\frac{\partial k}{\partial r}\right)+\frac{\mathcal{R}_m}{C_{p,m}}\frac{1}{r^2}\frac{\partial}{\partial r}\left(r^2K_m\frac{\partial T}{\partial r}\right). \tag{3.6}$$

Integrating equation (3.5) from the bubble center $r=0$ to the bubble wall $r=R(t)$ leads to the Ordinary Differential Equation (ODE) for homobaric bubble pressure:

$$\dot{p}_b=\frac{-p_bR^2u_{r,m,w}+\int_0^R\mathsf{G}r^2dr}{\frac{1}{3}R^3-\int_0^R\frac{\mathcal{R}_m}{C_{p,m}}r^2dr}, \tag{3.7}$$

where the radial velocity at the bubble wall $u_{r,m,w}$ is given by Fick's law[1] and the fact that radial velocity of non-condensable gas at the bubble wall is $u_{r,g,w}=\dot{R}$ (Estrada *et al.*, 2018),

$$u_{r,m,w}=\dot{R}-\frac{1}{1-k_w}D_m\left.\frac{\partial k}{\partial r}\right|_w. \tag{3.8}$$

[1]The mass diffusion at the bubble wall is taken into account for the bubble pressure, while it is negligible in the Rayleigh–Plesset equation (Brennen, 1995, pp. 47-50).

Integrating equation (3.5) from the bubble center $r = 0$ to radial distance r leads to an expression for the radial velocity field ($0 \leq r \leq R$),

$$u_{r,m}(r,t) = \frac{1}{p_b r^2}\left[\int_0^r \mathsf{G} r^2 dr - \dot{p}_b\left(\frac{1}{3}r^3 - \int_0^r \frac{\mathcal{R}_m}{C_{p,m}} r^2 dr\right)\right]. \tag{3.9}$$

The radial component of equation (3.3) leads to the PDE for temperature:

$$\begin{aligned}\rho_m C_{p,m}\left(\frac{\partial T}{\partial t} + u_{r,m}\frac{\partial T}{\partial r}\right) &= \dot{p}_b + \frac{1}{r^2}\frac{\partial}{\partial r}\left(r^2 K_m \frac{\partial T}{\partial r}\right) \\ &\quad - (C_{p,v} - C_{p,g})T\frac{1}{r^2}\frac{\partial}{\partial r}\left(r^2 \rho_m D_m \frac{\partial k}{\partial r}\right).\end{aligned} \tag{3.10}$$

3.2.2 Mixture thermal conductivity

Although there exists a kinetic theory for temperature-dependent thermal conductivity (Sutherland's law) and mixture thermal conductivity (Wilke's semi-empirical formula) (White, 2006, pp. 28-31, 34), a linear approximation enables us to avoid numerical errors. We extend the temperature-dependent thermal conductivity of Prosperetti *et al.* (1988) as

$$K_m(T,k) = A(k)T + B(k), \tag{3.11}$$

where the coefficients are given by $A(k) = kA_v + (1-k)A_g$ and $B(k) = kB_v + (1-k)B_g$. We use a different variable for temperature:

$$\tau = \int_{T_\infty}^{T} K(\hat{T},k)d\hat{T}, \tag{3.12}$$

which expands the mixture thermal conductivity from the spatial derivatives,

$$\frac{1}{r^2}\frac{\partial}{\partial r}\left(r^2 K_m \frac{\partial T}{\partial r}\right) = \frac{1}{r^2}\frac{\partial}{\partial r}\left(r^2 K_m \frac{\partial T}{\partial \tau}\frac{\partial \tau}{\partial r}\right) = \frac{1}{r^2}\frac{\partial}{\partial r}\left(r^2 \frac{\partial \tau}{\partial r}\right). \tag{3.13}$$

Property	Value
γ	1.33
M	18.02 g/mol
C_p	1.86 kJ/(kg · K)
A	9.7×10^{-5} W/m · K^2
B	-1.21×10^{-2} W/m · K

Table 3.1: Physical properties of vapor.

Property	Value
γ	1.67
M	39.94 g/mol
C_p	0.52 kJ/(kg · K)
A	3.0×10^{-5} W/m · K^2
B	1.09×10^{-2} W/m · K

Table 3.2: Physical properties of argon.

This approach enables us to avoid errors associated with finite differences, which is crucial because the temperature gradients near the bubble wall are often very large and thus give rise to significant numerical errors. The linear approximation (3.11) enables us to obtain a simple $\tau - T$ relation from equation (3.12):

$$T = \frac{\sqrt{K^2(T_\infty, k) + 2A(k)\tau} - B(k)}{A(k)}. \tag{3.14}$$

The coefficients A and B for each gas are obtained by fitting to Sutherland's law,

$$K(T) = K_0 \left(\frac{T}{T_0}\right)^{\frac{3}{2}} \frac{T_0 + \mathcal{S}_t}{T + \mathcal{S}_t}, \tag{3.15}$$

where K_0, T_0 and $\mathcal{S}_t$ are the Sutherland's law parameters which are available in White (2006, p. 31). Figure 3.2 shows the fitting results, where the coefficients for air are from Prosperetti *et al.* (1988), while the coefficients for vapor and argon are determined by the least squares method in the ranges of 300 $K \leq T \leq$ 900 K and 150 $K \leq T \leq$ 1800 K as these ranges are for ±2% error, respectively (White, 2006, p. 31). Physical properties of air, vapor and argon are listed in tables 2.1, 3.1 and 3.2.

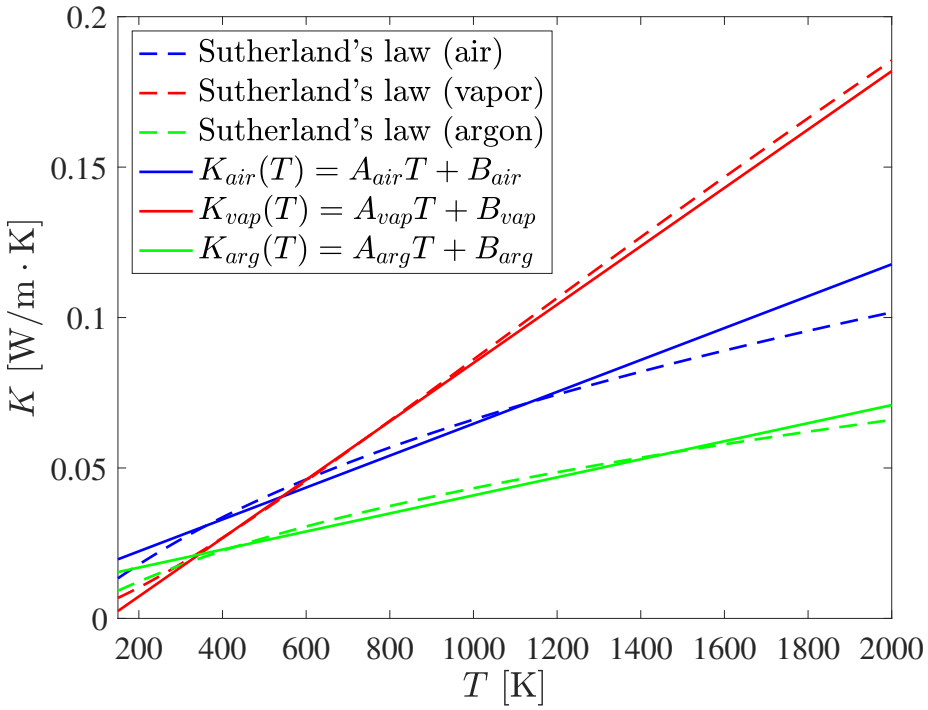

Figure 3.2: Temperature-dependent thermal conductivities of air, vapor and argon given by Sutherland's law and linear approximations. The fitting coefficients are listed in tables 2.1, 3.1 and 3.2 for air, vapor and argon, respectively.

3.2.3 Summary of the variable-γ gas-vapor mixture model

In summary, the dynamics of a spherical gas-vapor bubble in soft matter are described by solving the two ODEs and two PDEs simultaneously: the Keller–Miksis equation (2.5), the ODE for homobaric bubble pressure (3.7), the PDE for temperature (3.10) and the PDE for mass fraction of vapor (3.1), where the radial velocity is given by equation (3.9). The novelty of our gas-vapor mixture model is that we overcome the constant-γ assumption $\gamma = \gamma_g = \gamma_v$ used in past studies (Hao *et al.*, 2017; Estrada *et al.*, 2018). Instead, our model requires the evaluation of integrals for the fields of mixture gas constant $\mathcal{R}_m(r,t)$ and specific heat at constant pressure $C_{p,m}(r,t)$ inside the bubble.

The boundary conditions for the two PDEs are given as follows: we have the symmetry boundary condition at the origin,

$$\left.\frac{\partial T}{\partial r}\right|_{r=0} = 0, \quad \left.\frac{\partial k}{\partial r}\right|_{r=0} = 0, \tag{3.16}$$

the cold liquid assumption $T(r = R, t) = T_\infty$, and the partial pressure of vapor at the bubble wall for equilibrium phase change $p_{v,w} = p_{v,sat}(T_\infty)$, which gives $k(r = R, t) = k_w$ where k_w is determined by the relation between mass fraction of vapor and the pressure ratio,

$$k = \frac{1}{1 + \dfrac{\mathcal{R}_v}{\mathcal{R}_g}\left(\dfrac{p_b}{p_v} - 1\right)}, \tag{3.17}$$

which stems from the ideal gas law and the definition of mixture properties. The temperature-dependent saturated vapor pressure approximating tabulated data gives $p_{v,sat}(T_\infty) = 3.1$ kPa in water at the cold liquid temperature (Nigmatulin *et al.*, 1981), which is used as the boundary condition in this study. However, saturated vapor pressure at the gel interface is expected to be smaller for higher gel concentration, though data are not available. We investigate the dependence of the solution on this boundary condition in section 3.6.

The mass diffusivity follows an empirical relation (Fuller's correlation) (Cussler, 2009, p. 123).

At Standard Temperature and Pressure (STP) ($T_\infty = 298.15$ K and $p_{atm} = 101.3$ kPa), $D_m = 0.252 \times 10^{-4}$ m^2/s for air and vapor, and $D_m = 0.257 \times 10^{-4}$ m^2/s for argon and vapor.

The integrand (3.6) and the PDE for temperature (3.10) have similarities to the model of Nigmatulin *et al.* (1981), which is also used in the study of Akhatov *et al.* (2001), but have key differences. We consider conservation laws for the gas-vapor mixture, while Nigmatulin *et al.* (1981) considered conservation laws for gas and vapor separately and combined. The latter approach requires treatment of the individual heat flux terms, while we simply obtain a single heat flux term with the mixture thermal conductivity $K_m(T, k)$. As a result, our model is less complicated and appropriately describes the heat conduction in the gas-vapor mixture.

3.2.4 Constant-γ model

Under the constant-γ assumption $\gamma = \gamma_g = \gamma_v$ (which typically implies $\mathcal{R} = \mathcal{R}_g = \mathcal{R}_v$ and $C_p = C_{p,g} = C_{p,v}$), our gas-vapor model reduces to the conventional constant-γ model (Estrada *et al.*, 2018)[2]:

- ODE for homobaric bubble pressure

$$\dot{p}_b = \frac{3}{R}\left[-\gamma p_b u_{r,m,w} + (\gamma - 1)K_m \left.\frac{\partial T}{\partial r}\right|_w\right], \tag{3.18}$$

- PDE for temperature

$$\rho_m C_p \left(\frac{\partial T}{\partial t} + u_r \frac{\partial T}{\partial r}\right) = \dot{p}_b + \frac{1}{r^2}\frac{\partial}{\partial r}\left(r^2 K_m \frac{\partial T}{\partial r}\right), \tag{3.19}$$

- PDE for mass fraction of vapor

$$\frac{\partial k}{\partial t} + u_r \frac{\partial k}{\partial r} = \frac{1}{\rho_m r^2}\frac{\partial}{\partial r}\left(r^2 \rho_m D_m \frac{\partial k}{\partial r}\right), \tag{3.20}$$

[2]Strictly speaking, the past model of Estrada *et al.* (2018) is slightly different from the constant-γ model. That model requires $\gamma/(\gamma - 1)$ to be the same between gas and vapor, which is of course satisfied in the constant-γ case.

- The radial velocity field ($0 \leq r \leq R$)

$$u_r(r,t) = \frac{1}{\gamma p_b}\left[-\frac{1}{3}r\dot{p}_b + (\gamma-1)K_m\frac{\partial T}{\partial r}\right]. \tag{3.21}$$

Without vapor (i.e., $k(r,t) = 0$), the constant-γ model (3.18) to (3.21) further reduces to the pure gas model of Prosperetti *et al.* (1988) described in chapter 2. Solutions of our gas-vapor model are directly compared with those of the constant-γ model to examine the validity of the constant-γ assumption in section 3.7.

3.2.5 Dimensionless form

The equations are solved in dimensionless form. Given the characteristic length L_c and time T_c, and the normalized radial coordinate $y = r/R(t)$, the dimensionless forms of the gas-vapor mixture model for homobaric bubble pressure as well as the Keller–Miksis equation (2.5) are obtained as follows:

- Keller–Miksis equation

$$R^*\ddot{R}^*\left(1-\frac{\dot{R}^*}{c^*_\infty}\right) + \frac{3}{2}\dot{R}^{*2}\left(1-\frac{\dot{R}^*}{3c^*_\infty}\right) = \left(1+\frac{\dot{R}^*}{c^*_\infty}+\frac{R^*}{c^*_\infty}\frac{d}{dt^*}\right)\left(p^*_b - p^*_\infty - \frac{2}{\mathrm{We}R^*} + S^*\right), \tag{3.22}$$

- The stress integral

$$S^* = -\frac{4\dot{R}^*}{\mathrm{Re}R^*} - \frac{1}{2\mathrm{Ca}}\left[5 - 4\frac{R_{eq}}{L_cR^*} - \left(\frac{R_{eq}}{L_cR^*}\right)^4\right], \tag{3.23}$$

- ODE for homobaric bubble pressure

$$\dot{p}^*_b = \frac{-p^*_b u^*_{r,m,w} + R^*\int_0^1 \frac{\mathcal{R}_m}{C_{p,m}}\frac{\rho_m}{\rho_\infty}\frac{1}{\mathrm{Ec}}\mathsf{G}^* y^2 dy}{\frac{1}{3}R^* - R^*\int_0^1 \frac{\mathcal{R}_m}{C_{p,m}} y^2 dy}, \tag{3.24}$$

- The radial velocity at the bubble wall

$$u^*_{r,m,w} = \dot{R}^* - \frac{1}{1-k_w}\frac{\mathrm{Fo}_m}{R^*}\left.\frac{\partial k}{\partial y}\right|_w, \tag{3.25}$$

- The integrand

$$\mathsf{G}^* = \left(\frac{\mathcal{R}_v - \mathcal{R}_g}{\mathcal{R}_m} - \frac{C_{p,v} - C_{p,g}}{C_{p,m}}\right) T^* \frac{\mathrm{Fo}_m}{R^{*2}} \frac{1}{\rho_m y^2}\frac{\partial}{\partial y}\left(\rho_m y^2 \frac{\partial k}{\partial y}\right) + \frac{\mathrm{Fo}_h}{R^{*2}}\frac{1}{y^2}\frac{\partial}{\partial y}\left(y^2\frac{\partial \tau^*}{\partial y}\right), \tag{3.26}$$

- PDE for temperature

$$\begin{aligned}\frac{\partial \tau^*}{\partial t^*} + \frac{u^*_r - \dot{R}^* y}{R^*}\frac{\partial \tau^*}{\partial y} &= \frac{\rho_\infty}{\rho_m}\mathrm{Ec} K^* \dot{p}^*_b + K^* \frac{\mathrm{Fo}_h}{R^{*2}}\frac{1}{y^2}\frac{\partial}{\partial y}\left(y^2\frac{\partial \tau^*}{\partial y}\right) \\ &\quad - \frac{C_{p,v} - C_{p,g}}{C_{p,m}} T^* K^* \frac{\mathrm{Fo}_m}{R^{*2}}\frac{1}{\rho_m y^2}\frac{\partial}{\partial y}\left(\rho_m y^2 \frac{\partial k}{\partial y}\right),\end{aligned} \tag{3.27}$$

- PDE for mass fraction of vapor

$$\frac{\partial k}{\partial t^*} + \frac{u^*_r - \dot{R}^* y}{R^*}\frac{\partial k}{\partial y} = \frac{\mathrm{Fo}_m}{R^{*2}}\frac{1}{\rho_m y^2}\frac{\partial}{\partial y}\left(\rho_m y^2 \frac{\partial k}{\partial y}\right), \tag{3.28}$$

- The radial velocity field ($0 \le y \le 1$)

$$u^*_r(y, t^*) = \frac{R^*}{p^*_b y^2}\left[\int_0^y \frac{\mathcal{R}_m}{C_{p,m}}\frac{\rho_m}{\rho_\infty}\frac{1}{\mathrm{Ec}}\mathsf{G}^* y^2 dy - \dot{p}^*_b\left(\frac{1}{3}y^3 - \int_0^y \frac{\mathcal{R}_m}{C_{p,m}} y^2 dy\right)\right], \tag{3.29}$$

where the asterisk denotes dimensionless quantities[3], and the obtained dimensionless numbers are listed in table 3.3. We choose the characteristic length and time as $L_c = R_{eq}$ and $T_c = 1/f_d$ for ultrasound-induced bubble oscillations, while $L_c = R_{max}$ and $T_c = R_{max}\sqrt{\rho_\infty / p_{atm}}$ (Rayleigh collapse time) for laser-induced bubble collapse. Dimensionless forms of the constant-γ model and the pure gas model are available in Appendix A.

[3]The temperature and thermal conductivity are non-dimensionalized as $T^* = T/T_\infty$, $K^* = K/K(T_\infty, k_\infty)$ and $\tau^* = \tau/K(T_\infty, k_\infty)T_\infty$, where k_∞ is given by the equation (3.17) with $p_b = p_{atm} + 2\sigma/R_{eq}$ and $p_{v,sat}(T_\infty)$.

Name	Definition
Weber number	$\mathrm{We} = \rho_\infty V_c^2 L_c/\sigma$
Reynolds number	$\mathrm{Re} = \rho_\infty V_c L_c/\mu$
Cauchy number	$\mathrm{Ca} = \rho_\infty V_c^2/G$
Mass Fourier number	$\mathrm{Fo}_m = D_m/V_c L_c$
Heat Fourier number	$\mathrm{Fo}_m = D_h/V_c L_c$
Eckert number	$\mathrm{Ec} = V_c^2/C_{p,m} T_\infty$

Table 3.3: Dimensionless numbers in the model for spherical bubble dynamics in soft matter. $V_c = L_c/T_c$ is the characteristic velocity and $D_h = K(T_\infty, k)/\rho_m C_{p,m}$ is the thermal diffusivity.

As we expand the mixture thermal conductivity from the spatial derivatives in equation (3.13), it is preferable to avoid finite difference approximations on the mixture density field $\rho_m(r,t)$ as well. Thus, the diffusion term in the mass fraction of vapor in equations (3.26), (3.27) and (3.28) is computed as the following form

$$\frac{1}{\rho_m y^2}\frac{\partial}{\partial y}\left(\rho_m y^2 \frac{\partial k}{\partial y}\right) = \left(-\frac{\mathcal{R}_v - \mathcal{R}_g}{\mathcal{R}_m}\frac{\partial k}{\partial y} - \frac{1}{T^* K^*}\frac{\partial \tau^*}{\partial y}\right)\frac{\partial k}{\partial y} + \frac{1}{y^2}\frac{\partial}{\partial y}\left(y^2 \frac{\partial k}{\partial y}\right), \tag{3.30}$$

where the ideal gas law is used.

3.2.6 Numerical method

We discretize the radial coordinate inside the bubble with uniform grid spacing Δy as shown in figure 3.3. The computational domain ranges $0 \le y_i \le 1$ where $i = 0, ..., N_y$, on which we have discrete fields of temperature τ_i^* and mass fraction of vapor k_i. The spatial derivatives in the PDEs (3.27) and (3.28) are discretized with second-order central differences, e.g., for temperature,

$$\left.\frac{d\tau^*}{dy}\right|_i \approx \frac{\tau_{i+1}^* - \tau_{i-1}^*}{2\Delta y}, \quad \left.\frac{d^2\tau^*}{dy^2}\right|_i \approx \frac{\tau_{i+1}^* - 2\tau_i^* + \tau_{i-1}^*}{\Delta y^2}. \tag{3.31}$$

The values at the bubble center τ_c^* and k_c and the bubble wall τ_w^* and k_w are given by the boundary conditions. Second-order one-sided finite differences are applied at the origin (3.16):

$$\tau_c^* \approx \frac{4\tau_1^* - \tau_2^*}{3}, \quad k_c \approx \frac{4k_1 - k_2}{3}. \tag{3.32}$$

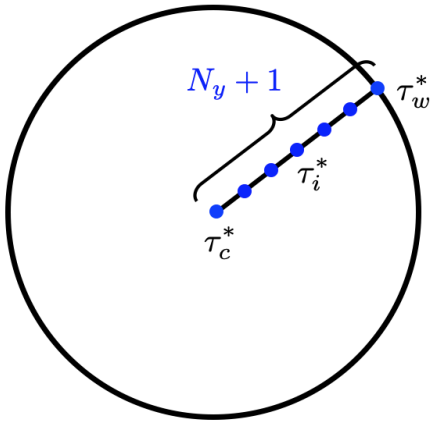

Figure 3.3: Numerical grids on the radial coordinate inside the bubble.

At the bubble wall, the cold liquid assumption yields $\tau_w^* = 0$ and k_w follows equation (3.17) for the saturated vapor pressure. The ODE for homobaric bubble pressure (3.24) requires spatial derivatives at the bubble wall, which are also discretized using second-order one-sided finite differences, e.g., for temperature,

$$\left.\frac{d\tau^*}{dy}\right|_w \approx \frac{\tau^*_{N_y-2} - 4\tau^*_{N_y-1} + 3\tau^*_w}{2\Delta y}, \quad \left.\frac{d^2\tau^*}{dy^2}\right|_w \approx \frac{-\tau^*_{N_y-3} + 4\tau^*_{N_y-2} - 5\tau^*_{N_y-1} + 2\tau^*_w}{\Delta y^2}. \tag{3.33}$$

To evaluate the integrals in equations (3.24) and (3.29), we use the second-order trapezoidal rule:

$$\int_0^1 f(y)dy \approx \Delta y\left(\frac{1}{2}f_c + \frac{1}{2}f_w + \sum_{j=1}^{N_y-1} f_j\right), \quad \int_0^y f(y)dy \approx \Delta y\left(\frac{1}{2}f_c + \frac{1}{2}f_i + \sum_{j=1}^{i-1} f_j\right), \tag{3.34}$$

where f is the integrand.

The ODEs and semi-discretized PDEs are summarized as the following system of equations:

$$\frac{d\boldsymbol{\xi}}{dt} = \mathcal{F}(\boldsymbol{\xi}), \quad \boldsymbol{\xi} = (R^*, \dot{R}^*, p_b^*, \tau_i^*, k_i^*)^T, \quad i = 1, ..., N_y - 1, \tag{3.35}$$

where the size of the column vector $\boldsymbol{\xi}$ is $3 + 2(N_y - 1)$, and the right-hand side $\mathcal{F}(\boldsymbol{\xi})$ consists of the two ODEs and two semi-discretized PDEs. This system of equations (3.35) is integrated in time

by the fifth-order Cash–Karp Runge–Kutta method (Press *et al.*, 2007, pp. 910-915)[4], in which we set the tolerance to 10^{-6} and the largest time step $\max(\Delta t)$ to satisfy the Courant-Friedrichs-Lewy (CFL) condition. Overall, the order of accuracy of our numerical method is second-order. The computational cost of our gas-vapor model is $O(N_t N_y \log(N_y))$, while that of the constant-γ model is $O(N_t N_y)$, where N_t is the number of time step.

3.3 Initial conditions for laser-induced bubble collapse

Initial conditions for the problem of laser-induced bubble collapse are set to when the bubble reaches the maximum radius R_{max} after the growth induced by focusing a laser pulse into soft materials. The process of laser-induced bubble collapse in soft materials is illustrated in figure 1.1 in chapter 1, in which the state (b) corresponds to the initial conditions. After the bubble collapses inertially, the bubble oscillates toward the equilibrium state (c) with the radius[5] R_{eq}. The initial bubble pressure is estimated by considering the relation between the initial and equilibrium states. All fields are uniform at the equilibrium state (c): temperature $T(r, t \to \infty) = T_\infty$, partial pressure of vapor $p_v(r, t \to \infty) = p_{v,sat}(T_\infty)$, and partial pressure of gas $p_g(r, t \to \infty) = p_{atm} + 2\sigma/R_{eq} - p_{v,sat}(T_\infty)$. The initial temperature and partial pressure fields at the state (b) are uncertainties in this problem, which are challenging to measure in experiments. We assume that the temperature is uniform and equal to the cold liquid temperature $T(r, t = 0) = T_\infty$ and the partial pressure of vapor is also uniform and equal to the saturated vapor pressure $p_v(r, t = 0) = p_{v,sat}(T_\infty)$. The dependence of the solution on this initial partial pressure of vapor is investigated in section 3.6. Considering the whole bubble as a thermodynamic system, the ideal gas law $p_g 4\pi R^3/3 = n_g \mathcal{R}_u T_\infty$ gives $p_g(r, t = 0)/p_g(r, t \to \infty) = (R_{eq}/R_{max})^3$ provided that the number of mole n_g is constant,

[4]The idea of the Cash–Karp Runge–Kutta method is to prepare two numerical solutions from different schemes: $x_{num,1} = x_{exact} + O(\Delta t^5)$ and $x_{num,2} = x_{exact} + O(\Delta t^4)$, and take difference between them to estimate the local truncation error $\varepsilon = |x_{num,1} - x_{num,2}| = O(\Delta t^4)$. The time step is adaptively reduced to confirm this error to be smaller than the tolerance $\varepsilon < 10^{-6}$.

[5]Pre-strain (see figure 2.4 in chapter 2) may exist in practice, which might not be negligible for stiffer gels (Ando & Shirota, 2019). However, the structural damage is problem-dependent (laser energy, type of hydrogels) and cannot be observed until the bubble completely dissolves into the gel. For simplicity, we do not consider the pre-strain in the rest of this thesis.

which leads to the following estimate of the initial bubble pressure (Estrada *et al.*, 2018),

$$p_b(t=0) = p_{v,sat}(T_\infty) + \left(p_{atm} + \frac{2\sigma}{R_{eq}} - p_{v,sat}(T_\infty)\right)\left(\frac{R_{eq}}{R_{max}}\right)^3. \tag{3.36}$$

The initially prescribed R_{eq} coincides with the solution $R(t \to \infty)$ for the pure gas model, while it does not coincide for the gas-vapor model and the constant-γ model because the partial pressure of gas is implicitly determined by $p_g(r,t) = p_b(t) - p_v(r,t)$. As a consequence, n_g does not remain constant, though the deviation is small at least in our problems. Other initial conditions are $R(t = 0) = R_{max}$ and $\dot{R}(t = 0) = 0$. For the laser-induced bubble collapse, the far-field pressure is constant of atmospheric pressure $p_\infty(t) = p_{atm}$.

3.4 Verification

Our numerical method is verified by a convergence study using the problem of laser-induced bubble collapse. We simulate the laser-induced collapse of an air-vapor bubble in a soft polyacrylamide gel according to the experiments of Estrada *et al.* (2018) for which physical properties are listed in table 3.4. Numerical solutions with different numbers of mesh points $N_y + 1$ for the bubble with $R_{max} = 100\,\mu$m and $R_{eq} = 50\,\mu$m are shown in figure 3.4 (a). An enlarged view in figure 3.4 (b) shows discrepancies between solutions with different N_y, which stems from numerical errors accumulated over each oscillation. Convergence is evaluated in figure 3.5, where the error is defined as $|R(t = 300\,\mu\text{s}) - R_{exact}|/R_{max}$ where R_{exact} is the numerical solution with $N_y = 1280$. Second-order accuracy is achieved as expected, thus verifying our numerical method. The same convergence study is conducted for the constant-γ model and the pure gas model[6]; second-order accuracy is obtained as well.

The number of mesh points $N_y + 1$ required for a sufficiently converged solution is problem-dependent. We need a finer spatial mesh for the problem of stronger collapse of a bubble to accurately capture the large gradients near the bubble wall (see figure 3.7). The violence of the

[6]For the pure gas model, $R_{exact} = R_{eq}$.

Property	Value
ρ_∞	1060 kg/m^3
c_∞	1430 m/s
σ	0.056 N/m
μ	56.0 mPa · s
G	3.16 kPa

Table 3.4: Physical properties of a soft polyacrylamide gel.

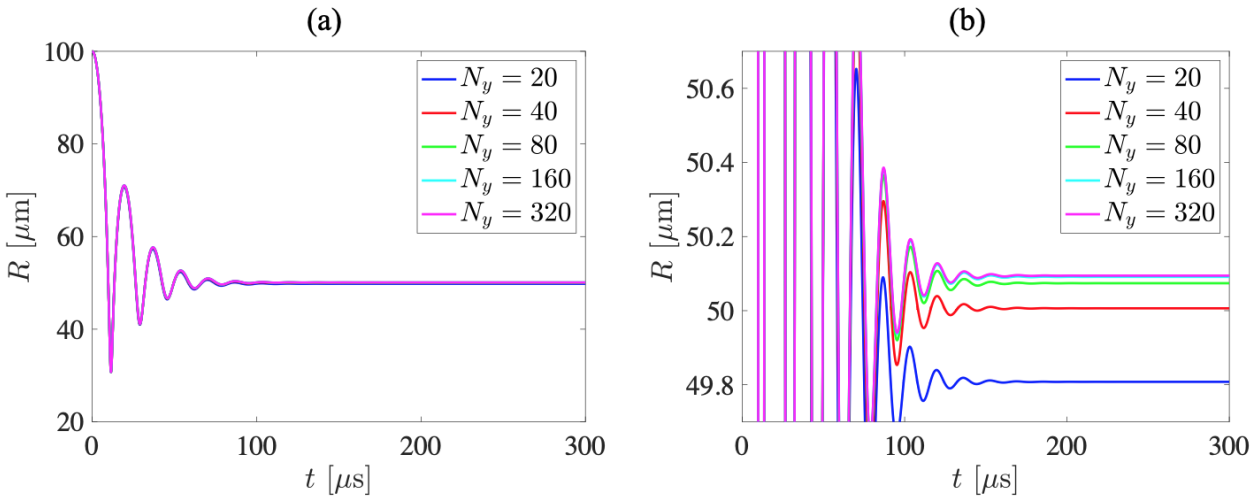

Figure 3.4: Numerical solutions for the laser-induced collapse of an air-vapor bubble with different number of mesh points $N_y + 1$. (a) The expanded bubble $R_{max} = 100\,\mu$m collapses and oscillates toward the equilibrium state $R_{eq} \approx 50\,\mu$m. (b) An enlarged figure of (a). Numerical solutions converge to the solution with the finest mesh.

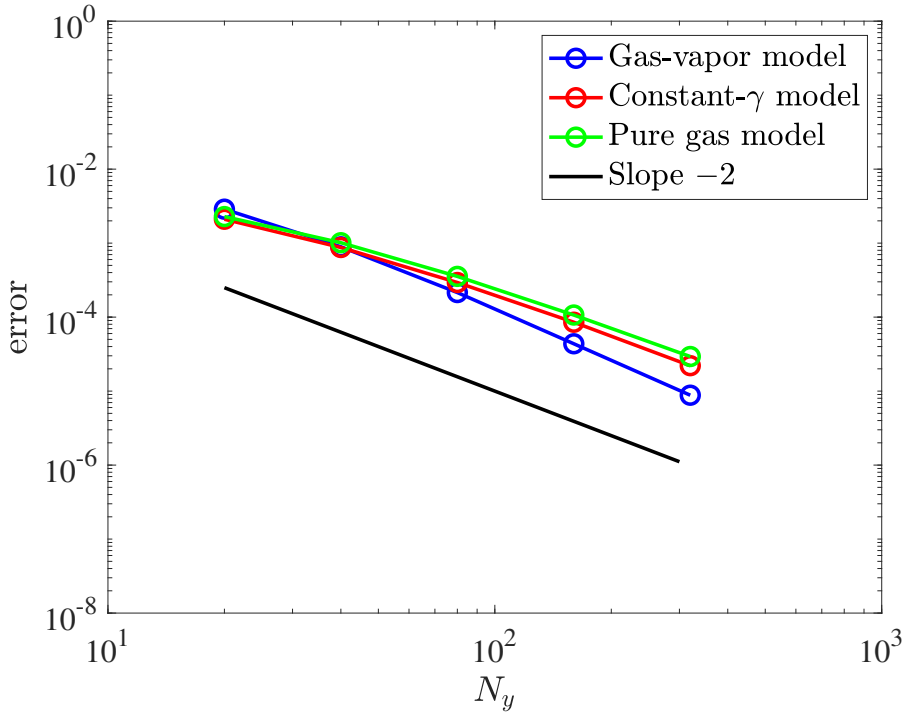

Figure 3.5: Convergence study showing the second-order accuracy of our numerical method. The error is defined as $|R(t = 300\ \mu\text{s}) - R_{exact}|/R_{max}$.

bubble collapse can be measured by the stretch ratio R_{max}/R_{eq}. For example, the laser-induced collapse of an air-vapor bubble in a soft polyacrylamide gel for $R_{max}/R_{eq} = 7$ (the case in figures 3.6 and 3.12) requires $N_y = 500$ to reduce the numerical error to less than 0.3% (dimensionally less than 1 μm) for the gas-vapor model, while $N_y = 200$ is sufficient for the constant-γ model and the pure gas model. Thus, we use $N_y = 500$ for the gas-vapor model and $N_y = 200$ for the other models in this thesis, with $\max(\Delta t) = 0.00001$ for the gas-vapor model and $\max(\Delta t) = 0.001$ for the other models to satisfy the CFL condition[7].

[7]We need smaller time step $\max(\Delta t)$ not only for finer mesh points $N_y + 1$ but also for larger stretch ratio R_{max}/R_{eq} because the advection speed u_{adv} in the PDEs is larger for the strong collapse; the CFL condition requires $u_{adv} \max(\Delta t)/\Delta y < 1$. The computational cost of the gas-vapor model is $O(N_t N_y \log(N_y))$, which is much larger than that of the other models $O(N_t N_y)$. Therefore, implicit methods may be more favorable than the explicit Cash–Karp Runge–Kutta method.

3.5 The role of gas-vapor mixture transport on inertial collapse

We investigate the role of gas-vapor mixture transport inside the bubble during laser-induced inertial collapse of a bubble in soft matter. Two different solutions are compared in figure 3.6 (a): one is for an air-vapor bubble obtained from the gas-vapor model (blue line), and the other is for an air bubble obtained from the pure gas model (red line). Both bubbles are in a soft polyacrylamide gel (table 3.4), and the initial conditions are set with $R_{max} = 350\,\mu$m and $R_{eq} = 50\,\mu$m. The initially expanded bubble collapses to its minimum radius R_{min}, where the inside gas is compressed rapidly $p_b \gg p_{atm}$, thus rebounding to the second maximum radius. We observe two major differences between the two solutions. First, the air-vapor bubble collapses to a minimum radius $R_{min} = 11.6\,\mu$m, which is larger than that of the pure air bubble ($R_{min} = 5.9\,\mu$m). Secondly, the air-vapor bubble rebounds to a larger size than that of the pure air bubble.

To understand the differences between the air-vapor and pure air bubbles, we examine the temperature and mass fraction fields during the inertial collapse of the air-vapor bubble in soft matter. Figure 3.7 shows sequential snapshots of the two fields $T(r,t)$ and $k(r,t)$ inside the bubble at $t = 0, 32.2, 33.0, 33.5, 50.6, 300.0\,\mu$s corresponding to the blue circles in figure 3.6 (a). The bubble initially contains 87% of vapor, which condenses to the surroundings during the collapse ($t = 32.2\,\mu$s). However, the collapse is so rapid compared to mass diffusion within the bubble that the vapor near the bubble center cannot diffuse toward the bubble interface and condense. As a result, an *air shell* is formed near the bubble wall (Akhatov *et al.*, 2001). It follows that, when the bubble reaches its minimum radius R_{min} ($t = 33.0\,\mu$s), the maximum temperature is induced near the bubble wall in the air-dominated region rather than at the bubble center in the vapor-dominated region. A large amount of vapor still remains inside the bubble right after the collapse ($t = 33.5\,\mu$s). This trapped vapor makes the minimum radius of the air-vapor bubble larger than that of the pure air bubble in figure 3.6 (a). During the rebound ($t = 50.6\,\mu$s), water from the surroundings vaporizes into the bubble. In the end, the bubble is in equilibrium, with $T(r,t) = T_\infty$ and $p_v(r,t) = p_{v,sat}(T_\infty)$.

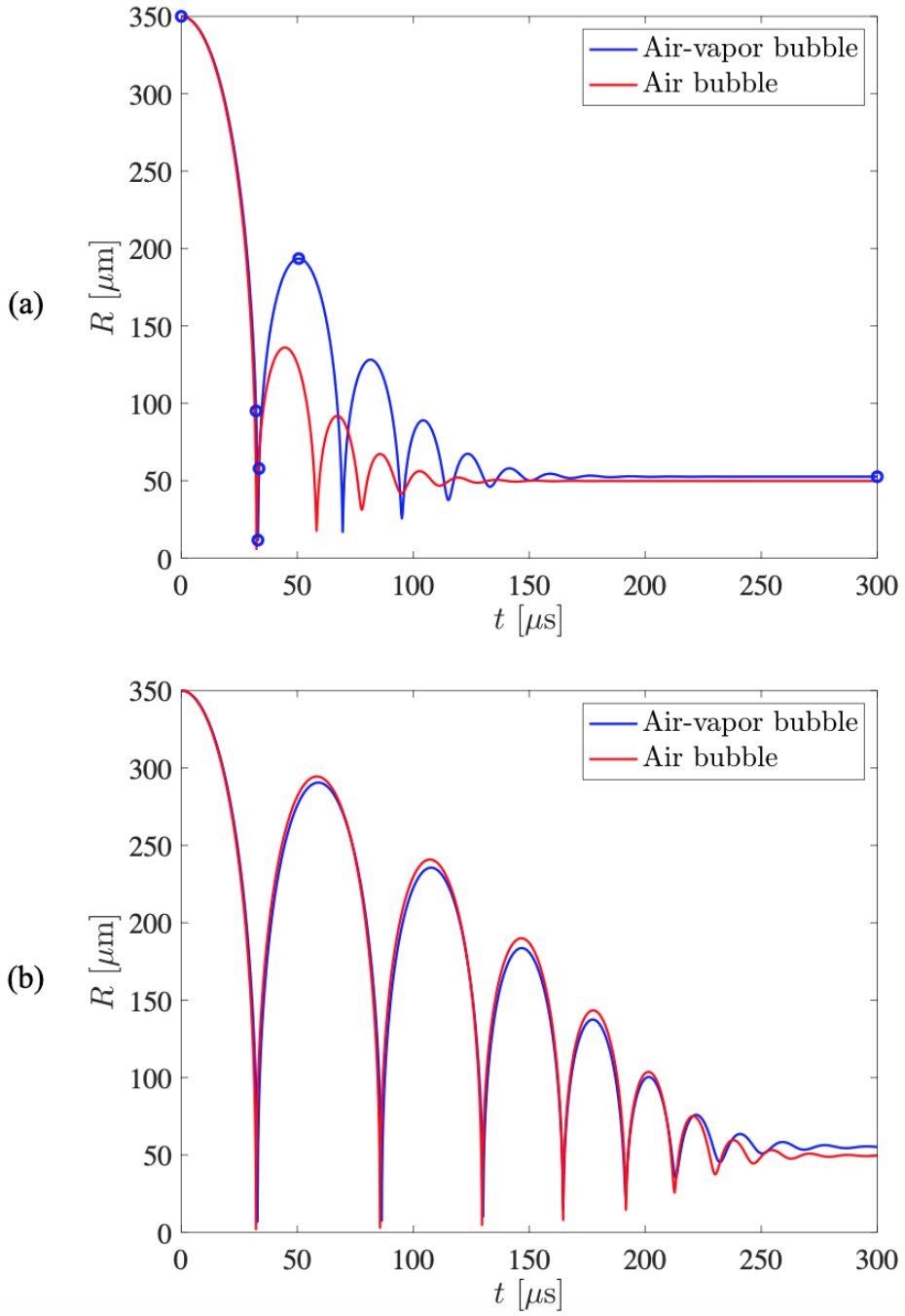

Figure 3.6: Comparison of the laser-induced collapse in a soft polyacrylamide gel between an air-vapor bubble and a pure air bubble. (a) Solutions of the (weakly compressible) Keller–Miksis equation. The blue circles correspond to $t = 0, 32.2, 33.0, 33.5, 50.6, 300$ μs at which temperature and mass fraction fields are shown in figure 3.7. (b) Solutions of the (incompressible) Rayleigh–Plesset equation.

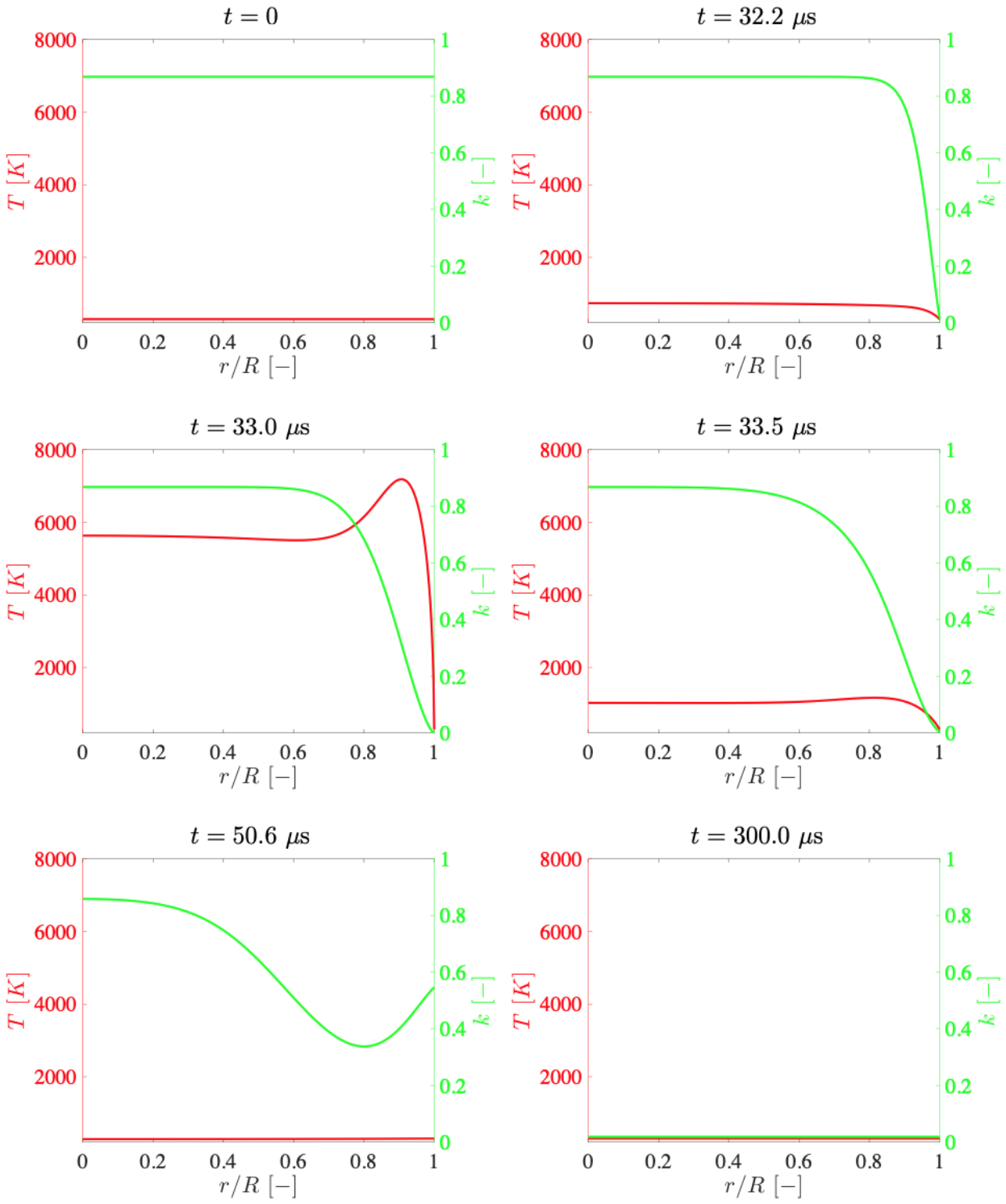

Figure 3.7: Temperature $T(r,t)$ and mass fraction of vapor $k(r,t)$ fields inside an air-vapor bubble at different times during the inertial collapse. The snapshots correspond to the blue circles represented in figure 3.6 (a). The collapse is so rapid compared to the mass diffusion that a large amount of vapor is trapped by an air shell. When the bubble reaches R_{min} at $t = 33.0\,\mu s$, the maximum temperature is induced near the bubble wall in the air-dominated region.

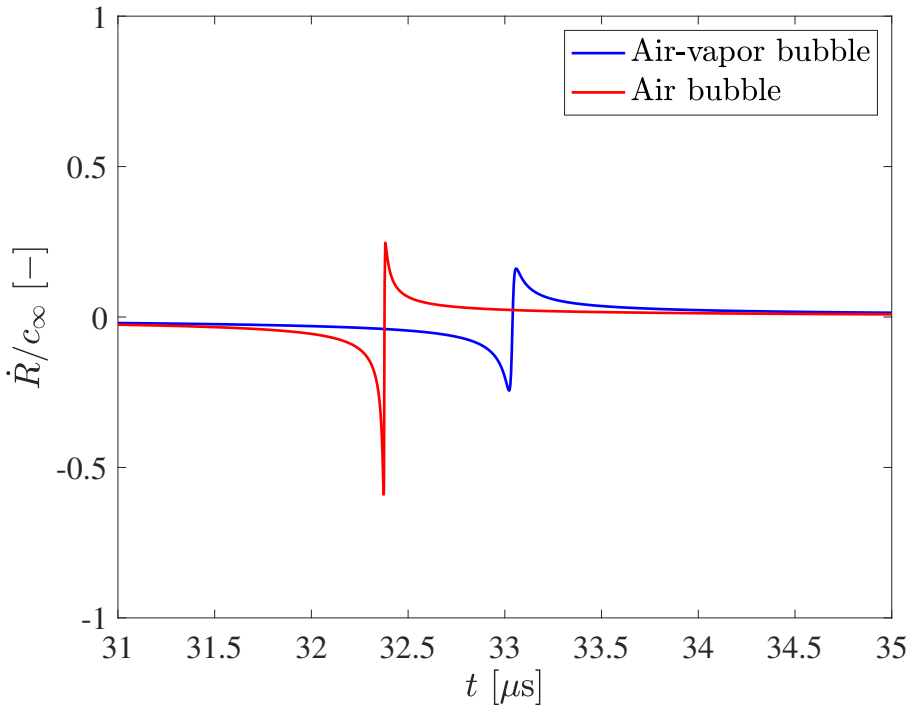

Figure 3.8: Time history of the bubble wall velocity during the first inertial collapse in figure 3.6 (a). The air-vapor bubble reaches a smaller velocity.

To understand why the air-vapor bubble rebounds to a larger size, we also take a look at the solutions of the (incompressible) Rayleigh–Plesset equation (2.4). The incompressible solutions for the air-vapor bubble and the pure air bubble are compared in figure 3.6 (b). Because of the trapped vapor, the air-vapor bubble collapses to a larger minimum radius (R_{min} = 7.0 μm) than that of the pure air bubble (R_{min} = 2.1 μm). However, the difference in the rebound amplitude between the incompressible solutions is quite small, which suggests that the large discrepancy in figure 3.6 (a) stems from compressible effects. Figure 3.8 shows the time history of the bubble wall velocity normalized by the sound speed during the first inertial collapse in figure 3.6 (a). The air-vapor bubble reaches a smaller velocity during the collapse ($\max|\dot{R}/c_\infty| = 0.25$) than the pure air bubble does ($\max|\dot{R}/c_\infty| = 0.59$), such that energy losses by acoustic radiation to the surroundings are smaller. As a result, the air-vapor bubble has higher internal energy at collapse and is therefore able to rebound to a larger size than the pure air bubble.

We examine the dependence of the solution on the initial profile of mass fraction field. The

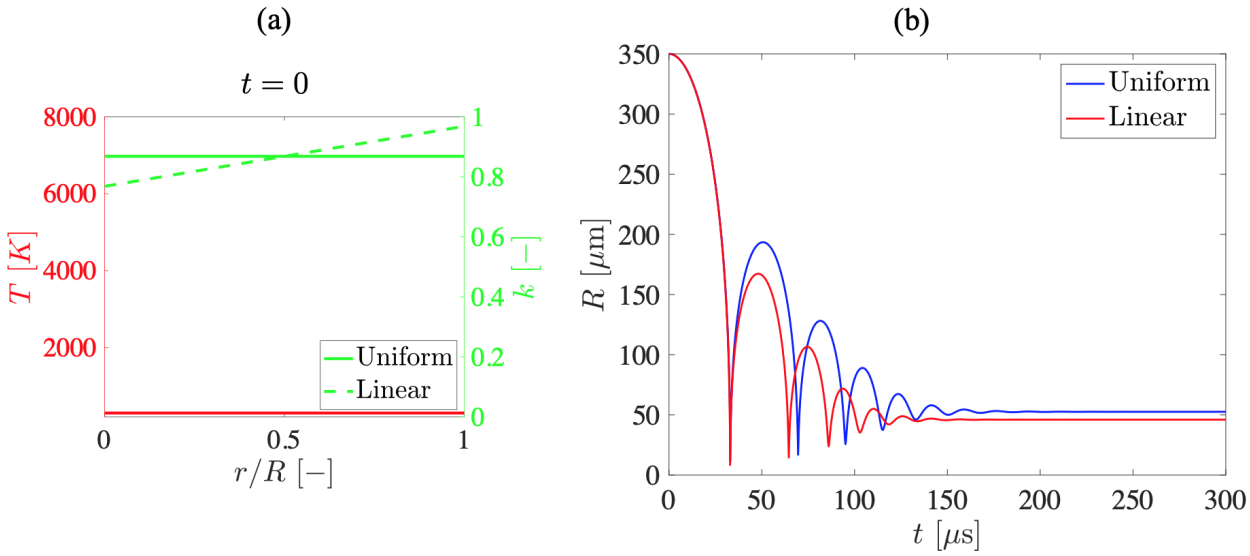

Figure 3.9: Solutions for the laser-induced bubble collapse with different initial profiles of the mass fraction field. (a) Initial temperature and mass fraction of vapor fields inside the bubble, given by two different profiles: uniform and linear profiles. (b) Comparison between solutions with the two different initial profiles.

initial temperature field is kept uniform and equal to the cold liquid temperature, while two different profiles are considered for the initial mass fraction field: uniform and linear profiles, as shown in figure 3.9 (a). Note that the initial bubble pressure is still set to equation (3.36) with the same equilibrium radius $R_{eq} = 50\ \mu$m and saturated vapor pressure $p_{v,sat}(T_\infty) = 3.1$ kPa. Figure 3.9 (b) shows solutions for the laser-induced collapse of an air-vapor bubble in a soft polyacrylamide gel with the two different initial profiles. The bubble which initially has a linear profile collapses with a larger velocity ($\max|\dot{R}/c_\infty| = 0.37$) than the other bubble does ($\max|\dot{R}/c_\infty| = 0.25$), resulting in larger energy losses and thus a smaller rebound. This is because the amount of the trapped vapor is smaller if the bubble initially has a linear profile with less vapor at the bubble center. Therefore, the initial profile of mass fraction field inside the bubble has an impact on the inertial collapse.

3.6 Validation

Our analysis of the role of gas-vapor mixture transport on inertial collapse is validated by comparing with experiments of the laser-induced bubble collapse in 50 wt% glycerol. Glycerol is

Property	Value
ρ_∞	1131 kg/m^3
c_∞	1886 m/s
σ	0.069 N/m
μ	5.9 mPa $\cdot$ s
G	0

Table 3.5: Physical properties of 50 wt% glycerol.

non-volatile with saturated vapor pressure close to zero, such that the vaporization is expected to be small. Therefore, our numerical solutions with a small amount of vapor are expected to agree with experiments. Another advantage with using 50 wt% glycerol[8] rather than hydrogels is that the material properties are well characterized (Takamura *et al.*, 2012; Negadi *et al.*, 2017); in particular, 50 wt% glycerol is a Newtonian fluid with no shear modulus $G = 0$. The physical properties of 50 wt% glycerol at STP are listed in table 3.5. Note that the viscosity is measured under quasi-static conditions with Cannon-Fenske viscometers (Takamura *et al.*, 2012). We numerically investigate the dependence of bubble dynamics on the saturated vapor pressure $p_{v,sat}$, which is the boundary condition $p_{v,w} = p_{v,sat}$ and also the initial condition $p_v(r, t = 0) = p_{v,sat}$, and compare with experiments.

The experiments were conducted by Ms. Selda Buyukozturk, Mr. Harry Cramer, and Prof. Christian Franck from the University of Wisconsin. The laser-induced bubble growth and subsequent collapses are recorded by a high-speed camera (HPV-X2, Shimadzu), as illustrated in figure 3.10. The glycerol sample is prepared in a 35 mm cylindrical glass bottomed container, which effectively avoids any edge effects from the container. A Q-switched Nd:YAG laser pulse (Amplitude) with a wavelength of 532 nm and pulse duration of 4 $\pm$ 0.3 ns is expanded and aligned into the back port of a Ti2 Nikon Microscope. A 532 nm dichroic notch filter passes the laser through the back aperture of a microscope objective (10x, NA = 0.3), focusing the laser into the glycerol

[8]The reason why we use the concentration of 50 wt% rather than 100 wt% is because the viscosity of 100 wt% glycerol heavily depends on temperature (Takamura *et al.*, 2012). For example, $\mu = 1.49$ Pa $\cdot$ s at 20 °C and $\mu = 0.70$ Pa $\cdot$ s at 30 °C for the 100 wt% glycerol. The viscous contribution in the Rayleigh–Plesset-type model only originates from the boundary conditions at the bubble wall (Brennen, 1995), which could be influenced by temperature variations during each collapse. On the other hand, $\mu = 0.0061$ Pa $\cdot$ s at 20 °C and $\mu = 0.0057$ Pa $\cdot$ s at 30 °C for 50 wt% glycerol, thus the fluctuation is negligible.

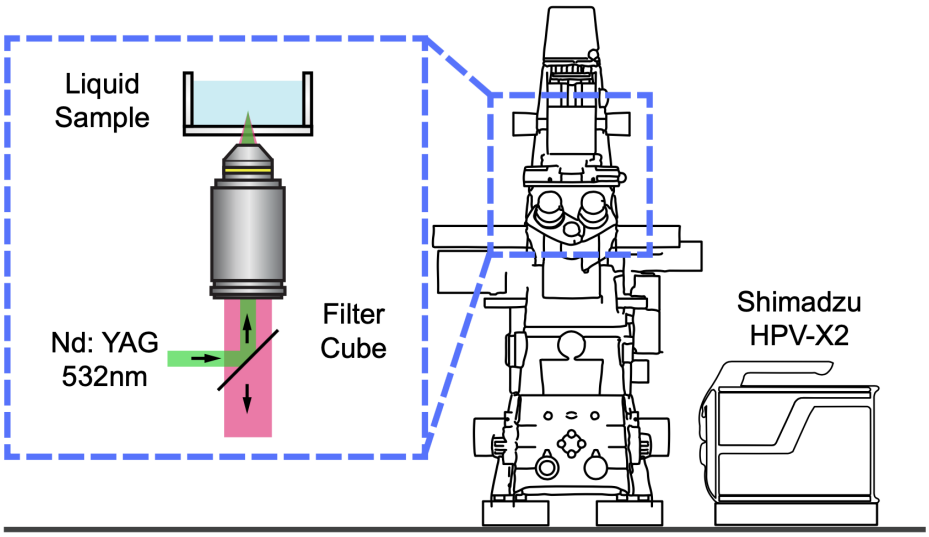

Figure 3.10: Schematic illustration of the experimental setup for recording the laser-induced bubble collapse. The resolutions of the high-speed camera is set to 500 kfps and 3.2 μm/pixel.

sample 1200 μm off the bottom of the container. Bright-field imaging of the bubble event with backlighting of LED illumination transmits through the dichroic notch filter, and is recorded by the high-speed camera. With the limited 256 consecutive frames, the temporal resolutions of the high-speed camera is set to 500 kfps to ensure that the equilibrium bubble radius R_{eq} occuring long after the oscillations is captured.

We compare our numerical solutions with different saturated vapor pressures to the experimental results of the laser-induced bubble collapse in 50 wt% glycerol in figure 3.11. A series of recorded images in figure 3.11 (a) show that the bubble maintains its spherical shape throughout the process. This bubble reaches a maximum radius $R_{max} = 419.6\,\mu$m and oscillates to an equilibrium radius of $R_{eq} = 95.6\,\mu$m. We initialize the simulations at the maximum radius as described in section 3.3. In figure 3.11 (b), the evolution of the area-equivalent radius is compared to the numerical solutions with three different saturated vapor pressures $p_{v,sat} = 3100, 810, 0$ Pa. Correspondingly, the initial mass fraction fields are set to $k(r, t = 0) = 0.62, 0.30, 0$, respectively. Because trapped vapor leads to less energy losses (see section 3.5), the bubble rebounds to a larger size when it initially contains more vapor. The solutions with lower saturated vapor pressure agree well with the experiments, which is consistent with the fact that glycerol is non-volatile and thus

the vaporization is expected to be small. This comparison provides confidence in the validity of our analysis on the role of gas-vapor mixture transport.

3.7 The validity of the constant-γ assumption

The validity of the constant-γ assumption $\gamma = \gamma_g = \gamma_v$ is examined by comparing solutions between the gas-vapor model and the constant-γ model. Numerical solutions for laser-induced collapse of an air-vapor bubble in a soft polyacrylamide gel (table 3.4) are shown in figure 3.12 (a) for three different stretch ratios $R_{max}/R_{eq} = 3, 5, 7$ where $R_{eq} = 50\,\mu$m. The ratio of specific heats of air $\gamma = 1.4$ is used for the constant-γ model. As the stretch ratio is increased, the solutions of the constant-γ model (dashed lines) deviate more from those of the gas-vapor model (solid lines). The discrepancy in the second maximum radius between the two models is 1.1% of R_{max} for $R_{max}/R_{eq} = 3$ and 2.4% of R_{max} (dimensionally 8.4 μm) for $R_{max}/R_{eq} = 7$. These discrepancies accumulate over time and result in significant differences in the oscillation period. The spatial resolution in experiments is usually a few microns per pixel (see figure 3.10 or figure 2.5 in chapter 2), thus the discrepancy is not negligible for strong collapse cases.

The discrepancy is expected to be larger for an argon-vapor bubble because the difference in ratio of specific heats is larger between argon ($\gamma = 1.67$) and vapor ($\gamma = 1.33$). Numerical solutions for laser-induced collapse of an argon-vapor bubble in a soft polyacrylamide gel are shown in figure 3.12 (b) for three different stretch ratios $R_{max}/R_{eq} = 3, 5, 7$ where $R_{eq} = 50\,\mu$m. The ratio of specific heats of argon $\gamma = 1.67$ is used for the constant-γ model. The discrepancy in the second maximum radius between the gas-vapor model and the constant-γ model is 4.0% of R_{max} for $R_{max}/R_{eq} = 3$ and 5.0% of R_{max} (dimensionally 17.5 μm) for $R_{max}/R_{eq} = 7$, which are large deviations compared to the experimental resolutions. As expected, the errors due to the constant-γ assumption are significantly larger with an argon-vapor bubble than with an air-vapor bubble.

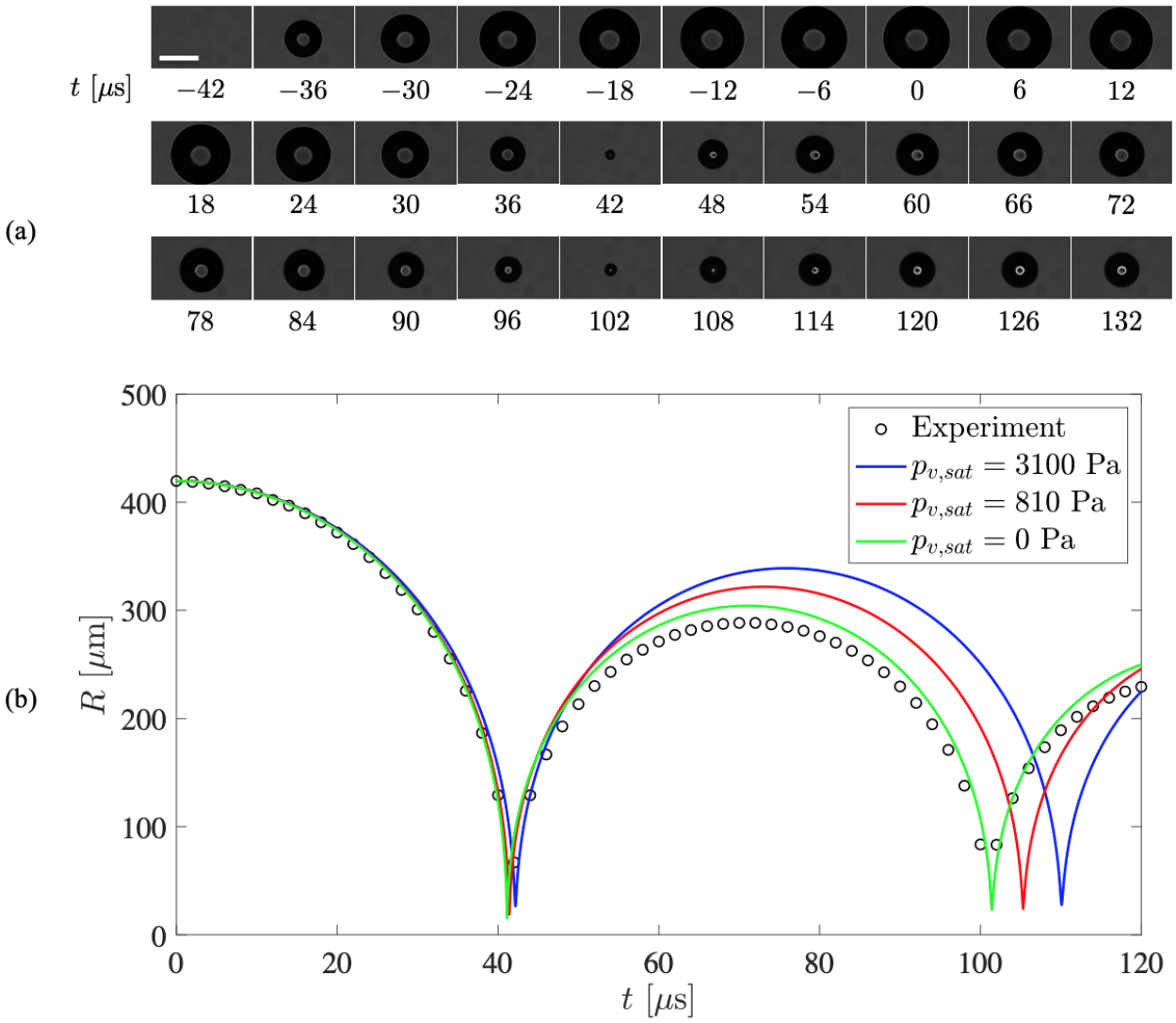

Figure 3.11: Laser-induced bubble collapse in 50 wt% glycerol. (a) A series of recorded images from the experiments. The bubble reaches $R_{max} = 419.6\,\mu$m at $t = 0$ and oscillates to $R_{eq} = 95.6\,\mu$m. The scale bar represents 500 μm. (b) Evolution of the area-equivalent radius compared to the numerical solutions with three different saturated vapor pressures $p_{v,sat} = 3100, 810, 0$ Pa. The solutions with lower saturated vapor pressure show better agreement.

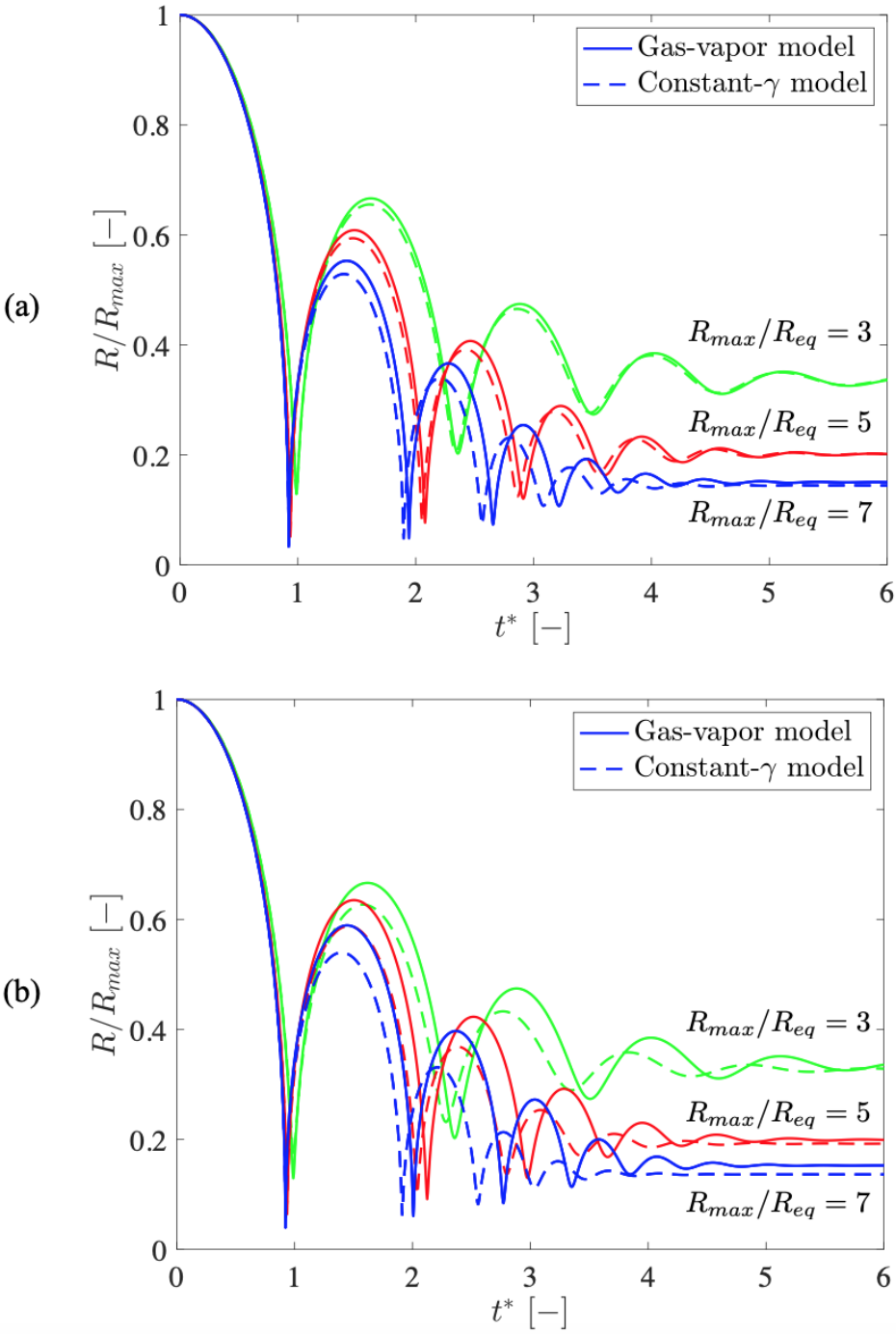

Figure 3.12: Comparison of the laser-induced collapse of a gas-vapor bubble in a soft polyacrylamide gel between the gas-vapor model and the constant-γ model. (a) Solutions for an air-vapor bubble with three different stretch ratios $R_{max}/R_{eq} = 3, 5, 7$ where $R_{eq} = 50\,\mu$m. (b) Solutions for an argon-vapor bubble with three different stretch ratios $R_{max}/R_{eq} = 3, 5, 7$ where $R_{eq} = 50\,\mu$m, showing larger discrepancies than the air-vapor bubble.

3.8 Conclusions

We develop a model for gas-vapor bubble dynamics and investigate the role of gas-vapor mixture transport on inertial bubble collapse in soft matter. The conservation laws in conjunction with the ideal gas law reduce to an ODE for homobaric bubble pressure and two PDEs for temperature and mass fraction of vapor, in which different ratios of specific heats for the gas and vapor are taken into account. A linear approximation of mixture thermal conductivity is introduced to avoid numerical errors. Numerical solutions of the model indicate that a large amount of vapor is trapped within an air shell during inertial collapse, such that the maximum temperature is induced near the bubble wall in the air-dominated region rather than at the bubble center. Furthermore, the trapped vapor reduces the bubble collapse velocity and thus energy losses via acoustic radiation, leading to a larger bubble rebound. This analysis of the role of gas-vapor mixture transport is consistent with experiments of laser-induced bubble collapse in 50 wt% glycerol, where vaporization is expected to be small in this non-volatile liquid. Comparison of numerical solutions between the gas-vapor and conventional constant-γ models show that the constant-γ assumption $\gamma = \gamma_g = \gamma_v$ results in experimentally measurable discrepancies of several percent. This discrepancy is prominent for an argon-vapor bubble due to the significantly different ratio of specific heats.

This study of gas-vapor mixture transport improves the fidelity of the cavitation model used in IMR to appropriately predict inertial bubble collapse in soft materials toward material characterization. Simulations of the new gas-vapor model are slow, which could be addressed by implementing implicit methods for time marching. This is important because IMR requires an ensemble of simulations to be run over a wide parameter range of viscosity and shear modulus (Estrada *et al.*, 2018). Another goal of this thesis is to understand the applicable conditions for IMR, which relies on calculating the spherical bubble radius. Furthermore, we observe in chapter 2 that the bubble becomes non-spherical when the oscillation amplitude increases. Therefore, we study the shape stability of a bubble in soft matter in chapters 4 and 5.

CHAPTER 4

Perturbation Analysis on a Spherical Interface Between a Gas and a Soft Solid

This chapter is adapted from Murakami *et al.* (2020a) and Gaudron *et al.* (2020).

4.1 Introduction

We conduct perturbation analysis on a spherical interface between a gas and a soft solid to determine the shape stability of a bubble in soft matter. In chapters 2 and 3, we studied spherical bubble dynamics. However, bubbles often deviate from a spherical shape in practice. In particular, Inertial Microcavitation high strain-rate Rheometry (IMR) relies on the model for spherical bubble dynamics (Estrada *et al.*, 2018), so it is important to be able to predict when the bubble dynamics depart from a spherical shape. However, studies of shape instabilities have been mostly limited to a bubble in water (Plesset, 1954; Prosperetti, 1977b). This chapter presents the first model describing non-spherical perturbations along the bubble surface in soft matter. The idea is to extend classical perturbation analysis on a plane interface (e.g., Rayleigh–Taylor instability) to a spherical interface between a gas and a soft solid. This model is capable of predicting shape instabilities during inertial bubble collapse as well as ultrasound-induced bubble oscillations (see chapter 5).

Under the homobaric and cold liquid assumptions (see chapter 2), we solve the conservation laws for the soft solid surrounding the bubble with non-spherical perturbations given by spherical harmonics. For an incompressible and irrotational soft solid, we first find the velocity potential

satisfying Laplace's equation. Then, Cauchy's equation of motion is integrated from the non-spherical bubble surface to infinity, resulting in two Ordinary Differential Equations (ODEs): one for the base state (mean bubble radius), and the other for the perturbation amplitude. For the stress tensor in the soft solid, we use the Kelvin–Voigt constitutive equation with neo-Hookean elasticity, which has been validated by the experiments in hydrogels (see chapter 2). In addition, contributions of the viscous rotational field are linearly superposed following the procedure of Prosperetti (1977b). Although this chapter focuses primarily on the methodology, we introduce numerical solutions of the model for free oscillations of a non-spherical bubble in water and in soft matter, and observe the viscoelasticity effects on the non-spherical perturbation.

4.2 General formulation

We consider a non-spherical bubble in an infinite soft solid of constant density ρ_∞ and temperature T_∞, described in spherical coordinates by the radial distance r, the polar angle θ and the azimuthal angle φ, as shown in figure 4.1, where $R(t)$ is the mean (volume-equivalent[1]) bubble radius, t is time, $\mathbf{u}(r,\theta,\varphi,t)$ is the velocity vector and $p_b(t)$ is the homobaric bubble pressure. Classical perturbation analysis on a plane interface (e.g., Rayleigh–Taylor instability) based on potential flow theory is extended to a spherical interface between a gas and a soft solid. The perturbations on a spherical interface are described by spherical harmonics (Plesset, 1954). For an incompressible ($\nabla\cdot\mathbf{u}=0$) and irrotational ($\nabla\times\mathbf{u}=\mathbf{0}$) soft solid, a velocity potential ϕ satisfies Laplace's equation $\nabla^2\phi=0$, which is solved by separation of variables in spherical coordinates,

$$\phi = \mathsf{R}(r)\mathsf{Y}(\theta,\varphi), \tag{4.1}$$

where

$$\mathsf{R}(r) = Ar^n + Br^{-n-1}, \quad \mathsf{Y}(\theta,\varphi) = Y_n^m(\theta,\varphi), \tag{4.2}$$

[1]Proof that the bubble volume is not affected by the perturbations given by spherical harmonics is available in the appendix of Gaudron *et al.* (2020).

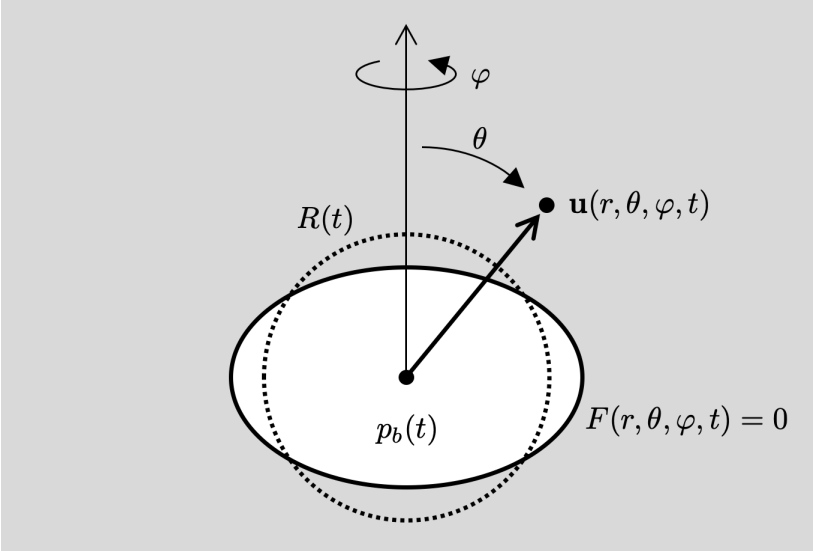

Figure 4.1: Coordinates for a non-spherical bubble in a soft solid.

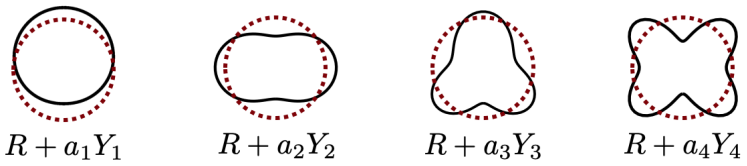

Figure 4.2: Examples of two-dimensional projections ($m = 0$) of the non-spherical bubble with a different spherical harmonic mode n.

where A and B are the constants determined by the boundary conditions, and $Y_n^m(\theta,\varphi)$ is the spherical harmonic mode of degree n and order m. Since Laplace's equation is linear, the solution can be expressed by a superposition of modes. As a consequence, the zero-thickness non-spherical bubble interface can be expressed by the superposition of spherical harmonics,

$$F(r,\theta,\varphi,t) = r - R(t) - \sum_{n,m} a_n(t) Y_n^m(\theta,\varphi) = 0, \tag{4.3}$$

where $a_n(t)$ is the perturbation amplitude of the spherical harmonic mode ($n > 0$ and $|m| \leq n$) such that $|a_n(t)| \ll R(t)$. Examples of two-dimensional projections ($m = 0$) of the non-spherical bubble with a different spherical harmonic mode n are illustrated in figure 4.2.

Our goal is to find a governing equation for the perturbation amplitude $a_n(t)$, which is achieved by integrating the conservation of momentum (2.2) from the bubble surface to infinity, as the

Rayleigh–Plesset equation is derived for the spherical radius. In fact, we solve the conservation laws (2.1) to (2.3) for the soft solid surrounding the bubble[2], for which the homobaric bubble pressure $p_b(t)$ is incorporated through the boundary condition. In addition, potential flow theory enables us to find the velocity field as $\mathbf{u} = -\nabla\phi$, and then the pre-determined velocity field is substituted into the conservation of momentum (2.2). Cauchy's equation of motion is

$$\frac{\partial \mathbf{u}}{\partial t} + (\mathbf{u}\cdot\nabla)\mathbf{u} = \frac{1}{\rho_\infty}\mathrm{div}\mathbf{T}, \tag{4.4}$$

where $\mathbf{T}$ is the Cauchy stress tensor. In general, four boundary conditions apply at the bubble surface (Prosperetti, 1977b). Two are kinematic boundary conditions: no-penetration and no-slip,

$$\frac{\partial F}{\partial t} + (\mathbf{u}\cdot\nabla)F = 0, \tag{4.5}$$

$$\mathbf{u}_{t_1} = \mathbf{u}_{t_2}, \tag{4.6}$$

where the subscript t denotes the tangential component and the subscripts 1 and 2 represent the gas and solid phases, respectively. The other two are dynamic boundary conditions for normal and shear stresses,

$$\mathbf{n}\cdot\mathbf{T}_2\mathbf{n} - \mathbf{n}\cdot\mathbf{T}_1\mathbf{n} = \sigma\nabla\cdot\mathbf{n}, \tag{4.7}$$

$$\mathbf{n}\times\mathbf{T}_2\mathbf{n} - \mathbf{n}\times\mathbf{T}_1\mathbf{n} = \mathbf{0}, \tag{4.8}$$

where σ is the surface tension. The normal unit vector at the bubble surface is

$$\mathbf{n} = \frac{\nabla F}{|\nabla F|} = \left\{ \begin{array}{c} 1 \\ -\dfrac{1}{r}a_n\dfrac{\partial Y_n^m}{\partial\theta} \\ -\dfrac{1}{r\sin\theta}a_n\dfrac{\partial Y_n^m}{\partial\varphi} \end{array} \right\}. \tag{4.9}$$

[2]Conservation of energy (2.3) is not solved because we have the cold liquid assumption $T(r,t) = T_\infty$ $(r \geq R)$.

4.3 Velocity potential

We consider the perturbation of a single non-spherical mode n to be superposed on the base state (spherical mode) as $\phi = \phi_S + \phi_{NS}$. The velocity potential for the base state is (Brennen, 1995)

$$\phi_S = \frac{R^2\dot{R}}{r}, \tag{4.10}$$

which is a source or sink at the origin. The velocity potential for the single non-spherical mode is given by equation (4.1). The boundary condition at infinity where the velocity vanishes ($\phi \to 0$ as $r \to \infty$) gives $A = 0$, thus

$$\phi_{NS} = B\frac{1}{r^{n+1}}Y_n^m. \tag{4.11}$$

The no penetration condition (4.5) reduces to (Plesset, 1954)

$$\mathbf{u}\cdot\mathbf{n}|_w = \dot{R} + \dot{a}_n Y_n^m, \tag{4.12}$$

where w denotes the value evaluated at the non-spherical bubble wall $r = R + a_n Y_n^m$. This boundary condition gives the constant B, and to the order $O(a_n)$, the velocity potential is determined as

$$\phi = \frac{R^2\dot{R}}{r} + \frac{R^{n+2}}{(n+1)r^{n+1}}\left(\dot{a}_n + \frac{2\dot{R}}{R}a_n\right)Y_n^m. \tag{4.13}$$

4.4 Viscoelastic stress tensor

The viscoelastic nature of the soft solid is modeled by the Kelvin–Voigt constitutive equation (see figure 2.2 in chapter 2); the stress tensor is

$$\mathbf{T} = \mathbf{T}_v + \mathbf{T}_e, \tag{4.14}$$

where the viscous stress is Newtonian and the elastic stress includes a neo-Hookean term and pressure (Gaudron *et al.*, 2015). The viscous stress tensor is

$$\mathbf{T}_v = 2\mu\mathbf{S} = \begin{bmatrix} 2\mu\dfrac{\partial u_r}{\partial r} & \mu\dfrac{1}{r}\dfrac{\partial u_r}{\partial \theta} & \mu\dfrac{1}{r\sin\theta}\dfrac{\partial u_r}{\partial \varphi} \\ \mu\dfrac{1}{r}\dfrac{\partial u_r}{\partial \theta} & 2\mu\dfrac{u_r}{r} & 0 \\ \mu\dfrac{1}{r\sin\theta}\dfrac{\partial u_r}{\partial \varphi} & 0 & 2\mu\dfrac{u_r}{r} \end{bmatrix}, \tag{4.15}$$

where μ is the viscosity and $\mathbf{S}$ is the strain rate tensor. The elastic stress tensor is

$$\mathbf{T}_e = G\mathbf{B} - \mathcal{P}\mathbf{I}, \tag{4.16}$$

where G is the shear modulus, $\mathbf{B} = \mathbf{F}\mathbf{F}^{\mathrm{T}}$ is the left Cauchy–Green tensor, $\mathcal{P}$ is the pseudo-pressure and $\mathbf{I}$ is the identity matrix. We consider irrotational deformations: the original configuration is $\mathbf{x}_0 = r_0\mathbf{e}_r$ and the current configuration is $\mathbf{x} = r(r_0, \theta, \varphi, t)\mathbf{e}_r$. Then, the deformation gradient tensor is

$$\mathbf{F} = \frac{\partial \mathbf{x}}{\partial \mathbf{x}_0} = \begin{bmatrix} \dfrac{\partial r}{\partial r_0} & \dfrac{1}{r_0}\dfrac{\partial r}{\partial \theta} & \dfrac{1}{r_0\sin\theta}\dfrac{\partial r}{\partial \varphi} \\ 0 & \dfrac{r}{r_0} & 0 \\ 0 & 0 & \dfrac{r}{r_0} \end{bmatrix}. \tag{4.17}$$

The deformation is also incompressible ($\det\mathbf{F} = 1$), which leads to

$$\frac{\partial r}{\partial r_0} = \left(\frac{r_0}{r}\right)^2. \tag{4.18}$$

The polar and azimuthal gradients of the current configuration $\partial r/\partial\theta$ and $\partial r/\partial\varphi$ are of order $O(a_n)$ (see Appendix C). Therefore, to the order $O(a_n)$, the elastic stress tensor results in[3]

$$\mathbf{T}_e = \begin{bmatrix} G\left(\frac{r_0}{r}\right)^4 - \mathcal{P} & G\frac{r}{r_0^2}\frac{\partial r}{\partial\theta} & G\frac{r}{r_0^2\sin\theta}\frac{\partial r}{\partial\varphi} \\ G\frac{r}{r_0^2}\frac{\partial r}{\partial\theta} & G\left(\frac{r}{r_0}\right)^2 - \mathcal{P} & 0 \\ G\frac{r}{r_0^2\sin\theta}\frac{\partial r}{\partial\varphi} & 0 & G\left(\frac{r}{r_0}\right)^2 - \mathcal{P} \end{bmatrix}. \tag{4.19}$$

4.5 Irrotational model

Given the velocity potential (4.13) and stress tensors (4.15) and (4.19), a governing equation for the perturbation amplitude $a_n(t)$ is obtained by integrating Cauchy's equation of motion (4.4) from the non-spherical bubble surface to infinity. The integration results in

$$\begin{aligned} \mathcal{P} &= p_\infty + \rho_\infty\left[R\ddot{R} + \frac{3}{2}\dot{R}^2 + \frac{3\dot{R}\dot{a}_n + R\ddot{a}_n - (n-1)\ddot{R}a_n}{n+1}Y_n^m\right] \\ &\quad + \frac{G}{2}\left[5 - 4\left(\frac{R_{eq}}{R}\right) + \left(\frac{R_{eq}}{R}\right)^4\right] + \frac{G}{R}\left[2\frac{R_{eq}}{R} - 2\left(\frac{R_{eq}}{R}\right)^4 + \frac{n(n+1)}{1 + \frac{R_{eq}}{R} + \left(\frac{R_{eq}}{R}\right)^2}\right]a_nY_n^m, \end{aligned} \tag{4.20}$$

where $p_\infty(t)$ is the far-field pressure, R_{eq} is the equilibrium bubble radius, and the divergence of viscous stress vanishes[4]. The dynamic boundary condition for normal stresses (4.7) reduces to

$$2\mu\frac{\partial u_r}{\partial r} + G\left(\frac{r_0}{r}\right)^4 - \mathcal{P} + p_b = \frac{2\sigma}{R} + \frac{(n-1)(n+2)}{R^2}\sigma a_nY_n^m, \tag{4.21}$$

[3]Our elastic stress tensor applies to incompressible and irrotational deformations. One way to confirm this fact is to consider the following vorticity equation for incompressible flow $\partial\boldsymbol{\omega}/\partial t + \mathbf{u}\cdot\nabla\boldsymbol{\omega} - \boldsymbol{\omega}\cdot\nabla\mathbf{u} = \nabla\times(\nabla\cdot\mathbf{T})/\rho_\infty$ where $\boldsymbol{\omega}$ is the vorticity vector. This equation leads to $\nabla\times(\nabla\cdot\mathbf{T}) = \mathbf{0}$ under the irrotational assumption ($\boldsymbol{\omega} = \mathbf{0}$), which the elastic stress tensor (4.19) satisfies.

[4]Using the vector identity, the viscous term in the incompressible Navier–Stokes equation is $\mu\nabla^2\mathbf{u} = \mu[\nabla(\nabla\cdot\mathbf{u}) - \nabla\times(\nabla\times\mathbf{u})]$, which is identically zero under the incompressible and irrotational assumptions. For the irrotational model, the viscous contribution stems from the dynamics boundary condition (4.21) only.

where the property of the spherical harmonics $r^2\nabla^2 Y_n^m = -n(n+1)Y_n^m$ is used to calculate $\nabla \cdot \mathbf{n}$. Evaluating equation (4.21) at the non-spherical bubble surface $r = R + a_n Y_n^m$ to order $O(1)$ gives a nonlinear ODE for the base state (mean bubble radius):

$$R\ddot{R} + \frac{3}{2}\dot{R}^2 = \frac{1}{\rho_\infty}\left\{p_b - p_\infty - \frac{2\sigma}{R} - \frac{4\mu\dot{R}}{R} - \frac{G}{2}\left[5 - 4\frac{R_{eq}}{R} - \left(\frac{R_{eq}}{R}\right)^4\right]\right\}, \tag{4.22}$$

which is exactly the Rayleigh–Plesset equation (2.4) with the Kelvin-Voigt stress integral with nonlinear elasticity (2.6). To order $O(a_n)$, a linear ODE for the perturbation amplitude of a non-spherical mode $a_n(t)$ is obtained as

$$\ddot{a}_n + A_n\dot{a}_n + B_n a_n = 0, \tag{4.23}$$

where

$$A_n = 3\frac{\dot{R}}{R} + 2(n+1)(n+2)\frac{\mu}{\rho_\infty R^2}, \tag{4.24}$$

$$B_n = -(n-1)\frac{\ddot{R}}{R} + 4(n-1)(n+1)\frac{\mu\dot{R}}{\rho_\infty R^3} + (n-1)(n+1)(n+2)\frac{\sigma}{\rho_\infty R^3} + (n+1)\frac{G}{\rho_\infty R^2}\left[2\frac{R_{eq}}{R} + 2\left(\frac{R_{eq}}{R}\right)^4 + \frac{n(n+1)}{1 + \frac{R_{eq}}{R} + \left(\frac{R_{eq}}{R}\right)^2}\right]. \tag{4.25}$$

This is the result of the perturbation analysis extended to a spherical interface between a gas and a soft solid. The stability of the non-spherical perturbation can be analyzed by the linear ODE (4.23).

4.6 Rotational corrections

4.6.1 Field decomposition

In addition to the perturbation on the potential flow, we linearly superpose the contributions of viscous rotational field following the procedure of Prosperetti (1977b). We decompose the velocity

field as

$$\mathbf{u} = \mathbf{u}_0 + \epsilon\mathbf{u}_p + \epsilon\mathbf{u}_r, \tag{4.26}$$

where the subscripts 0 and p denote the base state and perturbation corresponding to the first and second terms in the velocity potential (4.13), respectively, r denotes the rotational correction, and ϵ is of order $O(|a_n|/R)$. We refer to the last term not as a viscous correction (Prosperetti, 1977b) but as a rotational correction, because even if the flow is incompressible and irrotational there is a viscous contribution from the dynamic boundary condition for normal stresses (4.21). The pressure field is decomposed accordingly,

$$p = p_0 + \epsilon p_p + \epsilon p_r. \tag{4.27}$$

After this decomposition, Cauchy's equation of motion (4.4) can be split into two parts, the first for the irrotational component:

$$\frac{\partial}{\partial t}(\mathbf{u}_0 + \epsilon\mathbf{u}_p) + [(\mathbf{u}_0 + \epsilon\mathbf{u}_p)\cdot\nabla](\mathbf{u}_0 + \epsilon\mathbf{u}_p) = \frac{1}{\rho_\infty}\mathrm{div}(\mathbf{T}_{v_{irrot}} + \mathbf{T}_e), \tag{4.28}$$

where $\mathbf{T}_{v_{irrot}}$ is the viscous stress contribution to the irrotational velocity components $\mathbf{u}_0 + \epsilon\mathbf{u}_p$, and the pressure $p_0 + \epsilon p_p$ is included in $\mathbf{T}_e$ as the pseudo-pressure $\mathcal{P}$ (see equation (4.19)). The irrotational velocity field is obtained from $\mathbf{u}_0 + \epsilon\mathbf{u}_p = -\nabla\phi$, and the pseudo-pressure is determined by integrating equation (4.28) from the non-spherical bubble surface to infinity, for which the result is equation (4.20).

The second part of Cauchy's equation of motion is for the rotational component, which is obtained by subtracting equation (4.28) from equation (4.4),

$$\frac{\partial}{\partial t}(\epsilon\mathbf{u}_r) + (\mathbf{u}_0\cdot\nabla)\epsilon\mathbf{u}_r + (\epsilon\mathbf{u}_r\cdot\nabla)\mathbf{u}_0 = \frac{1}{\rho_\infty}\mathrm{div}\mathbf{T}_{v_{rot}}, \tag{4.29}$$

where $\mathbf{T}_{v_{rot}}$ is the viscous stress contribution to the rotational velocity component $\epsilon\mathbf{u}_r$ including the pressure ϵp_r. Prosperetti (1977b) solved equation (4.29) and determined the velocity and pressure fields, which was also reviewed by Liu *et al.* (2012),

$$\epsilon\mathbf{u}_r = \mathcal{T}Y_{nm}\mathbf{e}_r - \nabla\Phi, \tag{4.30}$$

$$\epsilon p_r = \mu\frac{n}{R}\mathcal{T}(R,t)Y_{nm} + \rho_\infty n\frac{\dot{R}}{R}Y_{nm}\int_R^\infty\left[\left(\frac{R}{s}\right)^3 - 1\right]\left(\frac{R}{s}\right)^n\mathcal{T}(s,t)ds, \tag{4.31}$$

where

$$\Phi = Y_{nm}\left[\left(\alpha(t) + \frac{n+1}{2n+1}\int_R^r s^{-n}\mathcal{T}(s,t)ds\right)r^n + \left(\frac{n}{n+1}R^{2n+1}\alpha(t) + \frac{n}{2n+1}\int_R^r s^{n+1}\mathcal{T}(s,t)ds\right)r^{-(n+1)}\right], \tag{4.32}$$

$$\alpha(t) = -\frac{n+1}{2n+1}\int_R^\infty s^{-n}\mathcal{T}(s,t)ds. \tag{4.33}$$

The toroidal component[5] of the vorticity field $\mathcal{T}(r,t)$ is determined by the second-order Partial Differential Equation (PDE):

$$\rho_\infty\frac{\partial\mathcal{T}}{\partial t} + \rho_\infty\frac{\partial}{\partial r}\left[\dot{R}\left(\frac{R}{r}\right)^2\mathcal{T}\right] - \mu\frac{\partial^2\mathcal{T}}{\partial r^2} + \mu n(n+1)\frac{\mathcal{T}}{r^2} = 0, \tag{4.34}$$

which requires two boundary conditions: $\mathcal{T}\to 0$ as $r\to\infty$ and shear stress continuity (4.8) at the bubble surface. Since viscosity of the gas is much smaller than that of the soft solid, the shear stress continuity condition (4.8) reduces to a balance between viscous shear stress and elastic shear stress of the soft solid,

$$\mathcal{T}(R,t) = \frac{2(n+2)}{n+1}\dot{a}_n - \frac{2(n-1)}{n+1}\frac{\dot{R}}{R}a_n + \frac{G}{\mu}\left(\frac{R_{eq}}{R}\right)^4 a_n - 2R^{n-1}\int_R^\infty\frac{\mathcal{T}(s,t)}{s^n}ds. \tag{4.35}$$

[5] Prosperetti (1977b) solved equation (4.29) by decomposing the vorticity into poloidal and toroidal fields as $\boldsymbol{\omega} = \boldsymbol{\mathcal{S}} + \boldsymbol{\mathcal{T}}$ where $\boldsymbol{\mathcal{S}} = \nabla\times\nabla\times[\mathcal{S}(r,t)Y_n^m(\theta,\varphi)\mathbf{e}_r]$ and $\boldsymbol{\mathcal{T}} = \nabla\times[\mathcal{T}(r,t)Y_n^m(\theta,\varphi)\mathbf{e}_r]$. An advantage of this approach is that the vorticity vector can be expressed by scalar variables. The toroidal component evolves according to equation (4.34), while the poloidal component remains zero if it is initially zero.

4.6.2 The final form of the equations

The equation governing the perturbation amplitude $a_n(t)$ is obtained with the velocity field including the rotational correction (4.26). The dynamic boundary condition for normal stresses (4.7) reduces to

$$-\epsilon p_r + 2\mu\frac{\partial(\epsilon u_{r,r})}{\partial r} + 2\mu\frac{\partial(u_{0,r}+\epsilon u_{p,r})}{\partial r} + G\left(\frac{r_0}{r}\right)^4 - \mathcal{P} + p_b = \frac{2\sigma}{R} + \frac{(n-1)(n+2)}{R^2}\sigma a_n Y_n^m, \quad (4.36)$$

where $u_{0,r}$, $u_{p,r}$ and $u_{r,r}$ are the radial component of the corresponding velocity vectors. The first two terms on the left-hand side are the contributions from rotational corrections. Substituting the velocity and pressure $u_{0,r}+\epsilon u_{p,r}$, $\epsilon u_{r,r}$, $\mathcal{P}$ and ϵp_r into equation (4.36) and evaluating at the non-spherical bubble surface $r = R + a_n Y_n^m$ to order $O(1)$ gives the nonlinear ODE for the base state (4.22). To order $O(a_n)$, a linear ODE for the perturbation amplitude $a_n(t)$ is obtained as

$$\ddot{a}_n + (A_n + A_{n_{rot}})\dot{a}_n + (B_n + B_{n_{rot}})a_n + C_{n_{rot}} = 0, \quad (4.37)$$

where

$$\begin{aligned}
A_n &= 3\frac{\dot{R}}{R} + 2(n+1)(n+2)\frac{\mu}{\rho_\infty R^2}, && (4.38)\\
B_n &= -(n-1)\frac{\ddot{R}}{R} + 4(n-1)(n+1)\frac{\mu\dot{R}}{\rho_\infty R^3} + (n-1)(n+1)(n+2)\frac{\sigma}{\rho_\infty R^3} \\
&\quad + (n+1)\frac{G}{\rho_\infty R^2}\left[2\frac{R_{eq}}{R} + 2\left(\frac{R_{eq}}{R}\right)^4 + \frac{n(n+1)}{1+\frac{R_{eq}}{R}+\left(\frac{R_{eq}}{R}\right)^2}\right], && (4.39)\\
A_{n_{rot}} &= -2n(n+1)(n+2)\frac{\mu}{\rho_\infty R^2}, && (4.40)\\
B_{n_{rot}} &= 2n(n-1)(n+1)\frac{\mu\dot{R}}{\rho_\infty R^3} - n(n+1)^2\frac{G}{\rho_\infty R^2}\left(\frac{R_{eq}}{R}\right)^4, && (4.41)\\
C_{n_{rot}} &= n(n+1)(n+2)\frac{\mu}{\rho_\infty R^2}\mathcal{T}(R,t) - n(n+1)\frac{\dot{R}}{R^2}\int_R^\infty\left[1-\left(\frac{R}{s}\right)^3\right]\left(\frac{R}{s}\right)^n\mathcal{T}(s,t)ds. && (4.42)
\end{aligned}$$

The coefficients in equation (4.37) are expressed as the sum of irrotational terms A_n and B_n and rotational corrections $A_{n_{rot}}$, $B_{n_{rot}}$ and $C_{n_{rot}}$. The novelty of our non-spherical model lies in the elastic terms in equations (4.35) (third term), (4.39) (last term), and (4.41) (last term). When $G = 0$, our non-spherical model reduces to the purely viscous model of Prosperetti (1977b).

In summary, the evolution of the non-spherical bubble surface in soft matter is determined by solving two ODEs: one for the mean bubble radius (4.22), and the other for the perturbation amplitude of the non-spherical mode (4.37). The toroidal field is used to determine $C_{n_{rot}}$ by solving the PDE (4.34). The homobaric bubble pressure $p_b(t)$ is given by an appropriate model, such as the one including effects of heat and mass diffusions introduced in chapters 2 and 3. Since terms of order $O(a_n^2)$ and higher are neglected, the equations for the different non-spherical modes are not coupled and do not influence the base state $R(t)$. In other word, there is a one-way coupling between the base state $R(t)$ and the perturbation $a_n(t)$. The equation for the perturbation amplitude $a_n(t)$ has no explicit dependence on the homobaric bubble pressure and the far-field pressure, thus instability is considered to be induced by the unsteady base state $R(t)$. Although the equations are linearized in the perturbation $a_n(t)$, the oscillations of the base state $R(t)$ are allowed to be nonlinear, and nonlinear elasticity is taken into account in our model. The dimensionless form is available in Appendix A.4.

4.7 Numerical method

The non-spherical model is solved numerically as follows. The two ODEs (4.22) and (4.37) as well as the model of homobaric bubble pressure are integrated in time by the Cash–Karp Runge–Kutta method (Press *et al.*, 2007, pp. 910-915). For example, with the gas-vapor model introduced in chapter 3, our system of equations is

$$\frac{d\boldsymbol{\xi}}{dt} = \mathcal{F}(\boldsymbol{\xi}), \quad \boldsymbol{\xi} = (R^*, \dot{R}^*, a_n^*, \dot{a}_n^*, p_b^*, \tau_i^*, k_i^*)^T, \quad i = 1, ..., N_y - 1, \tag{4.43}$$

where the size of the column vector $\boldsymbol{\xi}$ is $5 + 2(N_y - 1)$. The PDE for toroidal field (4.34) is solved using the same numerical treatment as Liu *et al.* (2012). We discretize the radial coordinate $y = r/R(t)$ outside the bubble with uniform grid spacing Δy_{out} as shown in figure 4.3. The computational domain ranges $1 \leq y_i \leq y_\infty$ where $i = 0, ..., N_{y_{out}}$, on which we have a discrete toroidal field $\mathcal{T}_i^*$. We semi-discretize the convection and diffusion terms by upwind and central differences,

$$\begin{aligned}\frac{d\mathcal{T}^*}{dt^*} &= \frac{\dot{R}^*}{R^*}\left(y_i - \frac{1}{y_i^2}\right)\frac{\mathcal{T}^*_{i+1} - \mathcal{T}^*_{i-1}}{2\Delta y_{out}} + \frac{|\dot{R}^*|}{R^*}\left(y_i - \frac{1}{y_i^2}\right)\frac{\mathcal{T}^*_{i+1} - 2\mathcal{T}^*_i + \mathcal{T}^*_{i-1}}{2\Delta y_{out}} \\ &\quad + \frac{1}{\mathrm{Re}R^{*2}}\frac{\mathcal{T}^*_{i+1} - 2\mathcal{T}^*_i + \mathcal{T}^*_{i-1}}{\Delta y_{out}^2} - \left[n(n+1)\frac{1}{\mathrm{Re}R^{*2}}\frac{1}{y_i^2} - \frac{2\dot{R}^*}{R^*}\frac{1}{y_i^3}\right]\mathcal{T}_i^*, \end{aligned} \tag{4.44}$$

and integrate in time by the standard fourth-order Runge-Kutta method. The boundary conditions are given by $\mathcal{T}^*_\infty = 0$ and the shear stress continuity at the bubble surface (4.35) for $\mathcal{T}^*_w$. We use Simpson's rule to evaluate the integrals in equations (4.35) and (4.42),

$$\int_1^{y_\infty} f(y)dy \approx \frac{\Delta y_{out}}{3}\left(f_0 + f_{N_{y_{out}}} + \sum_{\substack{j=1 \\ j=\text{odd}}}^{N_{y_{out}}-1} f_j + \sum_{\substack{j=2 \\ j=\text{even}}}^{N_{y_{out}}-2} f_j\right), \tag{4.45}$$

where f is the integrand. The computational domain is set to $1 \leq y \leq y_\infty = 2$ with $N_{y_{out}} = 200$, which is enough to capture the toroidal field (see section 5.2.1 in chapter 5). We use a sufficiently small time step to satisfy the Courant-Friedrichs-Lewy (CFL) condition. For the simulations in chapter 5, $N_{y_{out}} = 200$ requires $\max(\Delta t) = 0.0001$.

4.8 Free oscillations of a non-spherical bubble in soft matter

We numerically examine free oscillations of a non-spherical bubble in water and in soft matter as an introduction to the solutions of our non-spherical model. We consider a non-spherical bubble with mean equilibrium radius $R_{eq} = 100\,\mu$m, which is initially expanded to $R_{max} = 110\,\mu$m, with perturbation modes $n = 2$ and $n = 3$. The far-field pressure is $p_\infty(t) = p_{atm}$, and the homobaric bubble pressure $p_b(t)$ is given by the pure gas model (see chapter 2). The initial conditions are

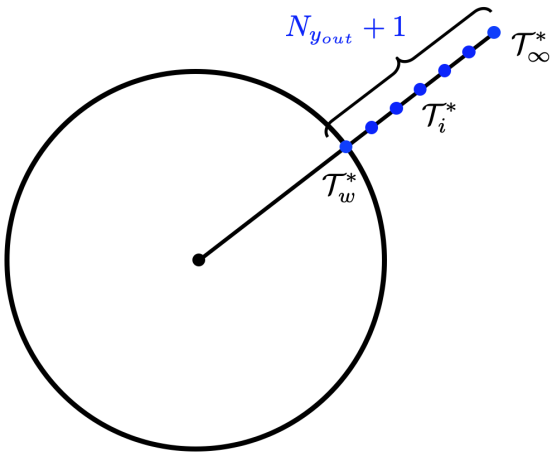

Figure 4.3: Numerical grids on the radial coordinate outside the bubble.

$R(t=0)=R_{max}$, $\dot{R}(t=0)=0$, $a_n(t=0)=0.1R_{max}$, $\dot{a}_n(t=0)=0$, $T(r,t=0)=T_\infty$, and the initial bubble pressure is given by equation (3.36). We use the irrotational model (4.22) and (4.23) in this section so that there is no contribution of the toroidal field[6]. We choose a 3 wt% gelatin gel of Hamaguchi & Ando (2015) as soft matter. The physical properties of water and the 3 wt% gelatin gel are listed in tables 4.1 and 4.2.

Numerical solutions for the free oscillations of a non-spherical bubble in water and in a 3 wt% gelatin gel are shown in figure 4.4 (a) and (b), respectively. The mean bubble radius $R(t)$ and perturbation amplitude $a_n(t)$ attenuate in time because of the viscous dissipation. The perturbation in the gel attenuates much faster and oscillates with higher frequency than that in water. This behavior can be understood by analyzing the damping rate and natural frequency of the non-spherical perturbation (see chapter 5).

The non-spherical bubble surface is expressed by the superposition of spherical harmonics of degree n and order m ($|m| \leq n$), with corresponding amplitudes $a_n(t)$ as equation (4.3). The spherical harmonics are given by

$$Y_n^m(\theta,\varphi) = K_n^m P_n^m(\cos\theta)\exp(im\varphi), \tag{4.46}$$

[6]The contributions of the rotational corrections are discussed in chapter 5.

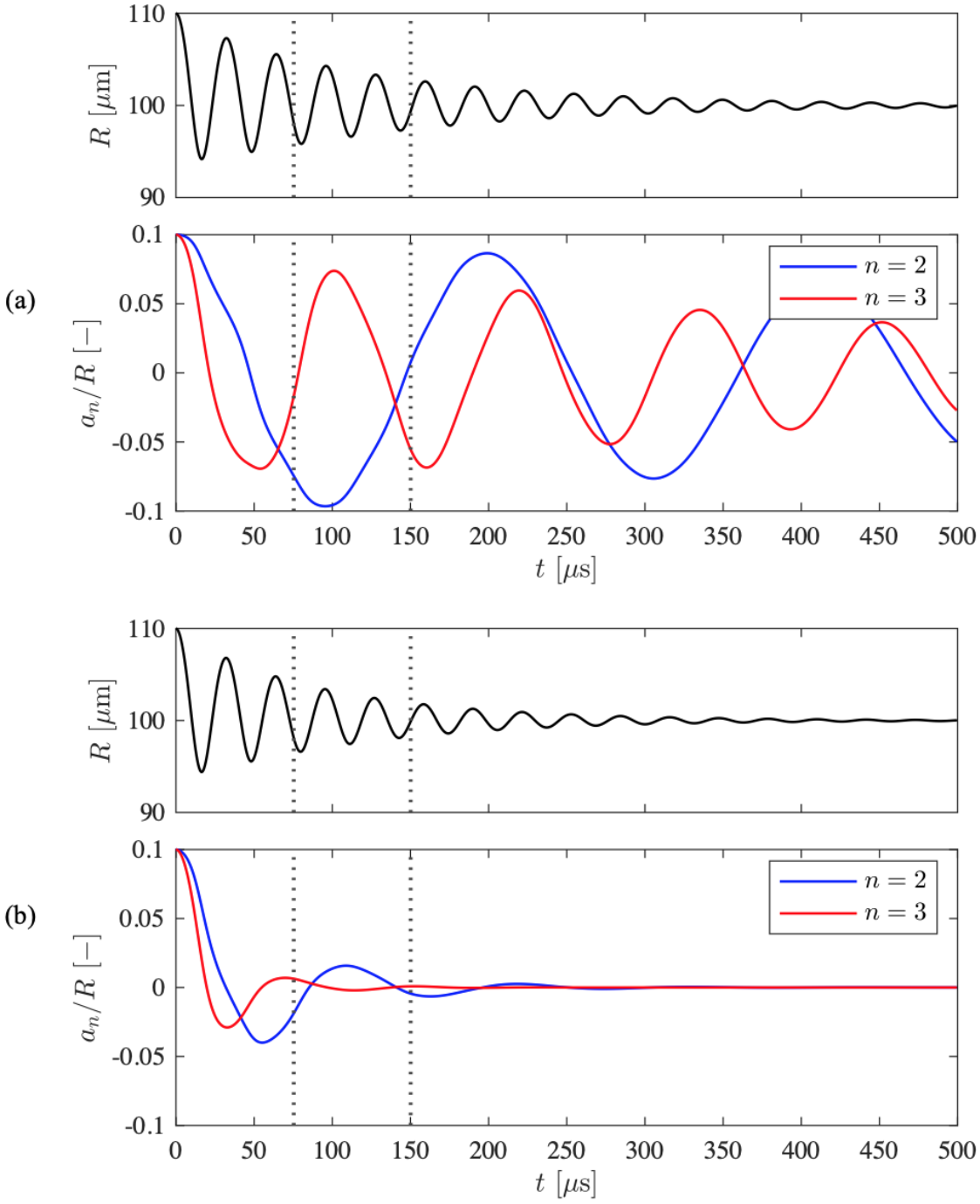

Figure 4.4: Solutions for the free oscillations of a non-spherical bubble in water and in a 3 wt% gelatin gel. (a) Solutions of the mean bubble radius (top) and perturbation amplitude of modes $n = 2$ and $n = 3$ (bottom) in water. (b) Solutions of the mean bubble radius (top) and perturbation amplitude of modes $n = 2$ and $n = 3$ (bottom) in a 3 wt% gelatin gel. The dotted lines correspond to when the non-spherical bubble shape is illustrated in figure 4.5. The perturbations attenuate much faster in the gel.

Property	Value
ρ_∞	998 kg/m^3
c_∞	1497 m/s
σ	0.072 N/m
μ	1.0 mPa · s
G	0

Table 4.1: Physical properties of water.

Property	Value
ρ_∞	998 kg/m^3
c_∞	1497 m/s
σ	0.040 N/m
μ	14.1 mPa · s
G	1.7 kPa

Table 4.2: Physical properties of a 3 wt% gelatin gel.

where K_n^m is the normalization factor, $P_n^m(\cos\theta)$ is the associated Legendre function representing the polar direction, and $e^{im\varphi}$ is the trigonometric function representing the azimuthal direction. The real part of the spherical harmonics (4.46) is taken to obtain physical quantities,

$$\Re\{Y_n^m(\theta,\varphi)\} = \begin{cases} (-1)^m \sqrt{2} K_n^{|m|} P_n^{|m|}(\cos\theta)\sin(|m|\varphi), & \text{if } m < 0, \\ K_n^m P_n^m(\cos\theta), & \text{if } m = 0, \\ (-1)^m \sqrt{2} K_n^m P_n^m(\cos\theta)\cos(m\varphi), & \text{if } m > 0. \end{cases} \tag{4.47}$$

The normalization factor is

$$K_n^m = \sqrt{\frac{2n+1}{4\pi}\frac{(n-m)!}{(n+m)!}}. \tag{4.48}$$

Figure 4.5 shows snapshots of the non-spherical bubbles in cartesian coordinates $(x_{cart}, y_{cart}, z_{cart})$ at $t = 0, 75, 150\ \mu$s in water (cyan bubble) and in the gel (green bubble), corresponding to figure 4.4. The bubble in the gel quickly converges to a spherical shape, while the bubble in water continues to exhibit non-spherical oscillations, where mode $n = 2$ is dominant at $t = 75\ \mu$s and mode $n = 3$ is dominant at $t = 150\ \mu$s. In short, the bubble surface in the gel is more stable than that in water

as the perturbation is suppressed more effectively.

4.9 Conclusions

We develop a model for non-spherical bubble dynamics in soft matter by extending classical perturbation analysis on a plane interface to a spherical interface between a gas and a soft solid. The non-spherical bubble surface is expressed by the superposition of the mean bubble radius and perturbations given by spherical harmonics. The integration of Cauchy's equation of motion from the non-spherical bubble surface to infinity results in two ODEs: one for the base state (mean bubble radius), and the other for the perturbation amplitude. Free oscillations of a non-spherical bubble in water and in a gel are numerically observed, where the perturbations in the gel are suppressed more effectively than those in water.

With the non-spherical model developed in this chapter, we can investigate the shape stability of a bubble in soft matter. We are interested in two types of instability: one is parametric instability during ultrasound-induced bubble oscillations observed in chapter 2, and the other is the Rayleigh–Taylor-type instability, that may occur during laser-induced inertial bubble collapse. In particular, the second one is important for IMR, which relies on calculating the spherical bubble radius. These shape stability problems are studied in chapter 5.

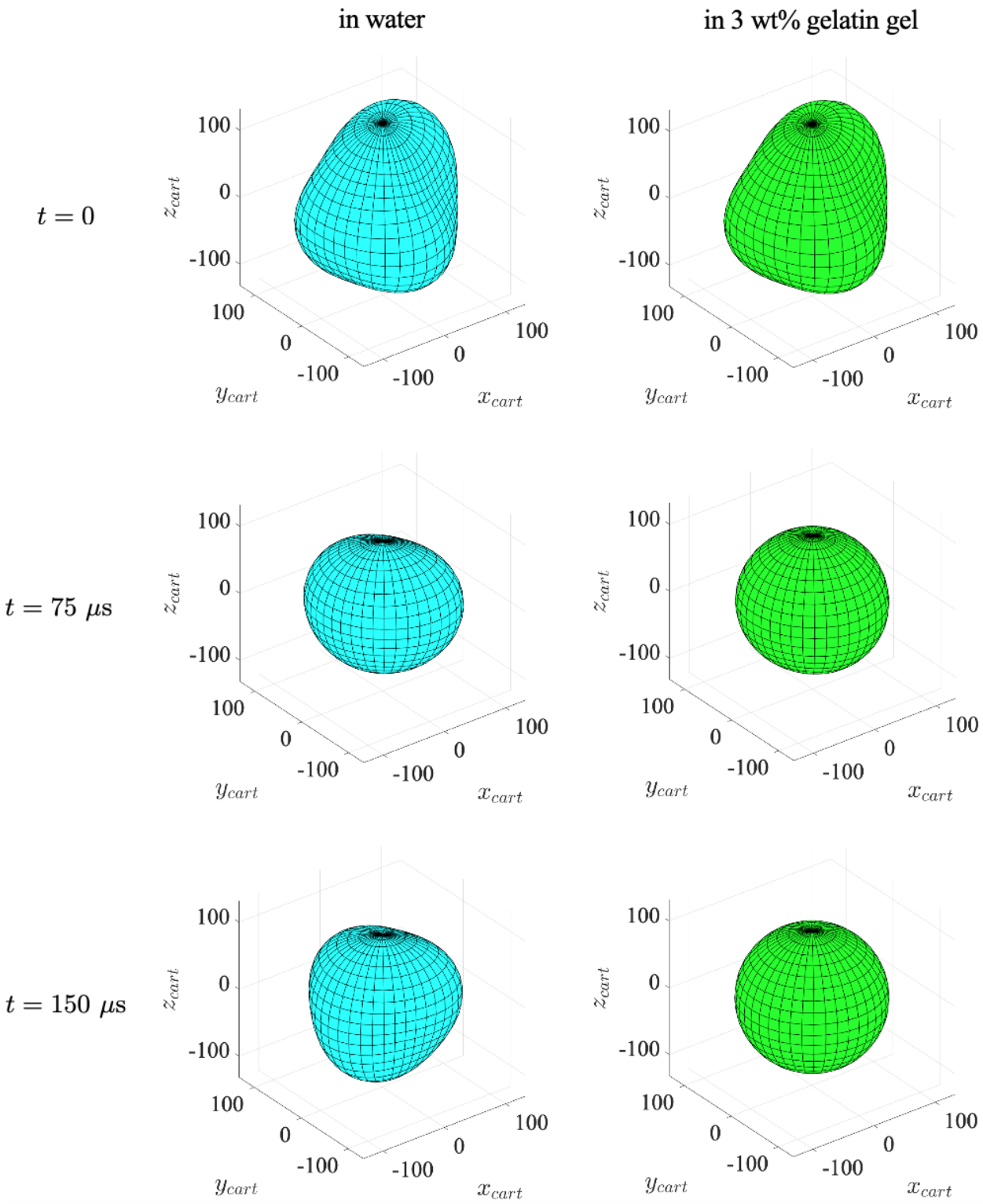

Figure 4.5: The shape of non-spherical bubbles at different times in water (cyan bubble) and in the gel (green bubble), corresponding to figure 4.4. The bubble in the gel quickly converges to a spherical shape, while the bubble in water continues non-spherical oscillations. In water, mode $n = 2$ is dominant at $t = 75\ \mu$s and mode $n = 3$ is dominant at $t = 150\ \mu$s.

CHAPTER 5

Shape Stability of a Bubble in Soft Matter

This chapter is adapted from Murakami *et al.* (2020a).

5.1 Introduction

We study the shape stability of a bubble in soft matter using the non-spherical model developed in chapter 4. Predicting the onset of bubble shape instability is a fundamental problem for therapeutic ultrasound applications (Brennen, 2015). Parametric instability is caused by the parametric resonance between the mean bubble radius and the non-spherical perturbation, which occurs when $\omega_d = 2\omega_n$ where $\omega_d = 2\pi f_d$ is the driving frequency and ω_n is the natural frequency of the non-spherical mode n (Versluis *et al.*, 2010). We observed the parametric instability of mode $n = 1$ in the 6 wt% gelatin gel in chapter 2, though the natural frequency of the non-spherical mode in soft matter has not been identified at this point. Inertial Microcavitation high strain-rate Rheometry (IMR) (Estrada *et al.*, 2018) requires to ensure that the bubble maintains its spherical shape during the laser-induced collapse in soft materials. As shown in figure 1.2 in chapter 1, experiments usually cannot capture the bubble at its minimum size during the first inertial collapse because of the limited resolutions of high-speed cameras, thus we need to rely on an analytical approach to investigate the bubble behavior between the two snapshots in the experiments. During inertial bubble collapse, a Rayleigh–Taylor-type instability of the bubble surface may be induced by the large acceleration (Brennen, 2002). This chapter studies the two types of instability, which have been investigated for bubbles in water, but not in soft matter:

- Parametric instability during ultrasound-induced bubble oscillations
- Rayleigh–Taylor-type instability during inertial bubble collapse

Some analytical studies are feasible for the parametric instability, while the Rayleigh–Taylor-type instability is investigated by numerically solving the non-spherical model.

We first introduce the damping rate and natural frequency of the non-spherical perturbation through the problem of parametric instability. In particular, the natural frequency is important as it determines the most unstable mode in the parametric instability. Furthermore, our non-spherical model reduces to a Mathieu equation which provides the amplitude threshold to predict the parametric instability. Although we do not conduct any convergence studies, these predictions of the most unstable mode serve a verification role. Our non-spherical analysis is validated against the two experimental data of parametric instability: one is mode $n = 3$ oscillations in a 3 wt% gelatin gel observed by Hamaguchi & Ando (2015), and the other is mode $n = 1$ oscillations in a 6 wt% gelatin gel observed in chapter 2. After the non-spherical model is validated for parametric instability, we numerically study the Rayleigh–Taylor-type instability during laser-induced inertial collapse. We investigate how the viscoelasticity as well as the initial perturbation amplitude influence the occurrence of the Rayleigh–Taylor-type instability.

5.2 Parametric instability

5.2.1 Damping rate

We first investigate the role of viscosity on non-spherical perturbation growth due to parametric instability. In addition, we explain the contributions of rotational and irrotational fields to the damping rate. We consider a bubble with the equilibrium mean radius $R_{eq} = 100$ μm in water, driven by ultrasound with frequency $f_d = 28$ kHz and pressure amplitude $p_A = \max(p_a) = 3.5$ kPa, where $p_a(t)$ is the acoustic pressure. The far-field pressure is $p_\infty(t) = p_{atm} + p_a(t)$ and the bubble pressure $p_b(t)$ is given by the pure gas model (see chapter 2). The initial conditions are given as

follows: mean bubble radius $R(t = 0) = R_{eq}$, $\dot{R}(t = 0) = 0$, perturbation amplitude[1] $a_n(t = 0) = 0.01R_{eq}$, $\dot{a}_n(t = 0) = 0$, bubble pressure $p_b(t = 0) = p_{atm} + 2\sigma/R_{eq}$, temperature field inside the bubble $T(r, t = 0) = T_\infty$ and toroidal field outside the bubble $\mathcal{T}(r, t = 0) = 0$. The physical properties of water is listed in table 4.1 in chapter 4.

Numerical solutions of the non-spherical model (4.22) and (4.37) are shown in figure 5.1, including the ultrasound pressure, mean bubble radius and perturbation amplitudes ($n = 2$ to $n = 6$) normalized by the mean bubble radius. Mode $n = 4$ gradually grows because of the parametric instability, as explained in detail in sections 5.2.2 and 5.2.3. In order to evaluate the contributions of the rotational field, we compare the solutions of mode $n = 4$ with different computational domain sizes: the irrotational model, $y_\infty = 1$ (the integral terms are zero), $y_\infty = 2$ and $y_\infty = 3$, as shown in figure 5.2. The full model exhibits smaller growth than the irrotational model. This behavior follows from the damping due to viscous dissipation at the bubble surface. Substituting the shear stress continuity condition (4.35) into $C_{n_{rot}}$ (4.42), the damping rate is obtained from equation (4.37) as

$$\zeta_n = 2(n + 1)(n + 2)\frac{\mu}{\rho_\infty R^2} + \zeta_{n_{rot}}, \tag{5.1}$$

with rotational correction

$$\zeta_{n_{rot}} = 2n(n + 2)\frac{\mu}{\rho_\infty R^2}, \tag{5.2}$$

which indicates that the rotational field increases the damping rate by satisfying the shear stress continuity at the bubble surface.

A comparison between solutions with $y_\infty = 1$ and $y_\infty = 2$ in figure 5.2 shows that the vorticity field (integral terms) has a destabilizing effect on the bubble surface. However, this contribution is small and the converged solution still exhibits much smaller growth than the irrotational model.

[1]The bubble with 1% perturbation is quite spherical. As a reference, the bubble in gel at $t = 75$ μs in figure 4.5 in chapter 4 has 1.9% perturbation of mode $n = 2$.

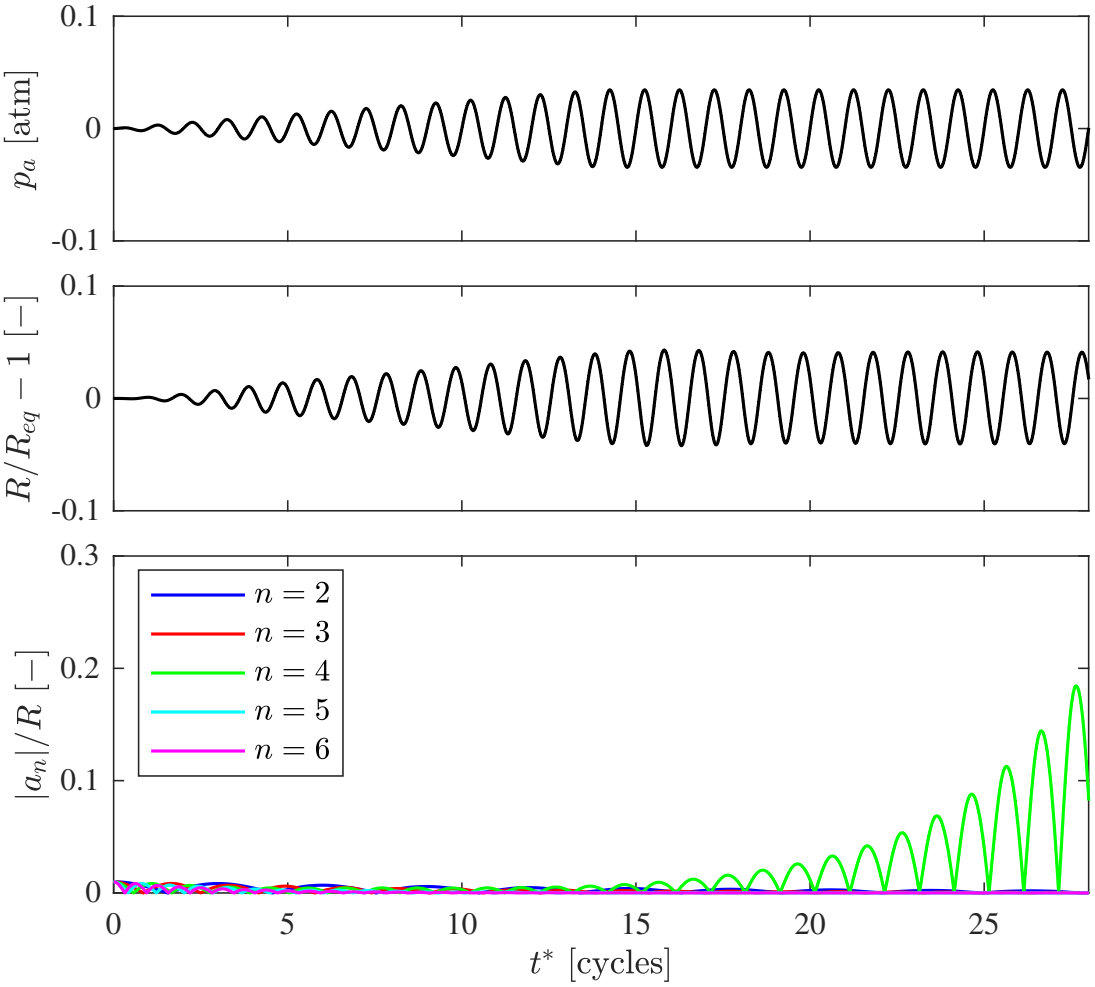

Figure 5.1: Solutions of the non-spherical model for a bubble with $R_{eq} = 100\ \mu$m in water driven by 28 kHz ultrasound, leading to the parametric instability of mode $n = 4$. Time histories of ultrasound pressure (top), mean bubble radius (middle) and perturbation amplitudes (bottom).

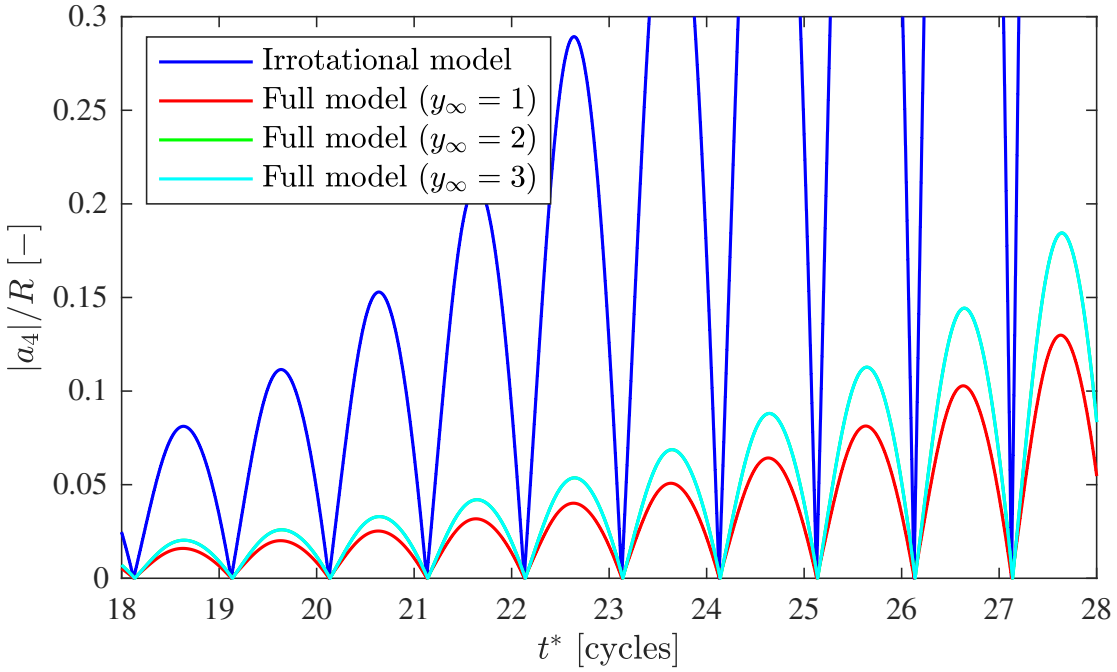

Figure 5.2: Comparison of the mode $n = 4$ in figure 5.1 with different computational domain sizes: the irrotational model, $y_\infty = 1$ (the integral terms are zero), $y_\infty = 2$ and $y_\infty = 3$. The solution with $y_\infty = 3$ is indistinguishable from that with $y_\infty = 2$. The full model taking into account the rotational field exhibits smaller growth than the irrotational model.

The solution appears to be converged with relatively small domain size[2] $y_\infty = 2$, thus the boundary layer tends to have a finite size, which is thin compared to the mean bubble radius. This behavior is expected given that the interface oscillations give rise to a problem analogous to Stokes' second problem (e.g., Currie, 2013, pp. 269-272). In fact, the main contribution of the rotational field originates from shear stress continuity at the bubble surface rather than the rotational field itself in the surroundings.

5.2.2 Natural frequency and the most unstable mode

We next investigate the role of elasticity, which is important because the natural frequency of the non-spherical modes determine the most unstable mode in parametric instability. Considering an initially spherical oscillating bubble, it is reasonable to assume $\mathcal{T}(r \neq R, t) = 0$ as long as no

[2]We use the number of mesh $N_{y_{out}} = 200$ for the case with $y_\infty = 2$ and $N_{y_{out}} = 800$ for the case with $y_\infty = 3$, thus figure 5.2 shows that the resolution as well as computational domain size are enough to capture the toroidal field.

vorticity is present around the bubble before the non-spherical perturbation appears. Substituting the shear stress continuity condition (4.35) into $C_{n_{rot}}$ (4.42) yields

$$C_{n_{rot}} \approx 2n(n+2)^2 \frac{\mu}{\rho_\infty R^2}\dot{a}_n - 2n(n-1)(n+2)\frac{\mu\dot{R}}{\rho_\infty R^3}a_n + n(n+1)(n+2)\frac{G}{\rho_\infty R^2}\left(\frac{R_{eq}}{R}\right)^4 a_n. \quad (5.3)$$

Then, the non-spherical model (4.37) reduces to

$$\ddot{a}_n + (A_n + A'_{n_{rot}})\dot{a}_n + (B_n + B'_{n_{rot}})a_n = 0, \quad (5.4)$$

where

$$A'_{n_{rot}} = 2n(n+2)\frac{\mu}{\rho_\infty R^2}, \quad (5.5)$$

$$B'_{n_{rot}} = -2n(n-1)\frac{\mu\dot{R}}{\rho_\infty R^3} + n(n+1)\frac{G}{\rho R^2}\left(\frac{R_{eq}}{R}\right)^4. \quad (5.6)$$

Since this is a second-order linear Ordinary Differential Equation (ODE), the square of its natural frequency corresponds to $B_n + B'_{n_{rot}}$. Ignoring the transient variation in the base state $R(t)$, the natural frequency of the non-spherical mode n is obtained as

$$\omega_n^2 = (n-1)(n+1)(n+2)\frac{\sigma}{\rho_\infty R_{eq}^3} + (n+1)\frac{G}{\rho_\infty R_{eq}^2}\left[4 + \frac{n(n+1)}{3}\right] + \omega_{n_{rot}}^2, \quad (5.7)$$

with rotational correction

$$\omega_{n_{rot}}^2 = n(n+1)\frac{G}{\rho_\infty R_{eq}^2}, \quad (5.8)$$

which indicates that the shear modulus of the surrounding medium increases the natural frequency of the non-spherical mode. This behavior is consistent with the notion that an elastic force has a restoring effect. Equation (5.7) also implies that the shear modulus of the surrounding medium enables parametric instability of mode $n = 1$, which does not exist in water because translational

oscillations cannot be induced by surface tension only. An elastic membrane on an encapsulated bubble also cannot induce the translational oscillations (Liu *et al.*, 2012). When $G = 0$, equation (5.7) reduces to the natural frequency of the non-spherical mode in water (Lamb, 1932; Prosperetti, 1977b). Similar to the damping rate (5.1), the rotational correction $\omega_{n_{rot}}^2$ stems from satisfying shear stress continuity at the bubble surface.

For a fixed driving frequency, equation (5.7) relates the most unstable mode number n to the equilibrium bubble radius R_{eq} as an indication of parametric instability, which occurs when $\omega_d = 2\omega_n$. Figure 5.3 shows this relation for $f_d = 28$ kHz in water and in the 3 wt% gelatin gel (see table 4.2 in chapter 4), where the surface tension $\sigma = 0.040$ N/m and shear modulus $G = 1.7$ kPa of the gel are taken from the experiments of Hamaguchi & Ando (2015). For example, mode $n = 4$ is the most unstable for a bubble with $R_{eq} = 100\,\mu$m in water, which is exactly what we observed in figure 5.1. While the most unstable mode is determined only by surface tension in water, it varies depending on the shear modulus in soft matter. For a given bubble size, shear modulus reduces the most unstable mode number n to a value below that of water. The rotational correction slightly changes the most unstable mode from that predicted by the irrotational model.

5.2.3 Mathieu equation and amplitude threshold

We can find the amplitude threshold of radial motion for the parametric instability by reducing the non-spherical model (4.37) to a Mathieu equation. Francescutto & Nabergoj (1978) reduced the purely viscous model of Prosperetti (1977b) to a Mathieu equation and found that the parametric instability occurs when the mean bubble radius $R(t)$ exceeds a threshold value. Following a similar procedure, we derive the amplitude threshold for the parametric instability in soft matter. We introduce the change of variables:

$$a_n = b_n \exp\left[-\frac{1}{2}\int (A_n + A'_{n_{rot}})dt\right], \tag{5.9}$$

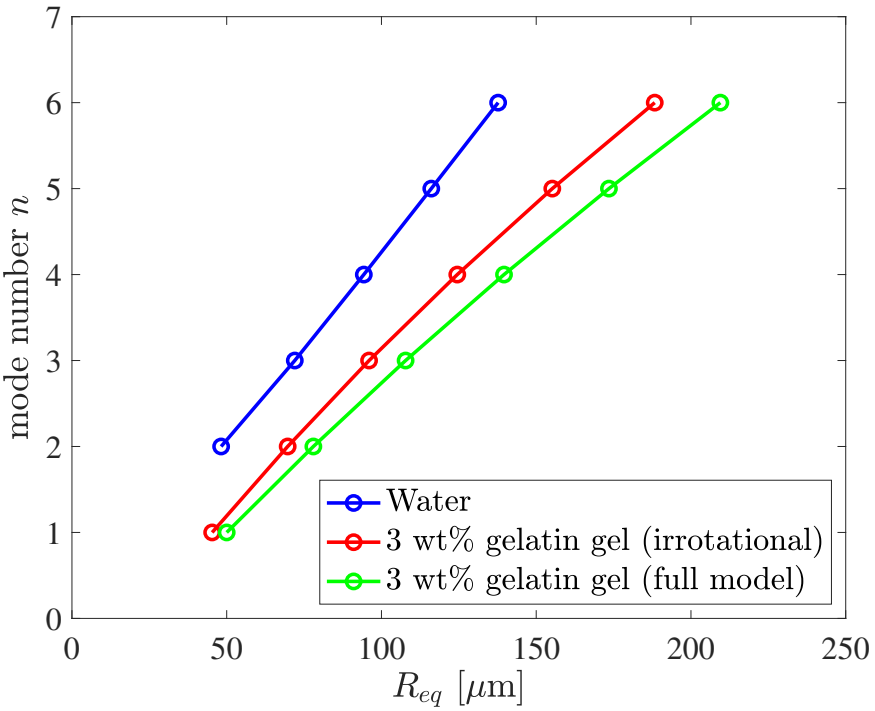

Figure 5.3: The most unstable mode versus equilibrium bubble radius in parametric instability in water and in the 3 wt% gelatin gel for a driving frequency f_d = 28 kHz. The shear modulus of the 3 wt% gelatin gel is G = 1.7 kPa.

such that equation (5.4) is transformed to

$$\ddot{b}_n - (\mathcal{G}_n + \mathcal{G}_{n_{rot}})b_n = 0, \tag{5.10}$$

where

$$\begin{aligned}
\mathcal{G}_n &= \frac{3}{4}\left(\frac{\dot{R}}{R}\right)^2 + \left(n+\frac{1}{2}\right)\frac{\ddot{R}}{R} - (n-1)(n+1)(n+2)\frac{\sigma}{\rho R^3} \\
&\quad - 6n(n+1)\frac{\mu\dot{R}}{\rho_\infty R^3} + \left[(n+1)(n+2)\frac{\mu}{\rho_\infty R^2}\right]^2 \\
&\quad - (n+1)\frac{G}{\rho_\infty R^2}\left[2\frac{R_{eq}}{R} + 2\left(\frac{R_{eq}}{R}\right)^4 + \frac{n(n+1)}{1+\frac{R_{eq}}{R}+\left(\frac{R_{eq}}{R}\right)^2}\right], \qquad (5.11) \\
\mathcal{G}_{n_{rot}} &= -6n\frac{\mu\dot{R}}{\rho_\infty R^3} + 2n(n+1)(n+2)^2\left(\frac{\mu}{\rho_\infty R^2}\right)^2 + \left[n(n+2)\frac{\mu}{\rho_\infty R^2}\right]^2 \\
&\quad - n(n+1)\frac{G}{\rho_\infty R^2}\left(\frac{R_{eq}}{R}\right)^4. \qquad (5.12)
\end{aligned}$$

Considering that the radial motion driven by ultrasound is simple harmonic,

$$R = R_{eq}(1 + C\cos\omega_d t), \tag{5.13}$$

where the oscillation amplitude $C = R/R_{eq} - 1$ is of order $O(|a_n|/R)$. Substituting equation (5.13) into equation (5.10) and using the change of variables $z = \omega_d t/2$, a Mathieu equation is obtained to order $O(a_n)$,

$$\frac{d^2 b_n}{dz^2} + \left[\beta_0 + 2\beta_2\cos(2z - \phi_m)\right] b_n = 0, \tag{5.14}$$

where

$$\beta_0 = \alpha_1 - (\alpha_2 + \alpha_{2_{rot}})^2 + \alpha_3\left[4 + \frac{n(n+1)}{3}\right] + \alpha_{3_{rot}}, \tag{5.15}$$

$$\beta_2 = C\sqrt{X_m^2 + Y_m^2}, \tag{5.16}$$

$$\phi_m = \arctan\frac{Y_m}{X_m}, \tag{5.17}$$

and

$$X_m = (2n+1) - \frac{3}{2}\alpha_1 + 2(\alpha_2 + \alpha_{2_{rot}})^2 - \alpha_3\left[18 + \frac{n(n+1)}{3}\right] - 6\alpha_{3_{rot}}, \tag{5.18}$$

$$Y_m = \alpha_4 + \alpha_{4_{rot}}, \tag{5.19}$$

$$\alpha_1 = 4(n-1)(n+1)(n+2)\frac{\sigma}{\rho_\infty \omega_d^2 R_{eq}^3}, \tag{5.20}$$

$$\alpha_2 = 2(n+1)(n+2)\frac{\mu}{\rho_\infty \omega_d R_{eq}^2}, \qquad \alpha_{2_{rot}} = 2n(n+2)\frac{\mu}{\rho_\infty \omega_d R_{eq}^2}, \tag{5.21}$$

$$\alpha_3 = 4(n+1)\frac{G}{\rho_\infty \omega_d^2 R_{eq}^2}, \qquad \alpha_{3_{rot}} = 4n(n+1)\frac{G}{\rho_\infty \omega_d^2 R_{eq}^2}, \tag{5.22}$$

$$\alpha_4 = -12n(n+1)\frac{\mu}{\rho_\infty \omega_d R_{eq}^2}, \qquad \alpha_{4_{rot}} = -12n\frac{\mu}{\rho_\infty \omega_d R_{eq}^2}. \tag{5.23}$$

We again distinguish rotational corrections from irrotational terms. According to stability theory for a Mathieu equation, the stability condition for the first unstable region is (Hayashi, 1964)

$$(\beta_0 - 1)^2 + 2(\beta_0 + 1)\delta^2 + \delta^4 > \beta_2^2, \tag{5.24}$$

where $2\delta = 2(\alpha_2 + \alpha_{2_{rot}})$ is the constant term in the series of $A_n + A'_{n_{rot}}$ in equation (5.4). The stability condition (5.24) results in

$$C < C_t = \sqrt{\frac{\left\{(\alpha_1 - 1) + \alpha_3\left[4 + \frac{n(n+1)}{3}\right] + \alpha_{3_{rot}}\right\}^2 + 4(\alpha_2 + \alpha_{2_{rot}})^2}{X^2 + Y^2}}, \tag{5.25}$$

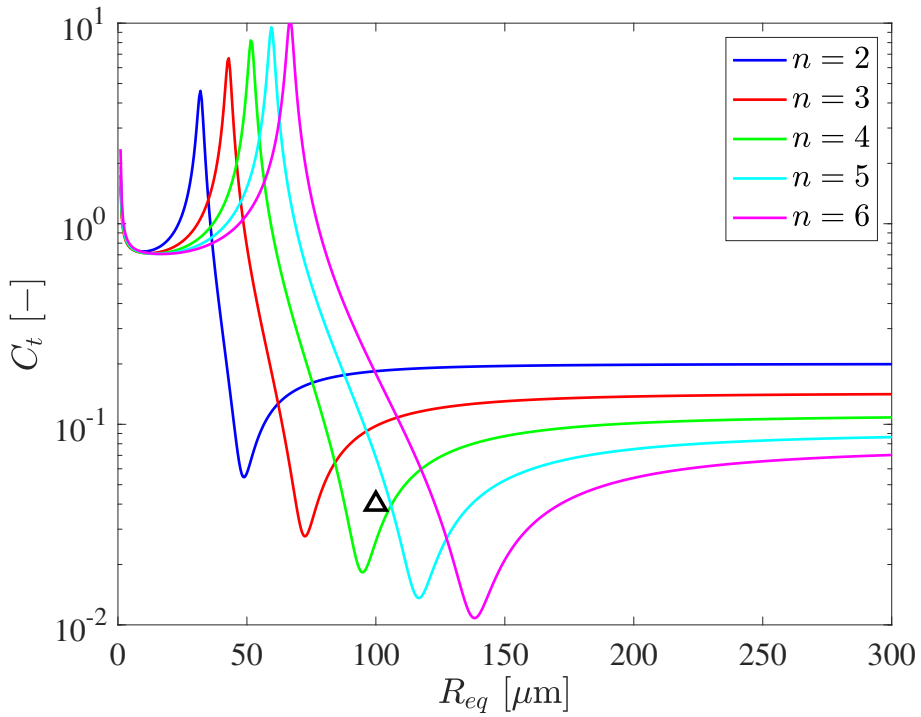

Figure 5.4: Amplitude threshold versus equilibrium bubble radius for parametric instability in water for a driving frequency $f_d = 28$ kHz. The triangle corresponds to the case in figure 5.1, which is inside the unstable region of mode $n = 4$.

where C_t is the amplitude threshold of radial motion. In short, parametric instability occurs when the radial motion exceeds the amplitude threshold: $C \geq C_t$.

The amplitude threshold C_t is determined by equation (5.25) for a given driving frequency ω_d, mode number n and equilibrium bubble radius R_{eq}. For a bubble in water, the amplitude thresholds for modes $n = 2$ to $n = 6$ are obtained for a fixed driving frequency $f_d = 28$ kHz as shown in figure 5.4. Each of these modes becomes unstable when the radial motion $C = R/R_{eq} - 1$ exceeds the corresponding amplitude threshold. For example, the radial motion in figure 5.1 is $C \approx 0.04$, which is shown by a triangle in figure 5.4. This triangle is inside the unstable region of mode $n = 4$ but outside the unstable regions of the other modes, thus confirming that mode $n = 4$ is the only unstable mode in this case. Furthermore, the minima of the amplitude thresholds in figure 5.4 and the most unstable modes in figure 5.3 correspond to the same equilibrium bubble radii. Higher modes $n > 6$ are stable, as their minima are located at larger equilibrium bubble radii.

We examine the difference between the amplitude thresholds of the full model and the irrotational model. Francescutto & Nabergoj (1978) compared the amplitude threshold with the experiments of Hullin (1977) in water, where the driving frequency was set to the natural frequency of the mean bubble radius (Plesset & Prosperetti, 1977):

$$\omega_0^2 = \frac{3\kappa}{\rho_\infty R_{eq}^2}\left(p_{atm} + \frac{2\sigma}{R_{eq}}\right) - \frac{2\sigma}{\rho_\infty R_{eq}^3}. \tag{5.26}$$

The polytropic index is set to $\kappa = 1.4$, which is valid for large bubbles (Chapman & Plesset, 1971). We reproduce the amplitude threshold of the full model for a bubble in water and compare to that of the irrotational model (equation (5.25) with no rotational correction) in figure 5.5. Since the second or third unstable regions provide additional minima (Hayashi, 1964), it is reasonable to define the amplitude threshold for all unstable regions as the line obtained by connecting the minima of the first unstable region as drawn in figure 5.5 (Francescutto & Nabergoj, 1978). The experimental data of Hullin (1977) are for the most part between lines following the full model (blue line, higher bound) and the irrotational model (red line, lower bound). This behavior is expected from figure 5.2 in which the solution of the full model lies between the solution with $y_{max} = 1.00$ (smallest growth) and the solution of the irrotational model (largest growth). Therefore, the precise threshold exists somewhere between the two models depending on how the vorticity behaves, and the irrotational model is useful as the lowest bound to secure from the parametric instability.

For a bubble in soft matter, the amplitude thresholds for modes $n = 1$ to $n = 5$ are obtained for a driving frequency $f_d = 28$ kHz as shown in figure 5.6, where the viscoelastic properties correspond to the 3 wt% gelatin gel (see table 4.2 in chapter 4) from the experiments of Hamaguchi & Ando (2015). Compared to the amplitude threshold in water in figure 5.4, viscoelasticity drastically changes the unstable region of the parametric instability. Viscosity smoothens the minima, while shear modulus shifts the minima toward larger equilibrium bubble radii. Hamaguchi & Ando (2015) observed that mode $n = 3$ is the most unstable mode for a bubble with $R_{eq} = 100\,\mu$m in the 3 wt% gelatin gel, which agrees with our prediction from the natural frequency (see figure 5.3).

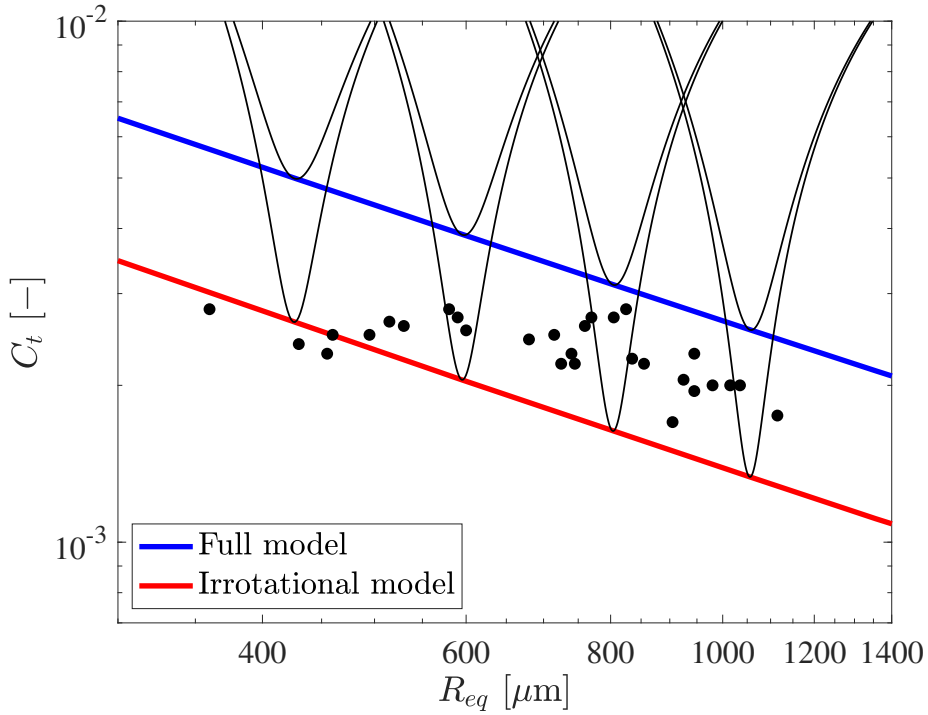

Figure 5.5: Comparison between the amplitude threshold and experiments in water, where the driving frequency is set to the natural frequency of the mean bubble radius. The minima of the amplitude thresholds correspond to modes $n = 8$ to $n = 11$ from left to right. The experimental data (black circles) are from Hullin (1977) and mostly bounded by lines following the full model (blue line, higher bound) and the irrotational model (red line, lower bound).

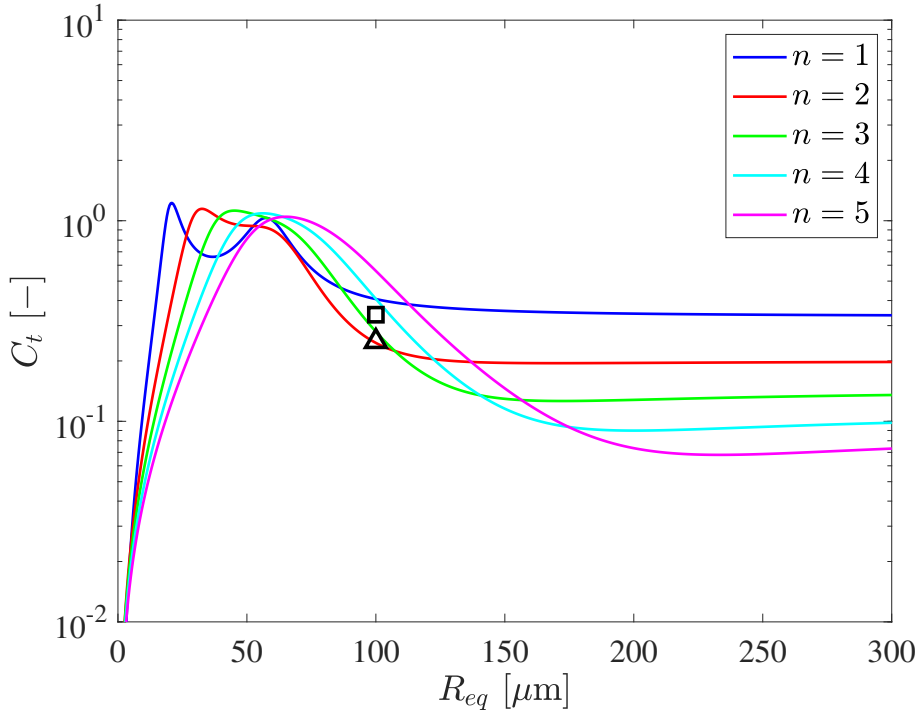

Figure 5.6: Amplitude threshold versus equilibrium bubble radius for the parametric instability in the 3 wt% gelatin gel for a driving frequency f_d = 28 kHz. The triangle and square correspond to the experiment of Hamaguchi & Ando (2015) and the example in figure 5.10, respectively, which are in the vicinity of the unstable regions of modes n = 2 and n = 3.

The radial motion in their experiments is $C \approx 0.25$, which is shown by a triangle in figure 5.6. This point is close to the unstable regions of modes $n = 2$ and $n = 3$, while it is clearly outside the unstable regions of the other modes. Thus, the amplitude threshold also implies parametric instability of mode $n = 3$.

5.2.4 Validation

We validate our non-spherical analysis against experimental observations of parametric instability in hydrogels. The parametric instability of mode $n = 3$ in the 3 wt% gelatin gel observed by Hamaguchi & Ando (2015) is well predicted by the natural frequency and amplitude threshold (see the last paragraph in section 5.2.3). In this section, we numerically solve the non-spherical model and investigate the parametric instability in the 3 wt% gelatin gel. We consider a bubble

with $R_{eq} = 100\,\mu$m driven by ultrasound with frequency $f_d = 28$ kHz and pressure amplitude[3] $p_A = 20.5$ kPa. Note that the pre-strain (see figure 2.4 in chapter 2) is small enough to be negligible in a 3 wt% gelatin gel (Ando & Shirota, 2019). The bubble pressure $p_b(t)$ is given by the pure gas model (see chapter 2). The initial conditions are set to $R(t = 0) = R_{eq}$, $\dot{R}(t = 0) = 0$, $a_n(t = 0) = 0.01R_{eq}$, $\dot{a}_n(t = 0) = 0$, $p_b(t = 0) = p_{atm} + 2\sigma/R_{eq}$, $T(r, t = 0) = T_\infty$ and $\mathcal{T}(r, t = 0) = 0$. The physical properties of the 3 wt% gelatin gel are listed in table 4.2 in chapter 4. The main uncertainty is the initial perturbation amplitudes, which are too small to resolve in experiments. Versluis *et al.* (2010) reported the initial condition $a_4 \approx 0.1\,\mu$m for $R_{eq} = 33\,\mu$m in water. We set a similar initial condition $a_n(t = 0) = 0.01R_{eq}$, though of course this value is likely to vary from one experiment to another.

Solutions of the non-spherical model including the ultrasound pressure, mean bubble radius and perturbation amplitudes ($n = 1$ to $n = 5$) normalized by the mean bubble radius are shown in figure 5.7. The perturbation amplitudes are initially small, such that the oscillations are effectively spherical. However, after several oscillations, mode $n = 3$ grows sufficiently due to the parametric instability, which causes the bubble shape to visibly depart from spherical (see figure 5.8), while the other non-spherical modes remain small. This behavior is predicted by the natural frequency and amplitude threshold (see figures 5.3 and 5.6). Figure 5.8 shows an example of the non-spherical bubble shape observed in our simulations at $t^* = 25.7$ and in the experiments of Hamaguchi & Ando (2015) at $t^* = 22.9$, where both yield the unstable mode $n = 3$. These bubbles are two-dimensional projections from the perpendicular to the zenith direction ($m = 0$), where the axis of symmetry coincides with the initial laser focusing direction in the experiments[4]. The discrepancy of the time at which mode $n = 3$ appears originates from the uncertainty in the initial perturbation amplitudes and the imperfect agreement in the mean bubble radius. In the experiments, the mean bubble oscillations are damped after non-spherical oscillations become manifest because the

[3]The exact data of ultrasound pressure used in Hamaguchi & Ando (2015) are not available, so we use something similar to reproduce the radial motion, as shown in figure 5.7. Our interest here is parametric instability induced by the radial motion.

[4]In water, the axis of symmetry coincides with the direction of gravity (Versluis *et al.*, 2010). For mode $n = 1$ oscillations in the 6 wt% gelatin gel (see figure 2.9 in chapter 2), the axis of symmetry coincides with the initial laser focusing direction, which is also the direction of gravity.

kinetic energy of the radial motion is transferred to the non-spherical mode and dissipated (Liu *et al.*, 2011). This kind of mode interaction is not captured in our linearized model.

Another set of experimental data to be compared with our analysis is the parametric instability of mode $n = 1$ in the 6 wt% gelatin gel observed in chapter 2. With regard to the 6 wt% gelatin gel in our experiments, we concluded that the viscoelastic properties fitted through the linear theory correspond to the damaged gel, and thus the resonance curve obtained with higher viscoelasticity shows better agreement (see figure 2.10 in chapter 2). Figure 5.9 shows the most unstable mode for $f_d = 28$ kHz in the damaged gel ($G = 4.0$ kPa) and in the gel before being damaged ($G = 8.0$ kPa). For a bubble with $R_{eq} = 107.8$ μm, mode $n = 1$ is the most unstable with the higher shear modulus, which agrees with our experimental observation. Therefore, this comparison supports the validity of the non-spherical model as well as our conclusion in chapter 2.

5.2.5 The role of viscoelasticity on parametric instability

We investigate the shape stability of a bubble driven by pulse-wave ultrasound to examine the role of viscoelasticity on the time evolution of the perturbation amplitude. We again consider the bubble with $R_{eq} = 100$ μm in the 3 wt% gelatin gel, and the initial conditions are set in the same manner as section 5.2.4. Solutions including the pulse-wave ultrasound pressure, mean bubble radius and perturbation amplitudes ($n = 1$ to $n = 5$) are shown in figure 5.10. Modes $n = 2$ and $n = 3$ grow, mode $n = 4$ slightly grows, while modes $n = 1$ and $n = 5$ decay exponentially. This behavior is consistent with the fact that the most unstable mode number is between 2 and 3 ($n = 2.7$ in figure 5.3). This behavior is further supported by the amplitude threshold: the radial motion is $C \approx 0.34$ and depicted by a square in figure 5.6, which lies inside the unstable regions of modes $n = 2$ and $n = 3$, close to the unstable region of mode $n = 4$, but outside the unstable regions of the other modes. After the passage of the pressure pulse, every mode decays, with the higher modes decaying faster than the lower modes, as expected from the increasing damping rate (5.1).

We examine the role of viscosity and shear modulus on the perturbation amplitude by comparing the mode $n = 3$ presented in figure 5.10 (green line) with solutions where the viscosity is

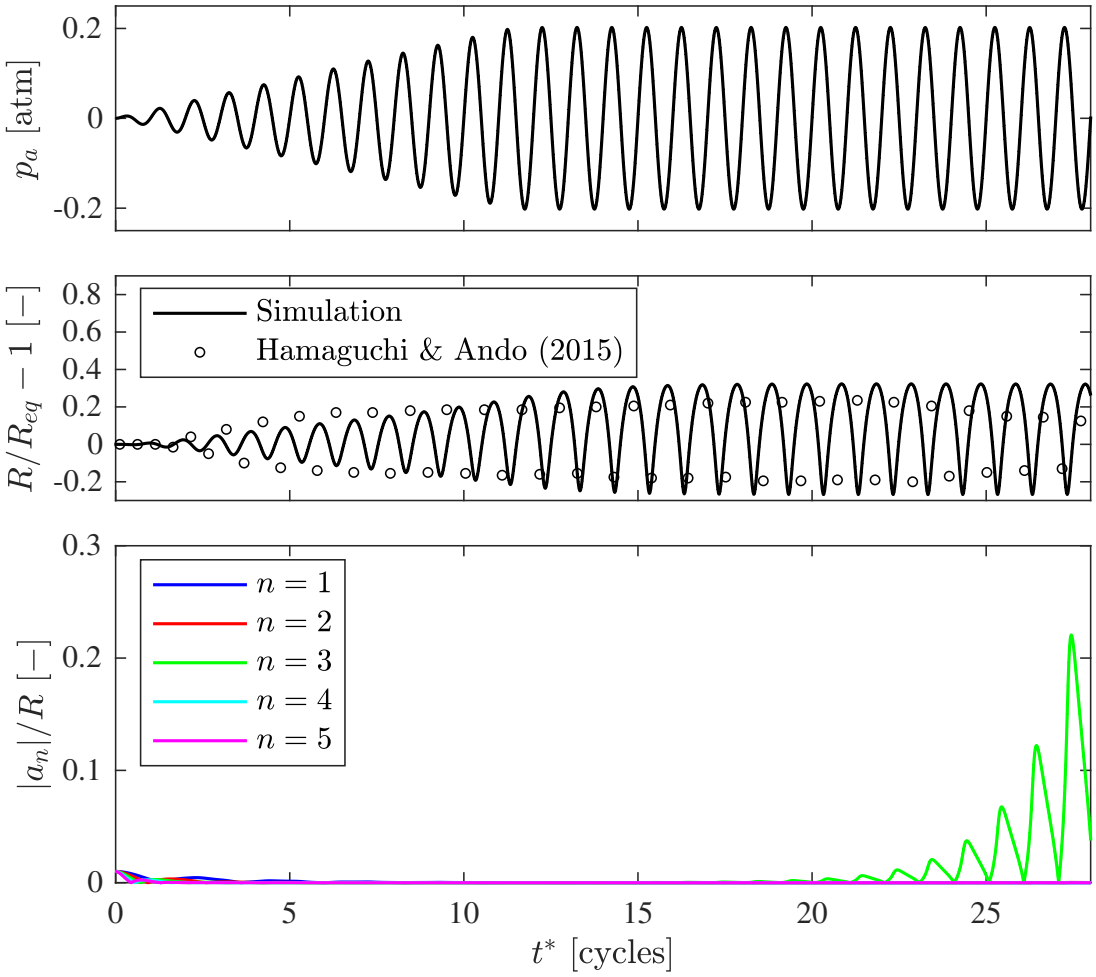

Figure 5.7: Solutions of the non-spherical model for a bubble with $R_{eq} = 100\,\mu$m in the 3 wt% gelatin gel driven by 28 kHz ultrasound, leading to the parametric instability of mode $n = 3$. Time histories of ultrasound pressure (top), mean bubble radius compared to the experiments of (Hamaguchi & Ando, 2015) (middle) and perturbation amplitudes (bottom).

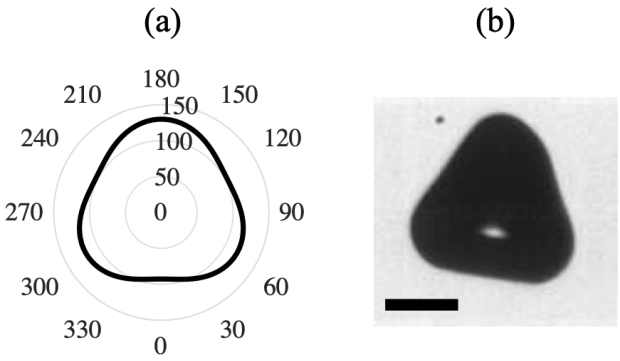

Figure 5.8: An example of the non-spherical bubble shape showing the mode $n = 3$. (a) The bubble obtained from our simulations at $t^* = 25.7$. (b) The bubble observed in the experiments of Hamaguchi & Ando (2015) at $t^* = 22.9$. The scale bar represents 100 μm.

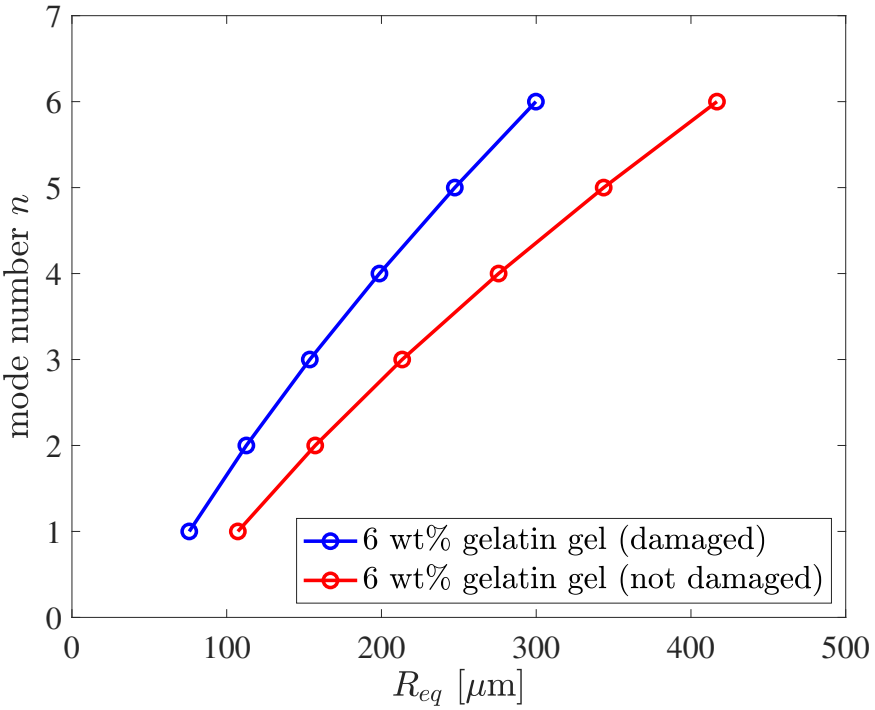

Figure 5.9: The most unstable mode versus equilibrium bubble radius in the parametric instability in the damaged 6 wt% gelatin gel ($G = 4.0$ kPa) and in the gel before being damaged ($G = 8.0$ kPa) for a driving frequency $f_d = 28$ kHz.

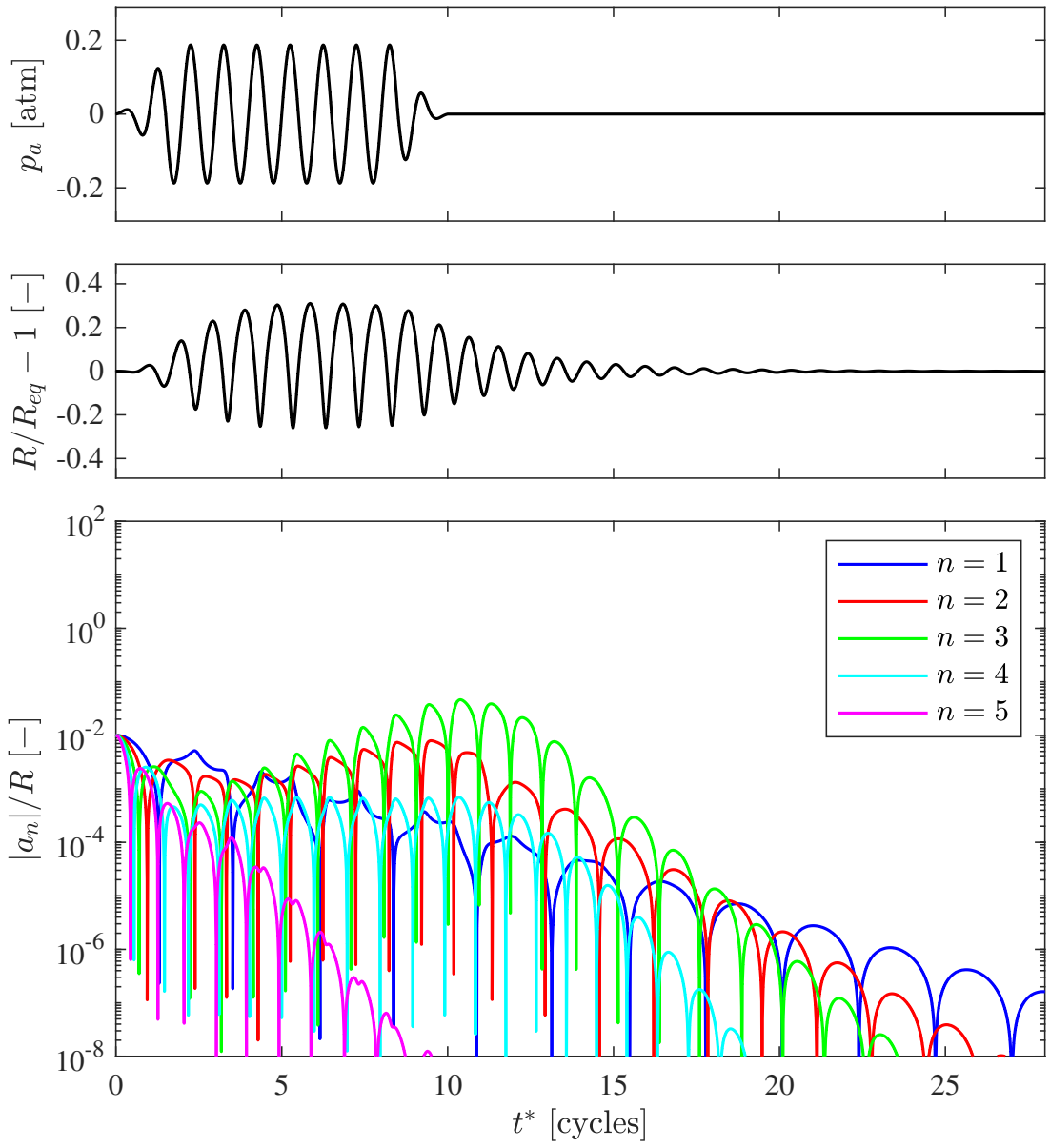

Figure 5.10: Solutions of the non-spherical model for a bubble with $R_{eq} = 100\,\mu$m in the 3 wt% gelatin gel driven by a pulse-wave ultrasound. Time histories of ultrasound pressure (top), mean bubble radius (middle) and perturbation amplitudes (bottom). Modes $n = 2$, $n = 3$ and $n = 4$ exponentially grow because of the parametric instability. After the passage of the pulse, higher modes decay faster than lower modes.

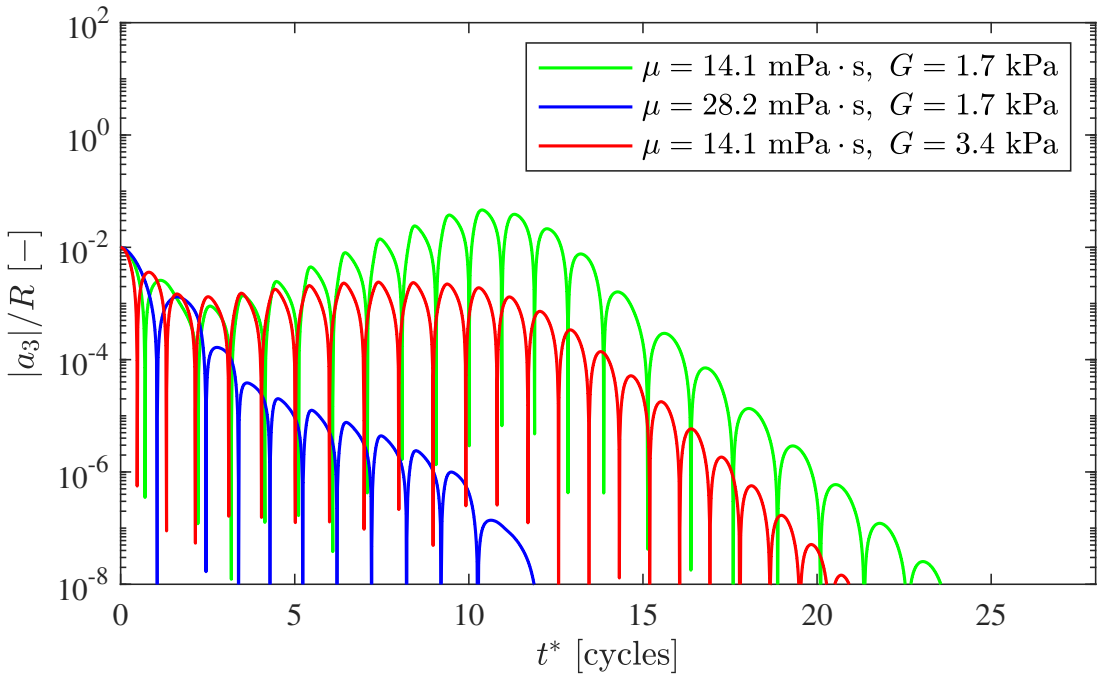

Figure 5.11: Comparison of the perturbation amplitude of mode $n = 3$ for three different cases: the same solutions as in figure 5.10, solutions with the same shear modulus but double the viscosity, and another with the same viscosity but double the shear modulus. Viscosity reduces the growth, while shear modulus changes the most unstable mode number to $n = 2$ for $G = 3.4$ kPa, thus making mode $n = 3$ less unstable.

doubled (but shear modulus kept the same) and another where the shear modulus is doubled (but the viscosity kept the same), as shown in figure 5.11. The mean bubble radius is slightly different in each case, but this discrepancy has only a small influence on the perturbation amplitude in this example. Viscosity increases the damping rate (5.1), thus reducing the perturbation growth and increasing the decay rate (blue line). Shear modulus increases the natural frequency of the non-spherical mode (5.7), where the most unstable mode number becomes $n = 2$ for $G = 3.4$ kPa, thus making mode $n = 3$ less unstable (red line).

5.3 Rayleigh–Taylor-type instability

Finally, we investigate the Rayleigh–Taylor-type instability that occurs during inertial bubble collapse. We consider the same problem of laser-induced bubble collapse in a soft polyacrylamide

gel as in chapter 3. Since the bubble dynamics have strong nonlinearity, we use the Keller–Miksis equation (2.5) rather than equation (4.22) to obtain the appropriate evolution of mean bubble radius $R(t)$, and solve the (incompressible) non-spherical model to examine the behavior of the perturbation $a_n(t)$. Compressible effects on the perturbation are expected to be small because the Mach number for the perturbation $\dot{a}_n/c_\infty$ is small at the initial stage of the instability[5]. The far-field pressure is $p_\infty(t) = p_{atm}$, and the bubble pressure $p_b(t)$ is given by the gas-vapor model (see chapter 3). Our goal is to confirm the spherical shape of a bubble in IMR, thus we use the irrotational model which always considers the lowest bound of the instability (see section 5.2.3). The initial conditions are set to $R(t = 0) = R_{max} = 350\,\mu$m, $\dot{R}(t = 0) = 0$, $a_n(t = 0) = 0.001R_{max}$, $\dot{a}_n(t = 0) = 0$, $p_b(t = 0)$ given by equation (3.36), $T(r, t = 0) = T_\infty$ and $k(r, t = 0)$ given by equation (3.17). The physical properties of the soft polyacrylamide gel are listed in table 3.4 in chapter 3. Again, the initial perturbation amplitudes are uncertainties in this problem.

Solutions of the mean bubble radius and perturbation amplitudes ($n = 1$ to $n = 10$) normalized by the mean bubble radius are shown in figure 5.12. The perturbations grow the largest during the first strongest collapse. Since the time scale of this instability is too small, we enlarge the first collapse in figure 5.13, in which we add the time history of bubble wall acceleration $\ddot{R}(t)$. During the inertial collapse, the bubble wall acceleration reaches the smallest value $\ddot{R} = -3.5 \times 10^9$ m/s^2 and sharply increases to $\ddot{R} = 3.7 \times 10^{10}$ m/s^2 within just 0.03 μs to make the bubble rebound. The instability is induced by this large acceleration of the gel into the gas and vice versa, thus this is the Rayleigh–Taylor-type instability. The most unstable mode is $n = 3$, and mode $n = 5$, $n = 6$ and $n = 4$ follow, thus the lower modes are relatively unstable.

We examine how viscoelasticity and initial perturbation amplitude influence the Rayleigh–Taylor-type instability of a bubble. Figure 5.14 compares the solutions of mode $n = 3$ presented in figure 5.13 (green line) to the solutions with double the viscosity, another with double the shear modulus, and another with half the initial perturbation amplitude. Viscoelasticity changes the evolution of mean bubble radius and thus the bubble wall acceleration, which is the most dominant

[5]The maximum perturbation velocity normalized by the sound speed in figure 5.12 is $\max|\dot{a}_3/c_\infty| = 0.10$.

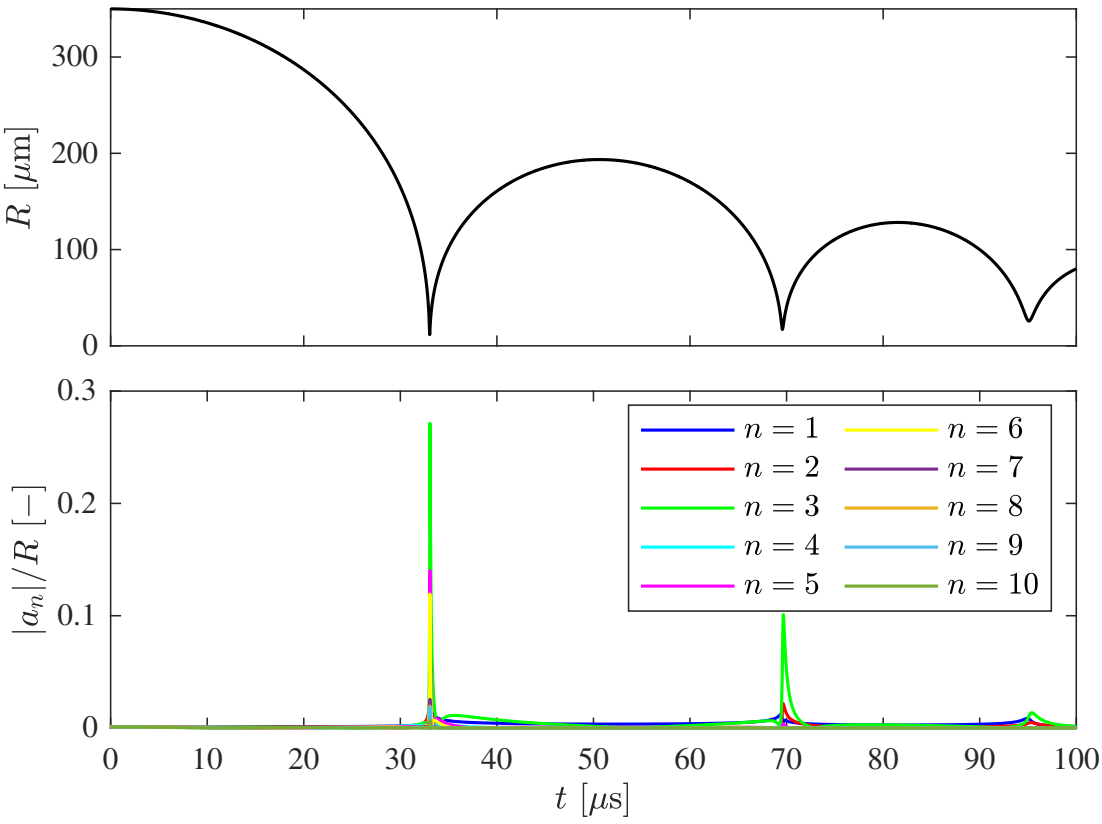

Figure 5.12: Solutions of the non-spherical model for laser-induced inertial collapse of an air-vapor bubble in a soft polyacrylamide gel. Time histories of mean bubble radius (top) and perturbation amplitudes (bottom). The perturbations grow the largest during the first strongest collapse.

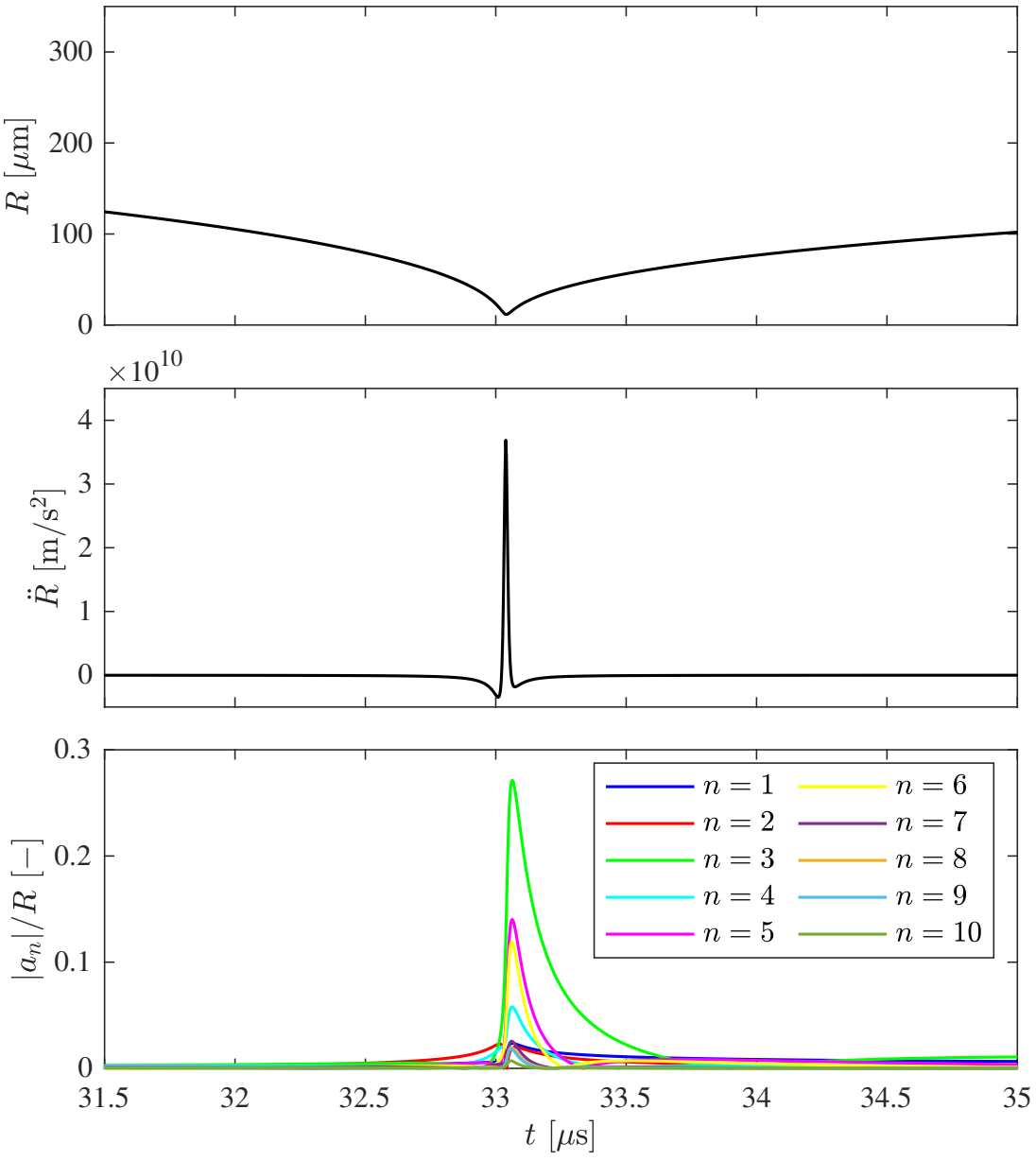

Figure 5.13: Enlarged view of figure 5.12 focusing on the first collapse, which shows the Rayleigh–Taylor-type instability. Time histories of mean bubble radius (top), bubble wall acceleration (middle) and perturbation amplitudes (bottom). The large acceleration induces the instability, where mode $n = 3$ is the most unstable in this case.

factor to induce the Rayleigh–Taylor-type instability. The bubble collapses at a later time for the case with double the viscosity as the acceleration is reduced, such that the perturbation growth is also reduced (blue line). On the other hand, the bubble collapses at an earlier time for the case with double the shear modulus as the acceleration is larger, which enhances the instability (red line). With half the initial perturbation amplitude (but with the same viscoelastic properties), the evolution of the mean bubble radius does not change, and the maximum perturbation amplitude simply becomes the half (cyan line). In short, the bubble wall acceleration, which is driven by the stretch ratio R_{max}/R_{eq} and viscoelasticity of the gel, and the initial perturbation amplitude are the key factors to determine if the bubble can retain its spherical shape during the inertial collapse.

5.4 Conclusions

We study two types of shape instability of a bubble in soft matter: one is the parametric instability during ultrasound-induced bubble oscillations, and the other is the Rayleigh–Taylor-type instability during inertial bubble collapse. Viscoelasticity plays an important role on the shape stability: viscosity increases the damping rate, thus suppressing the shape instability, while shear modulus increases the natural frequency, which changes the unstable mode in the parametric instability. Our non-spherical model reduces to a Mathieu equation and the amplitude threshold of radial motion is determined for parametric instability. Furthermore, our non-spherical analysis is validated against the experimental observations of parametric instability of mode $n = 3$ in the 3 wt% gelatin gel of Hamaguchi & Ando (2015) and mode $n = 1$ in the 6 wt% gelatin gel in chapter 2. For the Rayleigh–Taylor-type instability, viscoelasticity changes the bubble wall acceleration, which is the most dominant factor to induce the instability, while the initial perturbation amplitude simply scales the perturbation growth.

Given the ultrasound waveform, bubble size and physical properties of the soft matter, the natural frequency and Mathieu equation obtained in this chapter can be used to predict the unstable modes in parametric instability. This would help us to predict the bubble break up or the bubble

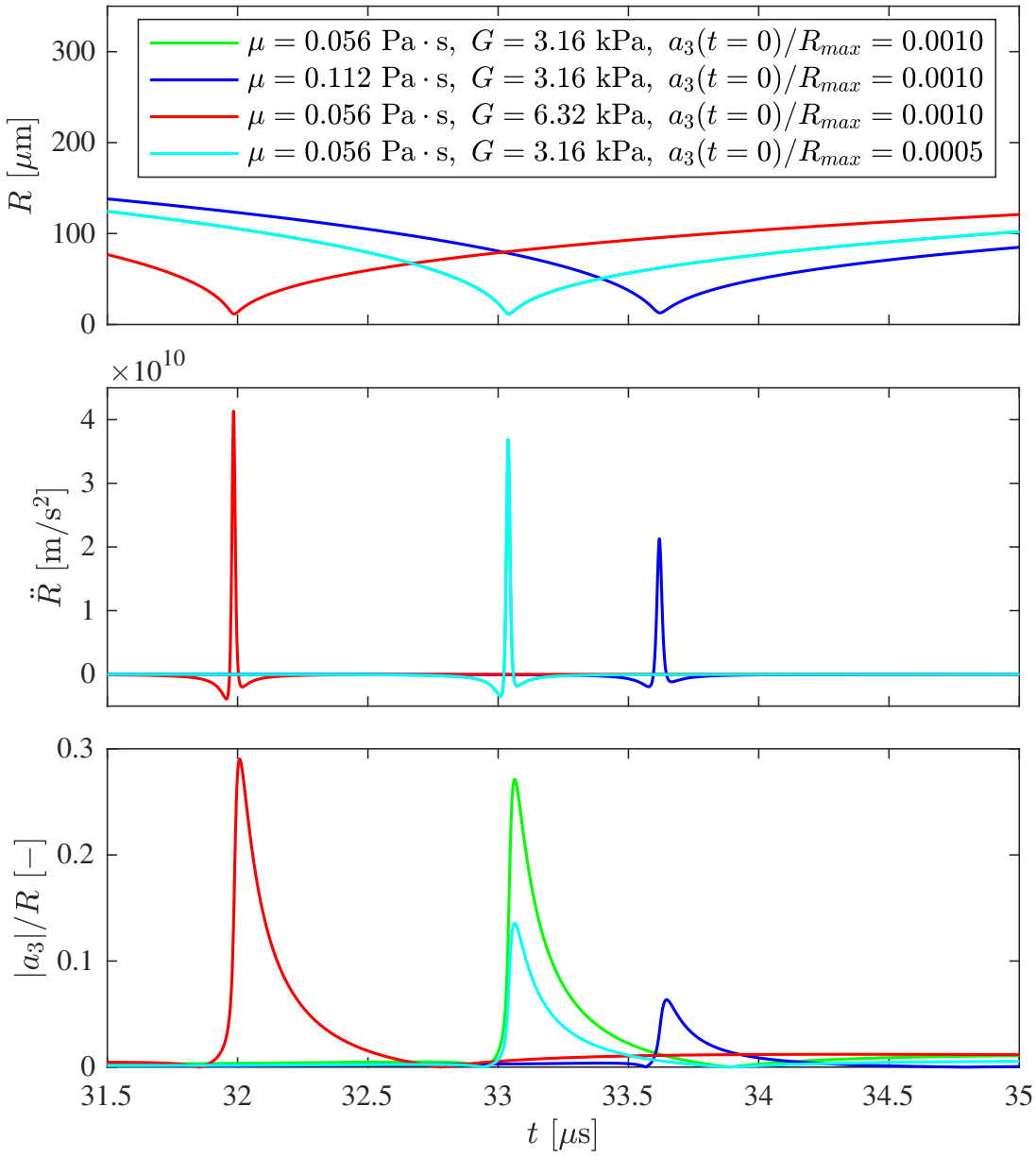

Figure 5.14: Comparison of the mode $n = 3$ in four different cases: the same solutions as in figure 5.13, solutions with double the viscosity, another with double the shear modulus, and another with half the initial perturbation amplitude. Viscoelasticity changes the bubble wall acceleration, which is the most dominant factor to induce the perturbation growth. The initial perturbation amplitude simply scales the growth.

collapse pressure produced by the damped mean bubble oscillations in therapeutic ultrasound. Furthermore, this analysis could be used to measure viscoelastic properties of soft materials at high rates by experimentally observing the decay rate and unstable mode of the non-spherical bubble oscillations. The time scale of the Rayleigh–Taylor-type instability that may occur in situations relevant to IMR is less than 0.1 μs, which is challenging to capture in experiments. If the initial perturbation amplitude is resolved when the bubble is expanded to R_{max}, the non-spherical model can predict the occurrence of the Rayleigh–Taylor-type instability, which would be helpful for the use of IMR.

CHAPTER 6

Conclusions

6.1 Summary and conclusions

In this thesis, we conducted analytical studies of spherical and non-spherical bubble dynamics in soft matter. The analysis is based on continuum mechanics; new models for spherical and non-spherical bubble dynamics were developed from conservation laws. These models were solved numerically and compared with experiments, leading to the validation of the models and to predictions of the following problems: ultrasound-induced bubble dynamics in soft matter, the role of gas-vapor mixture transport on inertial collapse, and shape stability of a bubble in soft matter.

Ultrasound-induced nonlinear oscillations of a gas bubble in a 6 wt% air-supersaturated gelatin gel were experimentally and numerically studied to investigate the role of viscoelasticity on the bubble dynamics. Comparison of finite-amplitude oscillations between experiments and simulations showed good agreement, implying the validity of the Rayleigh–Plesset-type model coupled with the Kelvin–Voigt constitutive equation with neo-Hookean elasticity. A resonance curve of the finite-amplitude bubble oscillations was experimentally obtained, which confirms the nonlinear feature of spring softening. Comparison of the resonance curves between experiments and simulations indicated that our viscoelastic properties fitted through linear theory correspond to the gel which has been damaged by the repeated large-amplitude oscillations.

We developed a model for gas-vapor bubble dynamics and investigated the role of gas-vapor mixture transport on inertial collapse. The new model takes into account the different ratios of specific heats for the gas and vapor. Numerical solutions showed that a large amount of vapor

is trapped by an air shell during inertial collapse and thus the maximum temperature is induced near the bubble wall in the air-dominated region. Furthermore, the trapped vapor reduces the bubble collapse velocity and thus energy losses via acoustic radiation, leading to a larger bubble rebound. This analysis was validated against our experiments of laser-induced bubble collapse in 50 wt% glycerol. Comparison between the new and conventional models showed that the constant-γ assumption $\gamma = \gamma_g = \gamma_v$ results in experimentally measurable discrepancies of several percent.

Lastly, we studied shape stability of a bubble in soft matter. A model for non-spherical bubble dynamics in soft matter was developed by extending classical perturbation analysis to a spherical interface between a gas and a soft solid. Viscoelasticity plays an important role on shape stability: viscosity increases the damping rate, thus suppressing the instability, while shear modulus increases the natural frequency, which changes the unstable mode in the parametric instability. Our non-spherical model reduced to a Mathieu equation and the amplitude threshold of radial motion was obtained to predict the parametric instability. The analysis was validated against experimental observations of ultrasound-induced non-spherical oscillations of a bubble in gelatin gels. Rayleigh–Taylor-type instability during inertial bubble collapse was numerically investigated. Viscoelasticity influences the bubble wall acceleration, which is the most dominant factor to induce the Rayleigh–Taylor-type instability.

These new findings as well as models for spherical and non-spherical bubble dynamics in soft matter could benefit applications including Inertial Microcavitation high strain-rate Rheometry (IMR), blast Traumatic Brain Injury (TBI) and therapeutic ultrasound. The study of gas-vapor mixture transport can improve the theoretical-numerical cavitation model used in IMR to appropriately predict the laser-induced bubble collapse in soft materials. The analysis on the Rayleigh–Taylor-type instability could help us to ensure that the bubble maintains its spherical shape during the laser-induced collapse in IMR. The study of ultrasound-induced bubble dynamics is potentially useful to predict the bubble break up in ultrasound drug delivery or the bubble collapse pressure in tissue ablation. Furthermore, the analysis of parametric instability could be used to develop techniques to measure viscoelastic properties of soft materials at high rates by experimentally ob-

serving non-spherical bubble oscillations.

6.2 Suggestions for future work

6.2.1 Modeling of spherical bubble dynamics

The Rayleigh–Plesset-type model for spherical bubble dynamics satisfies the conservations laws of continuum mechanics under the following main assumptions: spherically symmetric, homobaric, cold liquid and weakly compressible assumptions. The model also assumes no chemical reaction, the ideal gas law and equilibrium phase change at the bubble interface. These assumptions may not apply to all cavitation problems.

In the case of laser-induced bubble collapse in soft materials in IMR, one of the important uncertainties is the composition of non-condensible gases inside the bubble, as well as the temperature and mass fraction fields after the initial laser-induced growth. Air only was considered in this thesis, while different non-condensible gases may exist inside laser-induced cavitation bubbles in soft materials. These non-condensible gases may further react under the high temperatures produced during the inertial collapse, which would require incorporating chemical reactions into the model.

With regard to the viscoelastic modeling, the Kelvin–Voigt constitutive equation with neo-Hookean elasticity is validated for some tissue-mimicking hydrogels, and different constitutive equations are also available if needed, including relaxation (Warnez & Johnsen, 2015; Estrada *et al.*, 2018) and strain stiffening (Yang *et al.*, 2020). In addition, soft materials are sometimes damaged by the large-amplitude bubble oscillations, for which a description of damage or fracture (Movahed *et al.*, 2016) may be needed.

If the bubble dynamics include complicated reactions (Kamath *et al.*, 1993; Yasui *et al.*, 2004) or non-equilibrium phase change (Fujikawa & Akamatsu, 1980; Prosperetti, 2017) with many uncertain parameters, data-driven approaches (Brunton & Kutz, 2019) may be helpful. Furthermore, bubbles often exist as a cloud in practice, for which data-driven approaches could help us to de-

velop reduced-order models for single bubble dynamics used in cloud bubble simulations (Preston *et al.*, 2007; Ando *et al.*, 2011; Fuster & Colonius, 2011; Maeda & Colonius, 2018).

6.2.2 Shape stability of a bubble

Additional experimental studies for parametric instability in hydrogels would be helpful to confirm the validity of the non-spherical analysis. Predictions by the natural frequency and a Mathieu equation can be compared with experimental observations of different non-spherical modes with various gel concentrations as well as ultrasound frequencies. However, we should be careful not to damage the gel during the experiments because the most unstable mode in the parametric instability is sensitive to the shear modulus. Viscosity can be compared with the decay rate observed from the non-spherical oscillations driven by pulse-wave ultrasound.

Numerical simulations of the non-spherical model can predict the Rayleigh–Taylor-type instability, while it would be helpful to have a theory to systematically predict this instability based on the stretch ratio, viscoelastic properties and initial perturbation amplitude. Interplay between the Rayleigh–Taylor-type and parametric instabilities may also be important to understand the shape instability of a bubble during inertial collapse. Although experimental studies for the Rayleigh–Taylor-type instability are challenging due to the limited spatial and temporal resolutions of high-speed cameras, the instability results in bubble break up (Brennen, 2002) which could be captured in experiments. It is also difficult to control the initial perturbations, and multiple cameras would be needed to quantitatively image non-spherical perturbations.

From a modeling standpoint, compressible effects on the perturbation and mode interactions (Shaw, 2006) would be important to further study the shape stability of a bubble during inertial collapse. The non-spherical perturbation analysis could be extended to two bubbles (or a bubble near a rigid wall) to investigate the bubble-bubble interactions (Takahira *et al.*, 1991; Liu *et al.*, 2016). Ultrasound-induced dynamics of two bubbles (e.g., secondary Bjerknes force) in soft matter would be of interest for the therapeutic ultrasound. For ultrasound drug delivery, the non-spherical perturbation analysis needs to be extended to a bubble in non-Newtonian fluids such as blood.

Shock waves (Supponen *et al.*, 2017) or velocity and stress fields (Collis *et al.*, 2010; Cleve *et al.*, 2019) induced by non-spherical bubble dynamics are also important problems in the therapeutic ultrasound.

Appendices

Appendix A

Dimensionless Form of the Governing Equations

The dimensionless form of the gas-vapor model is included in section 3.2.5, while the dimensionless forms of the constant-γ model, pure gas model, viscous gas model, and non-spherical model are summarized in this appendix. The relevant dimensionless numbers are listed in table 3.3. We choose the characteristic length and time as $L_c = R_{eq}$ and $T_c = 1/f_d$ for ultrasound-induced bubble oscillations, and $L_c = R_{max}$ and $T_c = R_{max}\sqrt{\rho_\infty/p_{atm}}$ (Rayleigh collapse time) for laser-induced bubble collapse.

A.1 The constant-γ model

The dimensionless form of the constant-γ model (3.18) to (3.21) is obtained as follows:

- Ordinary Differential Equation (ODE) for homobaric bubble pressure

$$\dot{p}_b^* = \frac{3}{R^*}\left[-\gamma p_b^* u_{r,m,w}^* + (\gamma-1)\frac{\rho_m}{\rho_\infty}\frac{1}{\mathrm{Ec}}\frac{\mathrm{Fo}_h}{R^*}\left.\frac{\partial\tau^*}{\partial y}\right|_w\right], \tag{A.1}$$

- Partial Differential Equation (PDE) for temperature

$$\frac{\partial\tau^*}{\partial t^*} + \frac{u_r^* - \dot{R}^* y}{R^*}\frac{\partial\tau^*}{\partial y} = \frac{\rho_\infty}{\rho_m}\mathrm{Ec}K^*\dot{p}_b^* + K^*\frac{\mathrm{Fo}_h}{R^{*2}}\frac{1}{y^2}\frac{\partial}{\partial y}\left(y^2\frac{\partial\tau^*}{\partial y}\right), \tag{A.2}$$

- PDE for mass fraction of vapor

$$\frac{\partial k}{\partial t^*} + \frac{u_r^* - \dot{R}^* y}{R^*}\frac{\partial k}{\partial y} = \frac{\mathrm{Fo}_m}{R^{*2}}\frac{1}{\rho_m y^2}\frac{\partial}{\partial y}\left(\rho_m y^2 \frac{\partial k}{\partial y}\right), \tag{A.3}$$

- The radial velocity field ($0 \le y \le 1$)

$$u_r^*(y, t^*) = \frac{1}{\gamma p_b^*}\left[-\frac{1}{3}R^* y \dot{p}_b^* + (\gamma - 1)\frac{\rho_m}{\rho_\infty}\frac{1}{\mathrm{Ec}}\frac{\mathrm{Fo}_h}{R^*}\frac{\partial \tau^*}{\partial y}\right]. \tag{A.4}$$

A.2 The pure gas model

The dimensionless form of the pure gas model (2.7), (2.9) and (2.10) is obtained as follows:

- ODE for homobaric bubble pressure

$$\dot{p}_b^* = \frac{3}{R^*}\left[-\gamma p_b^* \dot{R}^* + (\gamma - 1)\frac{\rho_m}{\rho_\infty}\frac{1}{\mathrm{Ec}}\frac{\mathrm{Fo}_h}{R^*}\left.\frac{\partial \tau^*}{\partial y}\right|_w\right], \tag{A.5}$$

- PDE for temperature

$$\frac{\partial \tau^*}{\partial t^*} + \frac{u_r^* - \dot{R}^* y}{R^*}\frac{\partial \tau^*}{\partial y} = \frac{\rho_\infty}{\rho_m}\mathrm{Ec} K^* \dot{p}_b^* + K^*\frac{\mathrm{Fo}_h}{R^{*2}}\frac{1}{y^2}\frac{\partial}{\partial y}\left(y^2\frac{\partial \tau^*}{\partial y}\right), \tag{A.6}$$

- The radial velocity field ($0 \le y \le 1$)

$$u_r^*(y, t^*) = \frac{1}{\gamma p_b^*}\left[-\frac{1}{3}R^* y \dot{p}_b^* + (\gamma - 1)\frac{\rho_m}{\rho_\infty}\frac{1}{\mathrm{Ec}}\frac{\mathrm{Fo}_h}{R^*}\frac{\partial \tau^*}{\partial y}\right]. \tag{A.7}$$

A.3 The viscous gas model

The dimensionless form of the viscous gas model (B.3), (B.7), (B.4) and (B.2) is obtained as follows:

- ODE for homobaric bubble pressure

$$\dot{p}_b^* = \frac{3}{R^*}\left[-\gamma p_b^* \dot{R}^* + (\gamma-1)R^* \int_0^1 F_v^* y^2 dy + (\gamma-1)\frac{\rho}{\rho_\infty}\frac{1}{\mathrm{Ec}}\frac{\mathrm{Fo}_h}{R^*}\left.\frac{\partial \tau^*}{\partial y}\right|_w\right], \tag{A.8}$$

- PDE for temperature

$$\frac{\partial \tau^*}{\partial t^*} + \frac{u_r^* - \dot{R}^* y}{R^*}\frac{\partial \tau^*}{\partial y} = \frac{\rho_\infty}{\rho}\mathrm{Ec}K^* \dot{p}_b^* + \mathrm{Ec}K^* F_v^* + K^* \frac{\mathrm{Fo}_h}{R^{*2}}\frac{1}{y^2}\frac{\partial}{\partial y}\left(y^2 \frac{\partial \tau^*}{\partial y}\right), \tag{A.9}$$

- The radial velocity field ($0 \le y \le 1$)

$$u_r^*(y,t^*) = \frac{1}{\gamma p_b^*}\left[-\frac{1}{3}R^* y \dot{p}_b^* + \frac{\gamma-1}{y^2}R^* \int_0^y F_v^* y^2 dy + (\gamma-1)\frac{\rho}{\rho_\infty}\frac{1}{\mathrm{Ec}}\frac{\mathrm{Fo}_h}{R^*}\frac{\partial \tau^*}{\partial y}\right], \tag{A.10}$$

- The viscous terms

$$F_v^* = \frac{2}{\mathrm{Re}_g R^{*2}}\left(\frac{\partial u_r^*}{\partial y}\right)^2 + \left(\frac{1}{\mathrm{Re}_{g,v} R^{*2}} - \frac{2}{3}\frac{1}{\mathrm{Re}_g R^{*2}}\right)\left[\frac{4u_r^{*2}}{y^2} + \frac{4u_r^*}{y}\frac{\partial u_r^*}{\partial y} + \left(\frac{\partial u_r^*}{\partial y}\right)^2\right], \tag{A.11}$$

where $\mathrm{Re}_g = \rho V_c L_c/\mu_g$ and $\mathrm{Re}_{g,v} = \rho V_c L_c/\mu_{g,v}$ are the Reynolds numbers for the gas.

A.4 The non-spherical model

The dimensionless form of the non-spherical model (4.37) is obtained as

$$\ddot{a}_n^* + (A_n^* + A_{n_{rot}}^*)\dot{a}_n^* + (B_n^* + B_{n_{rot}}^*)a_n^* + C_{n_{rot}}^* = 0, \tag{A.12}$$

where

$$A_n^* = 3\frac{\dot{R}^*}{R^*} + \frac{2(n+1)(n+2)}{\mathrm{Re}R^{*2}}, \tag{A.13}$$

$$B_n^* = -(n-1)\frac{\ddot{R}^*}{R^*} + 4(n-1)(n+1)\frac{\dot{R}^*}{\mathrm{Re}R^{*3}} + \frac{(n-1)(n+1)(n+2)}{\mathrm{We}R^{*3}} + \frac{n+1}{\mathrm{Ca}R^{*2}}\left[2\frac{R_{eq}}{L_cR^*} + 2\left(\frac{R_{eq}}{L_cR^*}\right)^4 + \frac{n(n+1)}{1+\frac{R_{eq}}{L_cR^*}+\left(\frac{R_{eq}}{L_cR^*}\right)^2}\right], \tag{A.14}$$

$$A_{n_{rot}}^* = -\frac{2n(n+1)(n+2)}{\mathrm{Re}R^{*2}}, \tag{A.15}$$

$$B_{n_{rot}}^* = 2n(n-1)(n+1)\frac{\dot{R}^*}{\mathrm{Re}R^{*3}} - \frac{n(n+1)^2}{\mathrm{Ca}R^{*2}}\left(\frac{R_{eq}}{L_cR^*}\right)^4, \tag{A.16}$$

$$C_{n_{rot}}^* = \frac{n(n+1)(n+2)}{\mathrm{Re}R^{*2}}\mathcal{T}^*(1,t^*) - n(n+1)\frac{\dot{R}^*}{R^*}\int_1^\infty\left[1-\left(\frac{1}{y}\right)^3\right]\left(\frac{1}{y}\right)^n\mathcal{T}^*(y,t^*)dy. \tag{A.17}$$

The PDE for toroidal field[1] (4.34) is

$$\frac{\partial\mathcal{T}^*}{\partial t^*} - \frac{\dot{R}^*}{R^*}\left(y-\frac{1}{y^2}\right)\frac{\partial\mathcal{T}^*}{\partial y} - \frac{1}{\mathrm{Re}R^{*2}}\frac{\partial^2\mathcal{T}^*}{\partial y^2} + \left[\frac{n(n+1)}{\mathrm{Re}R^{*2}}\frac{1}{y^2} - \frac{2\dot{R}^*}{R^*}\frac{1}{y^3}\right]\mathcal{T}^* = 0, \tag{A.18}$$

where the boundary conditions are $\mathcal{T}^* \to 0$ as $y \to \infty$ and the shear stress continuity (4.35):

$$\mathcal{T}^*(1,t^*) = \frac{2(n+2)}{n+1}\dot{a}_n^* - \frac{2(n-1)}{n+1}\frac{\dot{R}^*}{R^*}a_n^* + \frac{\mathrm{Re}}{\mathrm{Ca}}\left(\frac{R_{eq}}{L_cR^*}\right)^4 a_n^* - 2\int_1^\infty\frac{\mathcal{T}^*(y,t^*)}{y^n}dy. \tag{A.19}$$

[1]The toroidal field is non-dimensionalized as $\mathcal{T}^* = \mathcal{T}/V_c$.

Appendix B

Proof That Gas Viscous Stresses Are Negligible in Bubble Dynamics

B.1 Modeling of viscous gas bubble dynamics

Although gas viscous stresses were neglected in past studies (e.g., Prosperetti *et al.*, 1988), the validity of this assumption has not been discussed. Thus, we numerically evaluate the contributions of gas viscous stresses to the bubble dynamics. In particular, gas viscous stresses are expected to be important during inertial bubble collapse because gas viscosity increases as temperature rises during the rapid compression. We first develop a new model which results in having an integral of the viscous stress field inside the bubble. Then, we numerically evaluate how important the viscous terms are on the bubble dynamics.

A model for the homobaric bubble pressure $p_b(t)$ is derived from the conservation laws (2.1) to (2.3) for the gas inside the bubble in conjunction with the equation of state (ideal gas law). Our goal here is to evaluate the contributions of gas viscous stresses, so we assume that the bubble consists of non-condensable gas (air) only for simplicity. Subtracting conservation of momentum (2.2) multiplied by $u_{j,m}$ from conservation of energy (2.3) results in, for the radial component in spherical coordinates,

$$\frac{\partial}{\partial t}(\rho e) + \frac{1}{r^2}\frac{\partial}{\partial r}\left[r^2(\rho e + p_b)u_r\right] = F_v + \frac{1}{r^2}\frac{\partial}{\partial r}\left(r^2 K\frac{\partial T}{\partial r}\right), \tag{B.1}$$

where

$$F_v = 2\mu_g \left(\frac{\partial u_r}{\partial r}\right)^2 + \left(\mu_{g,v} - \frac{2}{3}\mu_g\right)\left[\frac{4u_r^2}{r^2} + \frac{4u_r}{r}\frac{\partial u_r}{\partial r} + \left(\frac{\partial u_r}{\partial r}\right)^2\right], \tag{B.2}$$

where the viscous stress is Newtonian and $\mu_g(T)$ and $\mu_{g,v}(T)$ are the temperature-dependent dynamic and bulk viscosities of the gas, the heat flux is given by the Fourier's law for heat diffusion, and $K(T)$ is the thermal conductivity of the gas given by equation (2.8). The ideal gas law $p_b = \rho\mathcal{R}T$ and thermodynamic relations $e = C_vT$ and $C_p - C_v = \mathcal{R}$ result in $\rho e = p_b/(\gamma - 1)$ where γ is the ratio of specific heats. Substituting $\rho e = p_b/(\gamma - 1)$ and integrating equation (B.1) from the bubble center $r = 0$ to the bubble wall $r = R(t)$ leads to the Ordinary Differential Equation (ODE) for homobaric bubble pressure:

$$\dot{p}_b = \frac{3}{R}\left[-\gamma p_b\dot{R} + \frac{\gamma - 1}{R^2}\int_0^R F_v r^2 dr + (\gamma - 1)K\left.\frac{\partial T}{\partial r}\right|_w\right]. \tag{B.3}$$

Integrating equation (B.1) from the bubble center $r = 0$ to radial distance r leads to an expression for the radial velocity field ($0 \le r \le R$),

$$u_r(r,t) = \frac{1}{\gamma p_b}\left[-\frac{1}{3}r\dot{p}_b + \frac{\gamma - 1}{r^2}\int_0^r F_v r^2 dr + (\gamma - 1)K\frac{\partial T}{\partial r}\right]. \tag{B.4}$$

Using the thermodynamic relation $e = C_vT$ and conservation of mass (2.1), where C_v is the specific heat at constant volume, equation (B.1) becomes

$$\rho C_v\left(\frac{\partial T}{\partial t} + u_r\frac{\partial T}{\partial r}\right) + \frac{1}{r^2}\frac{\partial}{\partial r}(r^2 p_b u_r) = F_v + \frac{1}{r^2}\frac{\partial}{\partial r}\left(r^2 K\frac{\partial T}{\partial r}\right). \tag{B.5}$$

Substituting the radial velocity (B.4), the second term on the left-hand side is rewritten as

$$\frac{1}{r^2}\frac{\partial}{\partial r}(r^2 p_b u_r) = -\frac{1}{\gamma}\dot{p}_b + \frac{\gamma - 1}{\gamma}F_v + \frac{\gamma - 1}{\gamma}\frac{1}{r^2}\frac{\partial}{\partial r}\left(r^2 K\frac{\partial T}{\partial r}\right). \tag{B.6}$$

Then, equation (B.5) leads to the PDE for temperature:

$$\rho C_p \left(\frac{\partial T}{\partial t} + u_r \frac{\partial T}{\partial r} \right) = \dot{p}_b + F_v + \frac{1}{r^2} \frac{\partial}{\partial r} \left(r^2 K \frac{\partial T}{\partial r} \right). \tag{B.7}$$

The boundary conditions are $\partial T/\partial r|_{r=0} = 0$ at the origin and the cold liquid assumption $T(r = R, t) = T_\infty$ at the bubble wall.

In summary, the dynamics of a spherical viscous gas bubble in soft matter are described by solving the two ODEs and one PDE simultaneously: the Keller–Miksis equation[1] (2.5), the ODE for homobaric bubble pressure (B.3) and the PDE for temperature (B.7), where the radial velocity is given by the equation (B.4). We call this "viscous gas" model. Without viscous terms $F_v = 0$, the viscous gas model reduces to the pure gas model of Prosperetti *et al.* (1988) described in chapter 2. The dimensionless form of the viscous gas model is available in Appendix A.3.

B.2 The effects of gas viscous stresses on bubble dynamics

Since solving the velocity field inside the bubble (B.4) is not straightforward because the equation is implicit, we first evaluate the viscous term in the ODE for homobaric bubble pressure (B.3) in one-way coupling of the solutions obtained from the pure gas model. The dimensionless form of the ODE for homobaric bubble pressure (A.8) can be divided into three parts: polytropic term, viscous term and thermal term,

$$\dot{p}_b^* = \dot{p}_{b,poly}^* + \dot{p}_{b,visc}^* + \dot{p}_{b,ther}^*, \tag{B.8}$$

[1]The gas viscous term in the Keller–Miksis equation which stems from the dynamic boundary condition (Brennen, 1995) is negligible because the gas viscosity at cold liquid temperature and atmospheric pressure is much smaller than the viscosity of soft solid (or liquid) $\mu_g \ll \mu$. For example, the viscosity of air is $\mu_g = 1.8 \times 10^{-5}$ Pa · s which is much smaller than that of water, $\mu = 1.0 \times 10^{-3}$ Pa · s.

where

$$\dot{p}^*_{b,poly} = -3\gamma p^*_b \frac{\dot{R}^*}{R^*}, \tag{B.9}$$

$$\dot{p}^*_{b,visc} = 3(\gamma - 1) \int_0^1 F^*_v y^2 dy, \tag{B.10}$$

$$\dot{p}^*_{b,ther} = 3(\gamma - 1) \frac{\rho}{\rho_\infty} \frac{1}{\mathrm{Ec}} \frac{\mathrm{Fo}_h}{R^{*2}} \left. \frac{\partial \tau^*}{\partial y} \right|_w . \tag{B.11}$$

Temperature-dependent gas dynamic viscosity follows Sutherland's law (White, 2006, pp. 22-28):

$$\mu_g(T) = \mu_{g,0} \left(\frac{T}{T_0} \right)^{\frac{3}{2}} \frac{T_0 + \mathcal{S}_v}{T + \mathcal{S}_v}, \tag{B.12}$$

where the Sutherland's law parameters $\mu_{g,0}$, T_0 and $\mathcal{S}_v$ are available in White (2006, p. 28). For simplicity, we set $\mu_{g,v}(T) = \mu_g(T)$ given the uncertain dependence of the gas bulk viscosity on temperature.

We numerically evaluate the viscous term in the ODE for homobaric bubble pressure (B.8) in the problem of laser-induced inertial collapse of an air bubble in a soft polyacrylamide gel (see table 3.4 in chapter 3). Numerical solutions of the pure gas model are shown in figure B.1 (a), which is the same one as in figure 3.6 (a) in chapter 3. Correspondingly, the polytropic, viscous and thermal terms (B.9) to (B.11) are calculated and compared in figure B.1 (b). Overall, the viscous term is much less dominant than the other polytropic and thermal terms, in spite of taking into account the temperature-dependence of gas viscosity. During the first collapse, each term reaches the maximum values $|\dot{p}^*_{b,poly}| = 1.8 \times 10^9$, $|\dot{p}^*_{b,visc}| = 1.1 \times 10^4$ and $|\dot{p}^*_{b,ther}| = 5.5 \times 10^6$, respectively. Consequently, gas viscous stresses are negligible in the bubble dynamics.

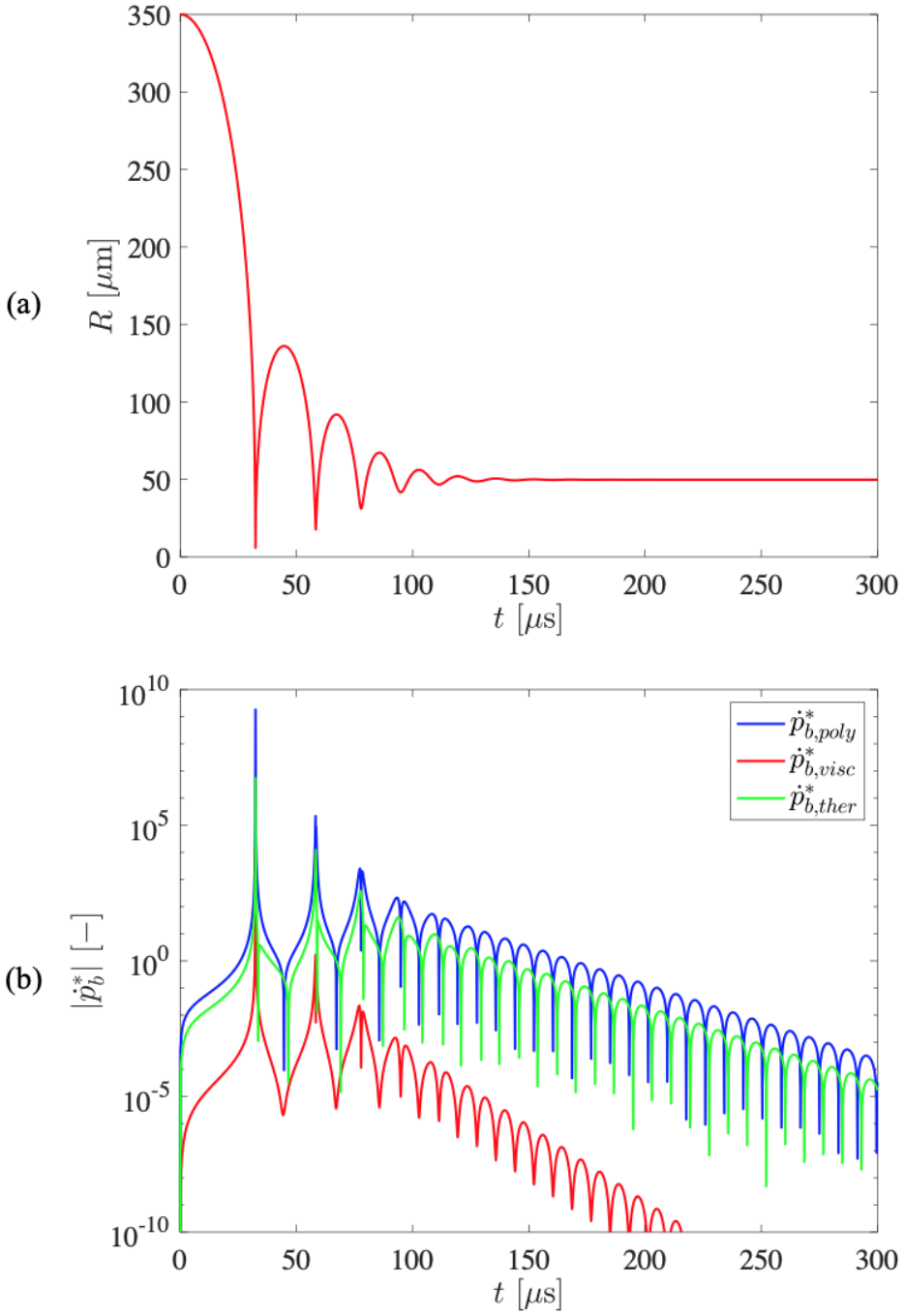

Figure B.1: Comparison among polytropic, viscous and thermal effects on the evolution of homobaric bubble pressure during laser-induced inertial bubble collapse. (a) Solutions of the pure gas model for an air bubble in a soft polyacrylamide gel. (b) One-way coupling evaluation of polytropic, viscous and thermal terms (B.9) to (B.11). Overall, the viscous term is much less dominant than the other terms.

Appendix C

Proof That the Polar and Azimuthal Gradients of the Current Configuration Are of First Order in Perturbation Amplitude

The polar and azimuthal gradients of the current configuration deformed by the non-spherical perturbation $\partial r/\partial\theta$ and $\partial r/\partial\varphi$ prove to be of order $O(a_n)$. The current configuration $r(r_0,\theta,\varphi,t)$ can be split into a spherical part $r_S(r_0,t)$ and a non-spherical correction $r_{NS}(r_0,\theta,\varphi,t)$ as

$$r(r_0,\theta,\varphi,t) = r_S(r_0,t) + r_{NS}(r_0,\theta,\varphi,t). \tag{C.1}$$

The incompressible condition (4.18) leads to

$$r_S(r_0,t) = [r_0^3 + C_S(t)]^{\frac{1}{3}}, \quad r_{NS}(r_0,\theta,\varphi,t) = [r_0^3 + C_{NS}(\theta,\varphi,t)]^{\frac{1}{3}}, \tag{C.2}$$

where functions of integration $C_S(t)$ and $C_{NS}(\theta,\varphi,t)$ are determined by the boundary condition at spherical and non-spherical bubble surfaces, respectively. As a result, to order $O(a_n)$, the current configuration is written as

$$r(r_0,\theta,\varphi,t) = r_S(r_0,t) + \frac{R^2}{r_S^2(r_0,t)} a_n Y_n^m. \tag{C.3}$$

Therefore, $\partial r/\partial r_0$ is of order $O(1)$, while $\partial r/\partial\theta$ and $\partial r/\partial\varphi$ are of order $O(a_n)$.

Bibliography

Akhatov, I., Lindau, O., Topolnikov, A., Mettin, R., Vakhitova, N., & Lauterborn, W. 2001. Collapse and rebound of a laser-induced cavitation bubble. *Phys. Fluids*, **13**, 2805–2819.

Allen, J. S., & Roy, R. A. 2000a. Dynamics of gas bubbles in viscoelastic fluids. I. Linear viscoelasticity. *J. Acoust. Soc. Am.*, **107**, 3167–3178.

Allen, J. S., & Roy, R. A. 2000b. Dynamics of gas bubbles in viscoelastic fluids. II. Nonlinear viscoelasticity. *J. Acoust. Soc. Am.*, **108**, 1640–1650.

Ando, K., & Shirota, E. 2019. Quasistatic growth of bubbles in a gelatin gel under dissolved-gas supersaturation. *Phys. Fluids*, **31**, 111701.

Ando, K., Colonius, T., & Brennen, C. E. 2009. Improvement of acoustic theory of ultrasonic waves in dilute bubbly liquids. *J. Acoust. Soc. Am.*, **126**, EL69–EL74.

Ando, K., Colonius, T., & Brennen, C. E. 2011. Numerical simulation of shock propagation in a polydisperse bubbly liquid. *Int. J. Mult. Flow*, **37**, 596–608.

Bader, K. B., Vlaisavljevich, E., & Maxwell, A. D. 2019. For whom the bubble grows: physical principles of bubble nucleation and dynamics in histotripsy ultrasound therapy. *Ultrasound Med Biol*, **45**, 1056–1080.

Bailey, M. R., Khokhlova, V. A., Sapozhnikov, O. A., Kargl, S. G., & Crum, L. A. 2003. Physical mechanisms of the therapeutic effect of ultrasound (a review). *Acoust. Phys.*, **49**, 369–388.

Bar-Kochba, E., Scimone, M. T., Estrada, J. B., & Franck, C. 2016. Strain and rate-dependent neuronal injury in a 3d *in vitro* compression model of traumatic brain injury. *Sci. Rep.*, **6**, 30550.

Barajas, C., & Johnsen, E. 2017. The effects of heat and mass diffusion on freely oscillating bubbles in a viscoelastic, tissue-like medium. *J. Acoust. Soc. Am.*, **141**, 908–918.

Barney, C. W., Dougan, C. E., McLeod, K. R., Kazemi-Moridani, A., Zheng, Y., Ye, Z., Tiwari, S., Sacligil, I., Riggleman, R. A., Cai, S., Lee, J., Peyton, S. R., Tew, G. N., & Crosby, A. J. 2020. Cavitation in soft matter. *Proc. Natl. Acad. Sci. U.S.A.*, **117**, 9157–9165.

Baughman Shively, S., Horkayne-Szakaly, I., Jones, R. V., Kelly, J. P., Armstrong, R. C., & Perl, D. P. 2016. Characterisation of interface astroglial scarring in the human brain after blast exposure: a post-mortem case series. *Lancet Neurol.*, **15**, 944–953.

Beig, S., & Johnsen, E. 2015. Maintaining interface equilibrium conditions in compressible multiphase flows using interface capturing. *J. Comput. Phys.*, **302**, 548–566.

Brennen, C. E. 1995. *Cavitation and bubble dynamics*. Oxford University Press.

Brennen, C. E. 2002. Fission of collapsing cavitation bubbles. *J. Fluid Mech.*, **472**, 153–166.

Brennen, C. E. 2015. Cavitation in medicine. *Interface Focus*, **5**, 20150002.

Brenner, M. P., Lohse, D., & Dupont, T. F. 1995. Bubble shape oscillations and the onset of sonoluminescence. *Phys. Rev. Lett.*, **75**, 954–957.

Brenner, M. P., Hilgenfeldt, S., & Lohse, D. 2002. Single-bubble sonoluminescence. *Rev. Mod. Phys.*, **74**, 425–484.

Brujan, E. A. 2011. *Cavitation in non-newtonian fluids*. Springer.

Brujan, E. A., & Vogel, A. 2002. Stress wave emission and cavitation bubble dynamics by nanosecond optical breakdown in a tissue phantom. *J. Fluid Mech.*, **558**, 281–308.

Brunton, S. L., & Kutz, J. N. 2019. *Data-driven science and engineering: Machine learning, dynamical systems, and control*. Cambridge University Press.

Chapman, R. B., & Plesset, M. S. 1971. Thermal effects in the free oscillation of gas bubbles. *J. Basic Eng.*, **33**, 373–376.

Cleve, S., Guédra, M., Mauger, C., Inserra, C., & Blanc-Benon, P. 2019. Microstreaming induced by acoustically trapped, non-spherically oscillating microbubbles. *J. Fluid Mech.*, **875**, 597–621.

Collis, J., Manasseh, R., Liovic, P., Tho, P., Ooi, A., Petkovic-Duran, K., & Zhu, Y. 2010. Cavitation microstreaming and stress fields created by microbubbles. *Ultrasonics*, **50**, 273–279.

Coussios, C. C., & Roy, R. A. 2008. Applications of acoustics and cavitation to noninvasive therapy and drug delivery. *Annu. Rev. Fluid Mech.*, **40**, 395–420.

Currie, I. G. 2013. *Fundamental mechanics of fluids*. CRC Press.

Cussler, E. L. 2009. *Diffusion: Mass transfer in fluid systems*. Cambridge University Press.

Daily, J., Pendlebury, J., Langley, K., & Hurd, R. 2014. Catastrophic cracking courtesy of quiescent cavitation. *Phys. Fluids*, **26**, 091107.

Dollet, B., van der Meer, S. M., Garbin, V., de Jong, N., Lohse, D., & Versluis, M. 2008. Nonspherical oscillations of ultrasound contrast agent microbubbles. *Ultrasound Med. Biol.*, **34**, 1465–1473.

Dollet, B., Marmottant, P., & Garbin, V. 2019. Bubble dynamics in soft and biological matter. *Annu. Rev. Fluid Mech.*, **51**, 331–355.

Estrada, J. B., Barajas, C., Henann, D. L., Johnsen, E., & Franck, C. 2018. High strain-rate soft material characterization via inertial cavitation. *J. Mech. Phys. Solids*, **112**, 291–317.

Feng, Z. C., & Leal, L. G. 1997. Nonlinear bubble dynamics. *Annu. Rev. Fluid Mech.*, **29**, 201–243.

Flynn, H. G. 1975a. Cavitation dynamics. I. A mathematical formulation. *J. Acoust. Soc. Am.*, **57**, 1379–1396.

Flynn, H. G. 1975b. Cavitation dynamics. II. Free pulsations and models for cavitation bubble. *J. Acoust. Soc. Am.*, **58**, 1160–1170.

Francescutto, A., & Nabergoj, R. 1978. Pulsation amplitude threshold for surface waves on oscillating bubbles. *Acustica*, **41**, 215–220.

Franck, C. 2017. Microcavitation: the key to modeling blast traumatic brain injury? *Concussion*, **2**, CNC47.

Fujikawa, S., & Akamatsu, T. 1980. Effects of the non-equilibrium condensation of vapour on the pressure wave produced by the collapse of a bubble in a liquid. *J. Fluid Mech.*, **97**, 481–512.

Fujiwara, T., & Shima, A. 1980. Nonlinear oscillations of bubbles in compressible hydraulic oils. *J. Acoust. Soc. Am.*, **68**, 1502–1508.

Fung, Y. C. 1993. *Biomechanics: Mechanical properties of living tissues*. Springer.

Fuster, D., & Colonius, T. 2011. Modelling bubble clusters in compressible liquids. *J. Fluid Mech.*, **688**, 352–389.

Gaudron, R., Warnez, M. T., & Johnsen, E. 2015. Bubble dynamics in a viscoelastic medium with nonlinear elasticity. *J. Fluid Mech.*, **766**, 54–75.

Gaudron, R., Murakami, K., & Johnsen, E. 2020. Shape stability of a gas cavity surrounded by linear and nonlinear elastic media. *J. Mech. Phys. Solids*, **143**, 104047.

Goeller, J., Wardlaw, A., Treichler, D., O'Bruba, J., & Weiss, G. 2012. Investigation of cavitation as a possible damage mechanism in blast-induced traumatic brain injury. *J. Neurotrauma*, **29**, 1970–1981.

Hamaguchi, F., & Ando, K. 2015. Linear oscillation of gas bubbles in a viscoelastic material under ultrasound irradiation. *Phys. Fluids*, **27**, 113103.

Hao, Y., & Prosperetti, A. 1999. The effect of viscosity on the spherical stability of oscillating gas bubbles. *Phys. Fluids*, **11**, 1309–1317.

Hao, Y., Zhang, Y., & Prosperetti, A. 2017. Mechanics of gas-vapor bubbles. *Phys. Rev. Fluids*, **2**, 034303.

Hayashi, C. 1964. *Nonlinear oscillations in physical systems*. McGraw-Hill Co.

Herring, G. 1941. Theory of the pulsations of the gas bubble produced by an underwater explosion. *OSRD Rep. No.*, **236**.

Hilgenfeldt, S., Lohse, D., & Brenner, M. P. 1996. Phase diagrams for sonoluminescing bubbles. *Phys. Fluids*, **21**, 2808–2826.

Hua, C., & Johnsen, E. 2013. Nonlinear oscillations following the rayleigh collapse of a gas bubble in a linear viscoelastic (tissue-like) medium. *Phys. Fluids*, **25**, 083101.

Hullin, Ch. 1977. Stabilitätsgrenze pulsierender luftblasen in wasser. *Acustica*, **37**, 64–73.

Ibsen, S., Schutt, C. E., & Esener, S. 2013. Microbubble-mediated ultrasound therapy: a review of its potential in cancer treatment. *Drug Des. Dev. Ther.*, **7**, 375–388.

Jamburidze, A., De Corato, M., Huerre, A., Pommella, A., & Garbin, V. 2017. High-frequency linear rheology of hydrogels probed by ultrasound-driven microbubble dynamics. *Soft Matter*, **13**, 3946–3953.

Johnsen, E., & Colonius, T. 2009. Numerical simulations of non-spherical bubble collapse. *J. Fluid Mech.*, **629**, 231–262.

Kamath, V., Prosperetti, A., & Egolfopoulos, F. N. 1993. A theoretical study of sonoluminescence. *J. Acoust. Soc. Am.*, **94**, 248–260.

Kameda, M., & Matsumoto, Y. 1999. Nonlinear oscillation of a spherical gas bubble in acoustic fields. *J. Acoust. Soc. Am.*, **106**, 3156–3166.

Keller, J. B., & Miksis, M. 1980. Bubble oscillations of large amplitude. *J. Acoust. Soc. Am.*, **68**, 628–633.

Klapcsik, K., & Hegedüs, F. 2019. Study of non-spherical bubble oscillations under acoustic irradiation in viscous liquid. *Ultrason. Sonochem.*, **54**, 256–273.

Kundu, P. K., Cohen, I. M., & Dowling, D. R. 2016. *Fluid mechanics*. Academic Press.

Lamb, H. 1932. *Hydrodynamics*. Cambridge University Press.

Lauterborn, W. 1976. Numerical investigation of nonlinear oscillations of gas bubbles in liquids. *J. Acoust. Soc. Am.*, **59**, 283–293.

Leighton, T. G. 1994. *The acoustic bubble*. Academic Press.

Lezzi, A., & Prosperetti, A. 1987. Bubble dynamics in a compressible liquid. part 2. second-order theory. *J. Fluid Mech.*, **185**, 289–321.

Lin, H., Storey, B. D., & Szeri, A. J. 2002. Inertially driven inhomogeneities in violently collapsing bubbles: the validity of the rayleigh–plesset equation. *J. Fluid Mech.*, **452**, 145–162.

Liu, Y., Sugiyama, K., Takagi, S., & Matsumoto, Y. 2011. Numerical study on the shape oscillation of an encapsulated microbubble in ultrasound field. *Phys. Fluids*, **23**, 041904.

Liu, Y., Sugiyama, K., Takagi, S., & Matsumoto, Y. 2012. Surface instability of an encapsulated bubble induced by an ultrasonic pressure wave. *J. Fluid Mech.*, **691**, 315–340.

Liu, Y., Sugiyama, K., & Takagi, S. 2016. On the interaction of two encapsulated bubbles in an ultrasound field. *J. Fluid Mech.*, **804**, 58–89.

Maeda, K., & Colonius, T. 2018. Eulerian-lagrangian method for simulation of cloud cavitation. *J. Comput. Phys.*, **371**, 994–1017.

Mitragotri, S. 2005. Healing sound: the use of ultrasound in drug delivery and other therapeutic applications. *Nature Rev. Drug Discov.*, **4**, 255–260.

Movahed, P., Kreider, W., Maxwell, A. D., Hutchens, S. B., & Freund, J. B. 2016. Cavitation-induced damage of soft materials by focused ultrasound bursts: A fracture-based bubble dynamics model. *J. Acoust. Soc. Am.*, **140**, 1374–1386.

Murakami, K., Gaudron, R., & Johnsen, E. 2018. Non-spherical dynamics of gas bubbles in soft matter. *Pages 732–736 of:* Katz, J. (ed), *Proceedings of the 10th International Symposium on Cavitation (CAV2018)*. ASME Press.

Murakami, K., Gaudron, R., & Johnsen, E. 2020a. Shape stability of a gas bubble in a soft solid. *Ultrason. Sonochem.*, **67**, 105170.

Murakami, K., Yamakawa, Y., Johnsen, E., & Ando, K. 2020b. Ultrasound-induced nonlinear oscillations of a spherical bubble in a gelatin gel. *Submitted.*

Negadi, L., Feddal-Benabed, B., Bahadur, I., Saab, J., Zaoui-Djelloul-Daouadji, M., Ramjugernath, D., & Negadi, A. 2017. Effect of temperature on density, sound velocity, and their derived properties for the binary systems glycerol with water or alcohols. *J. Chem. Thermodyn.*, **109**, 124–136.

Nigmatulin, R. I., Khabeev, N. S., & Nagiev, F. B. 1981. Dynamics, heat and mass transfer of vapour-gas bubbles in a liquid. *Int. J. Heat Mass Transf.*, **24**, 1033–1044.

Plesset, M. S. 1949. The dynamics of cavitation bubbles. *J. Appl. Mech.*, **16**, 277–282.

Plesset, M. S. 1954. On the stability of fluid flows with spherical symmetry. *J. Appl. Phys.*, **25**, 96–98.

Plesset, M. S., & Prosperetti, A. 1977. Bubble dynamics and cavitation. *Annu. Rev. Fluid Mech.*, **9**, 145–185.

Press, W. H., Teukolsky, S. A., Vetterling, W. T., & Flannery, B. P. 2007. *Numerical recipes*. Cambridge University Press.

Preston, A. T. 2004. Modeling heat and mass transfer in bubbly cavitating flows and shock waves in cavitating nozzles. *Ph.D. thesis, California Institute of Technology*.

Preston, A. T., Colonius, T., & Brennen, C. E. 2007. A reduced-order model of diffusive effects on the dynamics of bubbles. *Phys. Fluids*, **19**, 123302.

Prosperetti, A. 1977a. Thermal effects and damping mechanisms in the forced radial oscillations of gas bubbles in liquids. *J. Acoust. Soc. Am.*, **61**, 17–27.

Prosperetti, A. 1977b. Viscous effects on perturbed spherical flows. *Quart. Appl. Math.*, **34**, 339–352.

Prosperetti, A. 2017. Vapor bubbles. *Annu. Rev. Fluid Mech.*, **49**, 221–248.

Prosperetti, A., & Lezzi, A. 1986. Bubble dynamics in a compressible liquid. part 1. first-order theory. *J. Fluid Mech.*, **168**, 457–478.

Prosperetti, A., Crum, L. A., & Commander, K. W. 1988. Nonlinear bubble dynamics. *J. Acoust. Soc. Am.*, **83**, 502–514.

Rayleigh, L. 1917. On the pressure developed in a liquid during the collapse of a spherical cavity. *Phil. Mag. Ser. 6*, **34**, 94–98.

Saint-Michel, B., & Garbin, V. 2020. Bubble dynamics for broadband microrheology of complex fluids. *Curr. Opin. Colloid Interface Sci.*, **50**, 101392.

Shaw, S. J. 2006. Translation and oscillation of a bubble under axisymmetric deformation. *Phys. Fluids*, **18**, 072104.

Stricker, L., Prosperetti, A., & Lohse, D. 2011. Validation of an approximate model for the thermal behavior in acoustically driven bubbles. *J. Acoust. Soc. Am.*, **130**, 3243–3251.

Supponen, O., Obreschkow, D., Kobel, P., Tinguely, M., Dorsaz, N., & Farhat, M. 2017. Shock waves from nonspherical cavitation bubbles. *Phys. Rev. Fluids*, **2**, 093601.

Takahira, H., Akamatsu, T., & Fujikawa, S. 1991. Dynamics of two nonspherical bubbles in a viscous liquid. *Trans. JSME B*, **57**, 447–455.

Takamura, K., Fischer, H., & Morrow, N. R. 2012. Physical properties of aqueous glycerol solutions. *J. Pet. Sci. Eng.*, **98-99**, 50–60.

Taylor, G. I. 1950. The instability of liquid surfaces when accelerated in a direction perpendicular to their planes. i. *Proc. R. Soc. A.*, **201**, 192–196.

Thompson, P. A. 1972. *Compressible-fluid dynamics*. McGraw-Hill.

Tomita, Y., & Shima, A. 1977. On the behavior of a spherical bubble and the impulse pressure in a viscous compressible liquid. *Bull. JSME*, **20**, 1453–1460.

Versluis, M., Goertz, D. E., Palanchon, P., Heitman, I. L., & van der Meer, S. M. 2010. Microbubble shape oscillations excited through ultrasonic parametric driving. *Phys. Rev. E.*, **82**, 026321.

Warnez, M. T., & Johnsen, E. 2015. Numerical modeling of bubble dynamics in viscoelastic media with relaxation. *Phys. Fluids*, **27**, 063103.

White, F. M. 2006. *Viscous fluid flow*. McGraw-Hill.

Xu, Z., Ludomirsky, A., Eun, L. Y., Hall, T. L., Tran, B. C., Fowlkes, J. B., & Cain, C. A. 2004. Controlled ultrasound tissue erosion. *IEEE T. Ultrason. Ferr.*, **51**, 726–736.

Yamashita, T., & Ando, K. 2020. Low-intensity ultrasound induced cavitation and streaming in oxygen-supersaturated water: Role of cavitation bubbles as physical cleaning agents. *Ultrason. Sonochem.*, **52**, 268–279.

Yang, J., Cramer, H. C., & Franck, C. 2020. Extracting non-linear viscoelastic material properties from violently-collapsing cavitation bubbles. *Extreme Mech. Lett.*, **39**, 100839.

Yang, X., & Church, C. 2005. A model for the dynamics of gas bubbles in soft tissue. *J. Acoust. Soc. Am.*, **118**, 3595–3606.

Yasui, K., Tuziuti, T., & Iida, Y. 2004. Optimum bubble temperature for sonochemical production of oxidants. *Ultrasonics*, **42**, 579–584.

Zhang, Y., Du, X., Xian, H., & Wu, Y. 2015. Instability of interfaces of gas bubbles in liquids under acoustic excitation with dual frequency. *Ultrason. Sonochem.*, **23**, 16–20.

Zhang, Y., Gao, Y., & Du, X. 2018. Stability mechanisms of oscillating vapor bubbles in acoustic fields. *Ultrason. Sonochem.*, **40**, 808–814.

Zhou, G., & Prosperetti, A. 2020. Modelling the thermal behaviour of gas bubbles. *J. Fluid Mech.*, **901**, R3.